

Low-metallicity massive single stars with rotation

Evolutionary models applicable to I Zwicky 18

Dorottya Szécsi¹, Norbert Langer¹, Sung-Chul Yoon², Debashis Sanyal¹, Selma de Mink³, Christopher J. Evans⁴, and Tyl Dermine¹

¹ Argelander-Institut für Astronomie der Universität Bonn, Auf dem Hügel 71, 53121 Bonn, Germany

² Department of Physics & Astronomy, Seoul National University, Gwanak-ro 1, Gwanak-gu, 151-742, Seoul, South Korea

³ Astronomical Institute Anton Pannekoek, University of Amsterdam, 1098 XH Amsterdam, The Netherlands

⁴ UK Astronomy Technology Centre, Royal Observatory, Blackford Hill, Edinburgh, EH9 3HJ, UK

Received August 6, 2018/ Accepted ...

ABSTRACT

Context. Low-metallicity environments such as the early Universe and compact star-forming dwarf galaxies contain many massive stars. These stars influence their surroundings through intense UV radiation, strong winds and explosive deaths. A good understanding of low-metallicity environments requires a detailed theoretical comprehension of the evolution of their massive stars.

Aims. We aim to investigate the role of metallicity and rotation in shaping the evolutionary paths of massive stars and to provide theoretical predictions that can be tested by observations of metal-poor environments.

Methods. Massive rotating single stars with an initial metal composition appropriate for the dwarf galaxy I Zw 18 ($[\text{Fe}/\text{H}]=-1.7$) are modelled during hydrogen burning for initial masses of 9-300 M_{\odot} and rotational velocities of 0-900 km s^{-1} . Internal mixing processes in these models were calibrated based on an observed sample of OB-type stars in the Magellanic Clouds.

Results. Even moderately fast rotators, which may be abundant at this metallicity, are found to undergo efficient mixing induced by rotation resulting in quasi chemically-homogeneous evolution. These homogeneously-evolving models reach effective temperatures of up to 90 kK during core hydrogen burning. This, together with their moderate mass-loss rates, make them Transparent Wind Ultraviolet INTense stars (TWUIN star), and their expected numbers might explain the observed He II ionizing photon flux in I Zw 18 and other low-metallicity He II galaxies. Our slowly rotating stars above $\sim 80 M_{\odot}$ evolve into late B- to M-type supergiants during core hydrogen burning, with visual magnitudes up to 19^m at the distance of I Zw 18. Both types of stars, TWUIN stars and luminous late-type supergiants, are only predicted at low metallicity.

Conclusions. Massive star evolution at low metallicity is shown to differ qualitatively from that in metal-rich environments. Our grid can be used to interpret observations of local star-forming dwarf galaxies and high-redshift galaxies, as well as the metal-poor components of our Milky Way and its globular clusters.

Key words. stars: low-metallicity – stars: massive – stars: evolution – stars: rotation – stars: main-sequence – stars: red supergiants

1. Introduction

Many of the first stars in the Universe are thought to have started out very massive and almost metal-free (Abel et al. 2002; Bromm & Larson 2004; Frebel et al. 2005). Direct observations of these stars are not possible with current telescopes. However, low-metallicity massive stars can also be found in the local Universe: some of the nearby dwarf galaxies form massive stars at a high rate (Tolstoy et al. 2009; Weisz et al. 2014). As these galaxies can be directly observed and as their metallicity happens to be close to that of the first stars, they can be used as laboratories to study massive stellar evolution at low (i.e. substantially subsolar) metallicity. Such studies may lead us to a better understanding of the metallicity dependence of stellar evolution, including the first stars in the Universe.

Apart from the cosmological implications of stars at high redshift, there are another reasons to study stellar evolution at low metallicity. The initial chemical composition of a star influences the whole evolutionary path, internal structure, circumstellar surroundings and even the final fate of the star (Meynet & Maeder 2002; Hirschi et al. 2005; Meynet & Maeder 2005; Brott et al. 2011; Yoon et al. 2012; Yusof et al. 2013). There is ob-

servational evidence that long-duration gamma-ray bursts tend to prefer low-metallicity environments (Levesque et al. 2010; Modjaz et al. 2011; Graham & Fruchter 2013) and high redshifts (Horváth et al. 2014). Theoretical studies have shown that fast rotating stars at low metallicity may evolve quasi chemically-homogeneously (Yoon et al. 2006; Brott et al. 2011). These homogeneously-evolving stellar models are predicted to become fast rotating Wolf-Rayet (WR) type objects during the post main-sequence phase. They are, therefore, candidates of long-duration gamma-ray burst progenitors within the collapsar scenario (MacFadyen & Woosley 1999; Yoon & Langer 2005; Woosley & Heger 2006). Moreover, broad line type Ic supernovae (Arcavi et al. 2010; Sanders et al. 2012) that are associated with gamma-ray bursts (Modjaz et al. 2011; Graham & Fruchter 2013) as well as the recently identified superluminous supernovae (Quimby et al. 2011; Lunnan et al. 2013) occur preferentially in low-metallicity dwarf galaxies. This may corroborate the idea that reduced wind mass-loss at low metallicity (Vink et al. 2001; Mokiem et al. 2007) may allow for rapid rotation rates (Yoon et al. 2006; Georgy et al. 2009) and very massive (Langer et al. 2007; Yusof et al. 2013; Kozyreva et al. 2014) supernova progenitors. A good understanding of the evolution

of metal-poor massive stars is, therefore, important to probe the origin of these extremely energetic explosions.

The first stars are thought to have consisted of mostly hydrogen and helium with a ${}^7\text{Li}$ mass fraction of about 10^{-9} (Mathews et al. 2005). This first generation synthesized heavy elements via nuclear fusion, either in hydrostatic equilibrium or during an explosion. Stars that have formed from material processed by the first stars therefore also have non-zero metallicity. This second generation of stars may also be important in the re-ionisation history and chemical evolution of the early Universe (Yoshida et al. 2007; Greif et al. 2010; Hosokawa et al. 2012). Additionally, the imprint of the first nucleosynthesis events is thought to be present in extremely metal-poor Galactic halo stars (Beers & Christlieb 2005; Keller et al. 2014), for which our understanding is still incomplete (Heger & Woosley 2010; Lee et al. 2014).

Galactic globular clusters are also observed to have a low metal content ($[\text{Fe}/\text{H}]=-2.2\dots-0.2$) (Gratton et al. 2001; Yong et al. 2003; Caretta et al. 2005; D’Antona & Ventura 2010; Caretta 2010). Although we observe only low-mass stars in globular clusters today, there was probably a generation of massive stars during their early epoch (Portegies Zwart et al. 2010; Denissenkov & Hartwick 2014; Longmore et al. 2014). A theoretical understanding of massive stars at this metallicity might help to explain some of the most intriguing phenomena concerning globular clusters, e.g. the abundance anomalies and multiple populations observed in these objects (Decressin et al. 2007; de Mink et al. 2009; Bastian et al. 2013).

We can observe environments at very low but finite metallicity, if we turn to nearby blue compact dwarf galaxies (BCDG) (Searle & Sargent 1972; Zhao et al. 2013). BCDGs are typically small, high surface-brightness galaxies of low metallicity, with blue colours and intense emission lines (Hunter & Thronson 1995; Vaduvescu et al. 2007). Additionally, some of them contain WR stars, e.g. I Zw 18 (Legrand et al. 1997; Aloisi et al. 1999; Schaerer et al. 1999a; Shirazi & Brinchmann 2012; Kehrig et al. 2013). Moreover, nearby BCDGs form massive stars at a high rate of up to $1 M_{\odot} \text{ yr}^{-1}$ (Annibali et al. 2013). Given that their metallicity is observed to be low, they are laboratories to study the evolution of metal-poor massive stars (Izotov & Thuan 2002, 2004; Annibali et al. 2013). As mentioned above, modelling stellar evolution with a composition suitable for these dwarf galaxies can be an important step towards a deeper understanding of low-metallicity environments.

Recent studies theorized about the presence of metal-free Population III (Pop III) stars in finite-metallicity environments to explain various observational phenomena such as unusually high He II and Lyman- α emission in local dwarf galaxies or high-redshift galaxies (Heap et al. 2015; Kehrig et al. 2015; Sobral et al. 2015). However, the detailed evolutionary behaviour of low- but finite-metallicity massive stars has not been investigated comprehensively. With this study, we aim to shed new light on this issue.

We computed stellar evolutionary sequences of single stars in the mass range $9\text{--}300 M_{\odot}$ with rotational velocities between $0\text{--}900 \text{ km s}^{-1}$ and with an initial composition of $Z=0.0002$. Here we present the core-hydrogen-burning phase of these models. We emphasize therefore that the present study applies only to the main-sequence evolution of low-metallicity massive stars. The post-main-sequence evolution and final fates of our models will be discussed in a following study.

We include rotation into our models because massive stars are generally rapid rotators (Penny & Gies 2009; Huang et al. 2010; Ramírez-Agudelo et al. 2013; Dufton et al. 2013). Rotation may influence the life of massive stars in many ways (Heger

et al. 2000; Meynet & Maeder 2000; Hirschi et al. 2005; Yoon et al. 2006; Ekström et al. 2008; Georgy et al. 2012). At low metallicity, rotation may be particularly important because the stellar wind induced spin-down is much weaker (cf. Brott et al. 2011), and the stars remain rapidly rotating such that rotational mixing is facilitated (Maeder & Meynet 2000; Langer 2012).

We consider the evolution of isolated single stars. The majority of massive stars may form in binary systems that lead to interaction during their lives (Chini et al. 2012; Sana et al. 2012), often already during their main-sequence evolution. This can drastically affect their evolution (Eldridge et al. 2008, 2011) and binary products may be abundantly present among the brightest stars in dwarf galaxies (de Mink et al. 2014; Schneider et al. 2014). However, in many cases stars are spun up early during their evolution (de Mink et al. 2013). This means that our models provide a fair approximation to the evolution of stars spun up in binary systems.

Our paper is organised as follows. First we summarise the physical assumptions made for calculating the stellar evolutionary models in Sect. 2. Then we give an overview of the grid of stellar model sequences and the classification system that describes the different types of evolution at low metallicity in Sect. 3. We explain the behaviour of individual stellar tracks in the Hertzsprung–Russell (HR) diagram in Sect. 4. In Sect. 5, we analyse the models that evolve into core-hydrogen-burning cool supergiants. In Sect. 6, we present the models that evolve into transparent wind UV-intense stars. An analysis of the helium abundance at the surface and in the core is given in Sect. 7. A closer look into the mass-loss history is taken in Sect. 8. The evolution of the rotational velocity is presented in Sect. 9. In Sect. 10, we provide information on the ionizing fluxes predicted by our models. In Sect. 11, we discuss the results in context of previous publications of massive-star evolution at low metallicity. A summary of the results is given in Sect. 12. The appendices (available only in the online version) provide a summary of the models, a table of the ionizing fluxes, as well as isochrones.

2. Physical assumptions

We use a one-dimensional hydrodynamic binary evolutionary code (BEC) to compute rotating and non-rotating single stellar evolutionary sequences (see Heger et al. 2000; Heger & Langer 2000; Brott et al. 2011; Yoon et al. 2012, and references therein). BEC solves the five stellar structure equations using the implicit Henyey method. It contains detailed state-of-the-art treatment of rotation, magnetic fields, angular momentum transport and mass-loss.

Stellar model sequences are computed under the physical assumptions described in this section. The time between two consecutive models in the sequence is chosen adaptively, resolving the structural changes in detail. We typically resolve the core-hydrogen-burning evolution with ~ 2000 time steps, for which each stellar model is resolved into a similar number of mass shells. The whole set of evolutionary sequences with different initial masses and rotational velocities (but the same initial composition) is referred to as our grid of models.

The calculations were stopped when the central helium abundance reaches $Y_{\text{C}}=0.98$. We choose this as the terminal age main-sequence (TAMS). After this point, as the hydrogen fraction in the core becomes very small, the central temperature increases substantially due to an overall contraction, and the star falls out of thermal equilibrium. For this reason, we exclude this short contracting phase from the analysis of the main-sequence evolution of our stellar models.

2.1. Initial chemical composition

Stellar models with the same initial mass M_{ini} and same initial rotational velocity v_{ini} but different initial composition Z_{ini} may evolve differently for at least two reasons. First, the metallicity has a fundamental impact on the mass-loss rate of a star: the higher the total metal abundance at the surface, the stronger the stellar wind (Kudritzki et al. 1987; Vink et al. 2001; Mokiem et al. 2007; Puls et al. 2008). Second, due to the reduced radiative opacity and the low amount of CNO nuclei as initial catalysts, metal-poor stars are more compact than corresponding metal-rich ones (Ekström et al. 2011; Yoon et al. 2006).

We compare recent observations of the metal abundance pattern of the Sun and the dwarf galaxy I Zw 18 in Fig. 1. In particular carbon and nitrogen are under abundant compared to scaled solar abundances (see also Nicholls et al. 2014). We also plot the composition of the Small Magellanic Cloud (SMC) scaled down by ten. The metal abundance patterns of BCDGs in general are different from that of the Sun (Izotov et al. 1999; Vink et al. 2001; Tramper et al. 2011; Leboutteiller et al. 2013; Nicholls et al. 2014), showing that the metal abundance pattern of the SMC, which is the nearest metal-poor irregular dwarf galaxy, is a better approximation for the composition of e.g. I Zw 18 than the solar abundance pattern. Hence, to obtain theoretical predictions for the massive stars in I Zw 18, we take the abundance pattern of the SMC as in Brott et al. (2011), scale it down by a factor of ten and calculate massive stellar evolutionary models with this composition. The metallicity of our models (i.e. the sum of all metals as mass fraction) is then $Z=0.0002$.

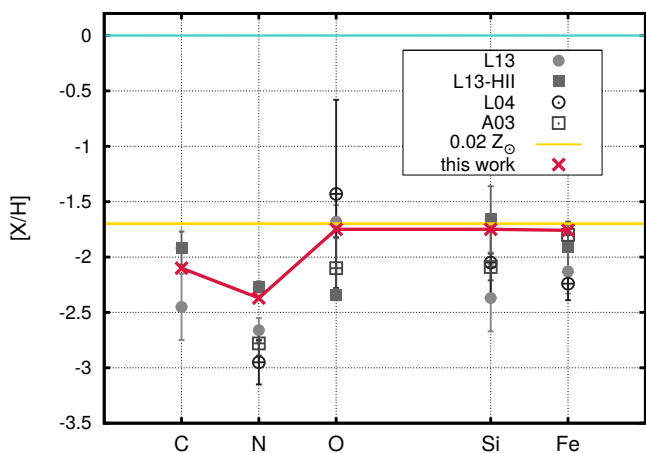


Fig. 1. Recent measurements of abundances in I Zw 18 compared to our applied composition (i.e. SMC composition scaled down by ten; shown by a red line with crosses). Carbon, nitrogen, oxygen, silicon and iron abundances are given relative to solar (Asplund et al. 2009): $[X/H]=\log(X/H)-\log(X/H)_{\odot}$. *L13*: first column of Table 7 in Leboutteiller et al. (2013). *L13-HII*: last column of the same table, composition of the HII regions. *L04* and *A03*: data of previous measurements, taken from Lecavelier des Etangs et al. (2004) and Aloisi et al. (2003), respectively. $0.02 Z_{\odot}$: solar abundances of Asplund et al. (2009) scaled down by a factor of 50.

Fig. 2 shows the metallicities of the local group galaxies SMC and LMC (as in Brott et al. 2011), and of the Sun (Asplund et al. 2009) as well as the metallicity of our I Zw 18 models. The zero value corresponds to the nearly metal-free first stars in the Universe called Population III stars. The metallicity of I Zw 18 is very close to that of Pop III stars on a linear scale; however, there

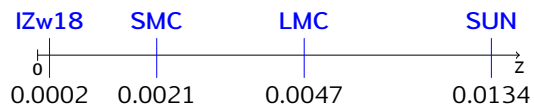


Fig. 2. Metallicities on a linear scale. SUN: solar metallicity given by Asplund et al. (2009). LMC, SMC: Large and Small Magellanic Clouds (Hunter et al. 2007; Brott et al. 2011). IZw18: $Z_{\text{IZw18}} \approx 0.1 \times Z_{\text{SMC}}$. The zero value corresponds to the metal-free Pop III stars.

are differences between our models and models of Pop III stars (see Sect. 10, Yoon et al. 2012, and Szécsi et al. in prep.).

For the initial value of helium, we assume that the mass fraction scales with the metallicity between the primordial helium mass fraction (Peimbert et al. 2007) and the solar value (Grevesse et al. 1996). Thus, the initial helium abundance in our $Z_{\text{ini}}=0.0002$ stellar models is $Y_{\text{ini}}=0.2477$.

Radiative opacities were interpolated from the OPAL tables (Iglesias & Rogers 1996) with solar-scaled metal abundances, with their iron abundance used as the interpolation parameter for metals. Our models thus correspond to a metallicity of $[\text{Fe}/\text{H}]=-1.7$ and $Z \approx Z_{\odot}/50$.

2.2. Physics of the stellar interior

All the mixing processes considered here are modelled as diffusive processes. Convection is treated according to the mixing-length theory (MLT) (Böhm-Vitense 1958) with an MLT parameter of $\alpha_{\text{MLT}} = 1.5$ (Langer 1991). Semi-convection is considered with an efficiency parameter of $\alpha_{\text{SEM}} = 1$ (Langer et al. 1983; Langer 1991), although it has minor effects on the models during the main-sequence evolution. As no calibration of the convective core overshooting parameter exists for stars of the considered metallicity, we rely on the work of Brott et al. (2011) who calibrated the overshooting against the rotational properties of B-type stars from the VLT-FLAMES survey (Hunter et al. 2008; Vink et al. 2010) as $\alpha_{\text{over}} = 0.335 H_p$, where H_p is the local pressure scale height. It has been suggested by Castro et al. (2014) and confirmed by McEvoy et al. (2015) that convective core overshooting of Galactic stars is probably mass-dependent and, at high mass ($\geq 15 M_{\odot}$), stronger than previously thought. However, the metallicity dependence of this effect still needs to be investigated.

Rotationally-induced mixing of chemical elements is treated with an efficiency parameter $f_c = 0.0228$ (Heger et al. 2000; Heger & Langer 2000), calibrated by Brott et al. (2011). Furthermore, transport of angular momentum by magnetic fields due to the Spruit–Taylor dynamo (Spruit 2002; Heger et al. 2005) is included, which is assumed here not to lead to additional transport of chemical elements (Spruit 2006; Suijs et al. 2008).

2.3. Mass-loss

For the early evolutionary stages of our models, we use the mass-loss rate prescription of Vink et al. (2000), which includes a bi-stability jump at ~ 25 kK. The dependence of mass-loss on the metallicity is additionally implemented according to Vink et al. (2001) as $\dot{M} \sim Z^{0.86}$. Approaching the empirical Humphreys–Davidson limit (thought to be connected to the Eddington limit), O and B stars may experience an increase in mass-loss, which is taken into account by using the empirical mass-loss rate prescription of Nieuwenhuijzen & de Jager (1990) (with the same

Z dependence as above) if its predicted mass-loss rate is higher than that of Vink et al. (2000, 2001) at any effective temperature smaller than ~ 22 kK.

Since we find some of our models to evolve into cool supergiants ($T_{\text{eff}} \lesssim 12$ kK) even during their main-sequence lifetime, we need to take the mass-loss of cool supergiant stars into consideration. In general, mass-loss of such stars is observed to be higher than that of O and B stars due to the low surface gravity at their large radii ($>1000 R_{\odot}$) and possibly due to dust formation in cool atmospheres (Groenewegen et al. 2009). However, quantitative physical models of such winds still have deficiencies, hence we rely on the empirical parametrization of the mass-loss rate following the prescription of Nieuwenhuijzen & de Jager (1990). This prescription is a revised version of that of de Jager et al. (1988), which has been shown by Maun & Josselin (2011) to be still applicable in the light of new observations of *bona-fide* red supergiants. The metallicity dependence of these winds is implemented as $\dot{M} \sim Z^{0.85}$ according to Vink et al. (2001). This formula is in accordance with the results of Maun & Josselin (2011) who find that the metallicity exponent should be between 0.5 and 1.

Our calculations predict strong surface helium enrichment even during core hydrogen burning as a result of fast rotation (see Sects. 6 and 7). We use the prescription of Hamann et al. (1995) for the winds of our models when the surface helium abundance is $Y_{\text{S}} \geq 0.7$ with reduction by a factor of 10 as suggested by Yoon et al. (2006). This reduction gives a mass-loss rate comparable to the most commonly adopted one by Nugis & Lamers (2000) (see Fig. 1 of Yoon 2015). The Hamann et al. (1995) prescription is applied together with a metallicity dependence of $\dot{M} \sim Z^{0.86}$ (Vink et al. 2001). For stars with surface helium abundances of $0.7 \geq Y_{\text{S}} \geq 0.55$, we interpolate linearly between the reduced Hamann et al. (1995) mass-loss rate and the rate of Vink et al. (2000, 2001).

A mass-loss enhancement is implemented for stars rotating near their critical rotation which includes their Eddington factor (Langer 1997; Yoon & Langer 2005). It remains unclear whether rapid rotation *per se* leads to an increase in mass-loss (Müller & Vink 2014). However, as discussed in Müller & Vink (2014), it still appears reasonable to consider that the mass-loss rate does increase close to the Eddington limit (Langer 1997; Gräfener et al. 2011).

3. The grid of stellar models

Stellar model sequences were computed under the physical assumptions described in Sect. 2. Each sequence is represented by one dot in the diagram in Fig. 3.

The distribution of the sequences in the initial parameter space is chosen to support a study of synthetic populations. For such a study, an interpolation between the sequences would be needed, which is easier to do if the model grid is dense enough – especially in the regions where the models are most varied. Therefore, we increased the number of computed models in the yellow region, which represents the transition between normal and chemically-homogeneous evolution, because these models show more variations. Additionally, we increased the number of computed models in the corner of the very massive slow rotators (which become core-hydrogen-burning cool supergiants) in order to study their evolution in more detail.

The initial masses of the models in our grid are chosen roughly equidistant on a logarithmic scale. The most massive stars found so far in the local universe are suggested to have an initial mass around $300 M_{\odot}$ (Crowther et al. 2010; Schneider

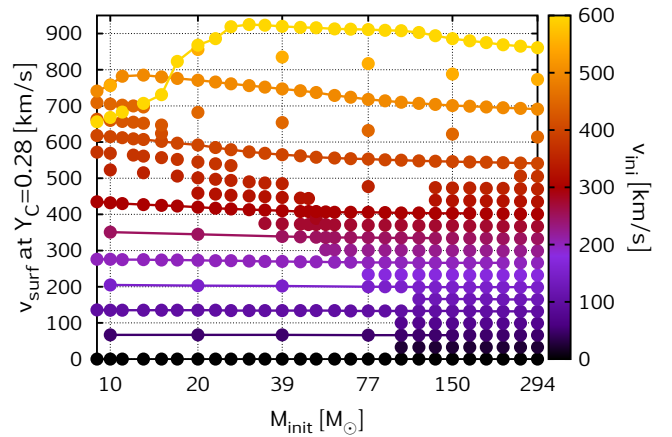


Fig. 4. Surface rotational velocity at the ZAMS (cf. Sect. 3.1). Every dot represents one evolutionary sequence, cf. Fig. 3. The colours refer to the *initial* surface rotational velocity, v_{ini} . Sequences with $v_{\text{ini}}=50, 100, 125, 150, 200, 250, 300, 400, 500$ and 600 km s^{-1} are connected by lines.

et al. 2014). Therefore, while stars more massive than this might be important in the presence of a top-heavy initial mass function (e.g. Ciardi et al. 2003; Dabringhausen et al. 2009) or in large starbursts (Treu et al. 2010; Sonnenfeld et al. 2012; Chabrier et al. 2014), we use $294 M_{\odot}$ here as an upper limit.

The colouring of the dots in Fig. 3 represents the surface helium mass fraction at the end of the main sequence (cf. Sect. 7). The red, yellow and blue regions indicate the type of evolution a given model undergoes, as described in Sects. 3.3 and 7.

3.1. Rotational velocities

The Y-axis in Fig. 3 refers to the initial equatorial rotational velocity at the surface of our models. We chose to cover a wide range in initial rotational velocity from zero up to 600 km s^{-1} . The models start out chemically homogeneous and in hydrostatic and thermal equilibrium initially. We emphasize that the initial rotational velocities refer to the values with which the calculations were started, and are generally significantly lower than the rotational velocity after hydrogen burning has reached CNO equilibrium, i.e. at central helium abundance $Y_{\text{C}} \simeq 0.28$ (Fig. 4). We define this point in time as the zero-age main-sequence (ZAMS). The reason for the rotational velocity at the ZAMS being higher than initially is that at the beginning of the calculation, the star undergoes a short phase of structural changes while approaching CNO equilibrium. During this adjustment phase, the star contracts, spins up and thus continues its evolution with increased rotation. On average, our models rotate about 30% faster than the nominal (i.e. Y-axis in Fig. 3) initial rotational velocity indicates.

Stellar models in the left top corner of Fig. 4 with $M \leq 17 M_{\odot}$ and $v_{\text{ini}}=600 \text{ km s}^{-1}$ rotate slower at the ZAMS than models with $v_{\text{ini}}=500 \text{ km s}^{-1}$. This is because although the models with $v_{\text{ini}}=600 \text{ km s}^{-1}$ also spin up initially, they nearly reach their Keplerian velocity during the early contraction phase. Stellar models close to the breakup rotation undergo enhanced mass-loss, so they lose mass and spin down at the beginning of the evolution. In this phase, the one-dimensional models only provide crude approximations of fast rotating stars (see e.g. Decressin et al. 2007; Chiappini et al. 2011; Krtićka et al. 2011; Espinosa Lara & Rieutord 2013, for a discussion of stars close to the breakup

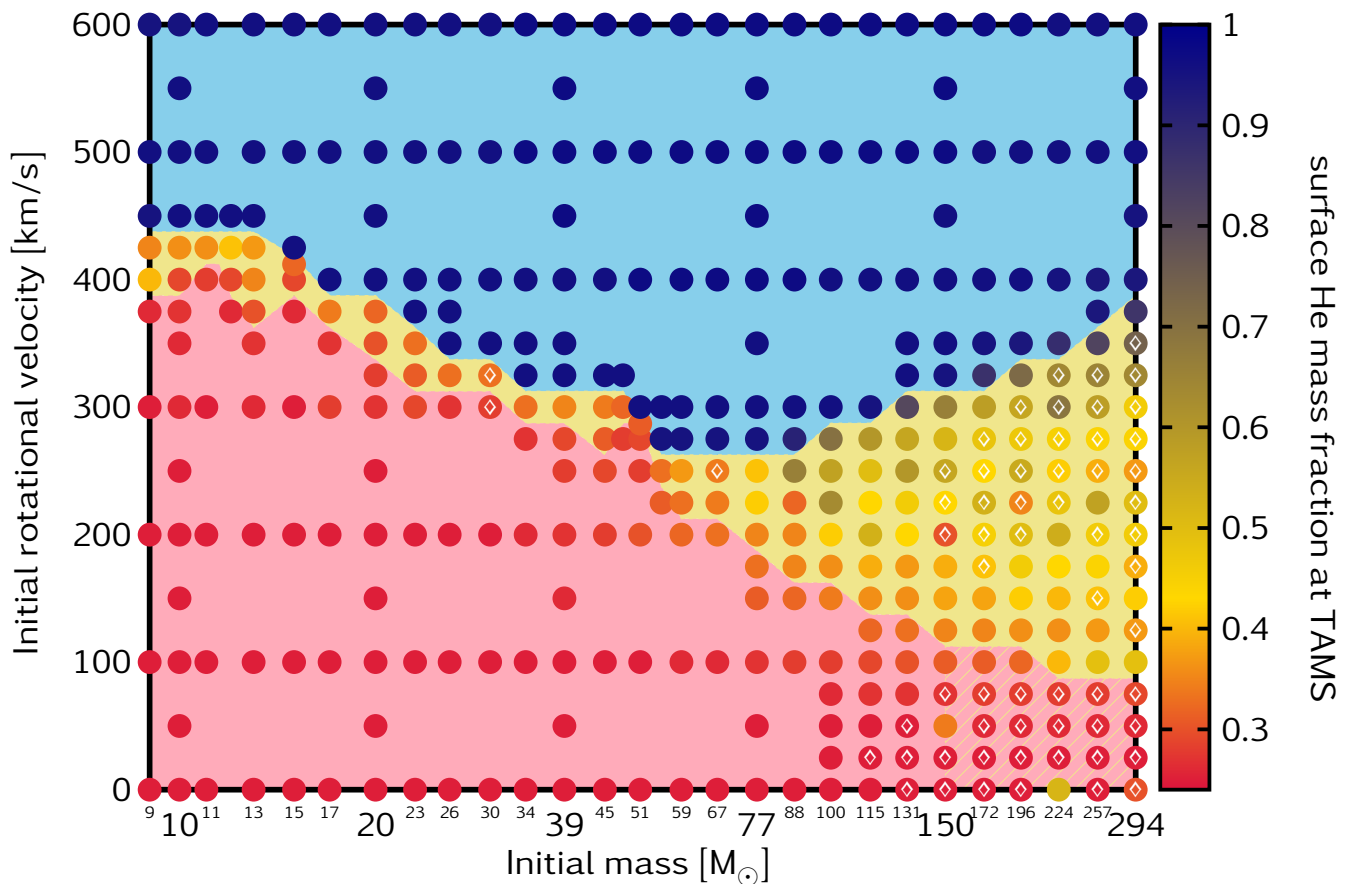


Fig. 3. Grid of 375 evolutionary sequences of single stars. Each evolutionary sequence of our grid is represented by one dot in this diagram. Sequences inside the blue shaded region follow chemically-homogeneous evolutionary paths evolving bluewards in the HR diagram and having a surface helium abundance of $Y_S \approx 0.98$ at the TAMS. Sequences inside the red region follow normal evolution, keeping Y_S close to the initial value of ≈ 0.24 . Sequences inside the yellow region deviate from normal evolution: either they start their lives evolving chemically homogeneously and then switch to normal evolution, or they start normal evolution and mass-loss uncovers their helium-rich layers (cf. Sect. 7). Diamonds mark the sequences that have not reached the TAMS (i.e. the calculation was stopped between $0.82 < Y_C < 0.98$), and the yellow-dashed pattern indicates that the separation line between the red and yellow regions is uncertain at the highest masses.

rotation). In particular, when the surface rotational velocity approaches the break-up velocity, angular momentum may be removed by losing mass into an equatorial, viscous decretion disc, as discussed by Krtićka et al. (2011). The effects of the decretion disc on the evolution of our fast rotating massive stars still remains to be studied.

3.2. Normal, homogeneous and transitional evolution

The grid in Fig. 3 consists of 375 sequences, from which 142 are classified as normal evolution (NE), 123 as (quasi) chemically-homogeneous evolution (CHE), and 110 as transitional evolution (TE). The calculation of some sequences with NE and TE were stopped before reaching the TAMS due to numerical difficulties. However, all the sequences in the grid reached a core helium mass fraction of $Y_C \gtrsim 0.82$. In Fig. 4, the sequences that were not followed until the TAMS are marked.

Models with NE develop a core-envelope structure: the core is chemically mixed through convection and fuses hydrogen into helium, while the envelope largely retains its initial composition. Their radii increase during the main-sequence lifetime because a chemical gradient develops and because the envelope inflates in the case of the highest-mass models (see the discussion in

Sect. 5). We also refer to Sect. 4 for the discussion of the HR diagram, in which the models evolve towards lower effective temperatures (redwards).

Chemically-homogeneous evolution was first described by Maeder (1987) in the context of rotation. Several authors have since investigated this evolutionary behaviour (see e.g. Yoon & Langer 2005; Yoon et al. 2006; Cantiello et al. 2007; Meynet & Maeder 2007) and have reported observational support for it (Walborn et al. 2004; Eldridge & Stanway 2012; Martins et al. 2013). Models with CHE develop only shallow chemical gradients between the core and the envelope and all the nuclear products are mixed throughout the star and reach the surface. We investigate their surface helium abundance and the optical depth of their winds in Sect. 6.

Transitional evolution was introduced by Yoon et al. (2012) for Pop III sequences where the surface helium mass fraction Y_S becomes larger than 0.7 at the TAMS, but the post-main-sequence evolution proceeds redwards. However, in their grid of 51 stellar sequences, only three sequences were identified as TE. We decided to use this expression in a broader sense: to describe a behaviour when the model starts evolving homogeneously and, at some point of the main-sequence lifetime, turns to normal evolution due to angular momentum loss in the stellar

wind (see also Sect. 7). Note that this revised definition of TE considers only the main-sequence phase.

3.3. The structure of the grid

In this section, we analyse the grid of stellar sequences shown in Fig. 3. A prominent feature for our grid is the shape of the transition region shown in yellow in Fig. 3. This region is narrow in the lower-mass regime (9-55 M_{\odot}). For higher masses (55-294 M_{\odot}), however, it covers a larger range of initial rotational velocities. The higher the mass, the more sequences follow TE.

At masses lower than $\sim 55 M_{\odot}$ in Fig. 3, the bifurcation between NE and CHE is sharp, and there is a very small transitional region between them. For these masses, the initial rotational velocity at which a star evolves homogeneously decreases with the initial mass. This is consistent with the finding of Yoon et al. (2012), who showed for stars in the mass range of 13-60 M_{\odot} that the ratio of the timescale of the Eddington–Sweet circulation τ_{ES} , which governs the mixing in our models, and the main-sequence lifetime τ_{MS} is systematically smaller for a higher-mass star. The ratio τ_{ES}/τ_{MS} becoming lower with mass is related to higher radiation pressure and lower density in higher-mass stars. Therefore, for a given initial rotational rate, CHE is favoured in higher-mass stars. Although Yoon et al. (2012) applied this reasoning to metal-free massive stars, our low-metallicity stellar models nevertheless follow the same principles.

In the regime above 55 M_{\odot} in Fig. 3, mass-loss effects are contributing significantly. Mass-loss influences the evolution at least in two ways. First, mass-loss removes angular momentum (Langer 1998). This can make an initially fast rotating star spin down and turn to normal, redwards evolution. Second, if enough mass is lost, deeper, helium-rich layers can be uncovered. This way the star appears more blue. Which effect of these two is more dominant, depends on the actual angular momentum and the size of the convective core, as explained below.

Slow rotators follow normal redward evolution, and angular momentum loss has no significant effect on them. At masses $\geq 80 M_{\odot}$, slowly rotating ($v_{ini} \lesssim 100 \text{ km s}^{-1}$) models evolve into cool supergiants before core-hydrogen exhaustion due to envelope inflation (Sect. 5). As we show in Sect. 7, these supergiant models may expose helium-rich layers near the TAMS due to the strong mass-loss and the deep convective envelope. Therefore, some of them are marked by orange coloured dots in Fig. 3.

The normally-evolving models that are close to the yellow transition region also have orange colours. This implies that there is no clear separation between normally-evolving and transitional-evolving models in the mass range 100-294 M_{\odot} . The transition here happens smoothly, and the separation line between the red and yellow regions that we draw in Fig. 3 in this mass range is somewhat arbitrary.

Additionally, as Fig. 4 shows, for most of the sequences in the bottom right corner of the grid the calculation of the last model did not converge, so the simulations were stopped before reaching the TAMS. If these sequences were continued until $Y_C=0.98$, they would probably expose deeper layers and would also appear more orange in Fig. 3, and that would move the separation line between the red and yellow regions towards slower rotations, so we marked this uncertain part of the diagram with a dashed pattern. However, the fact that some of the models are unevolved does not explain all the diversity in the surface helium and the colours in the bottom right corner of the grid in Fig. 3. The two consequences of mass-loss (the induced spin down due to angular-momentum loss and the uncovering of the

deep-lying helium-rich layers) shape the surface properties of the models at the TAMS. Additionally, these models increase their radii, making the stars appear more red and, due to the effective core-envelope coupling (Sect. 9.1), spin up. The consequence of these two competing mechanisms is that the models in the bottom right corner of the grid show diversity in the surface helium value at the TAMS (and also in the surface rotational velocity at the TAMS, as we discuss in Sect. 9.2.1).

At moderate initial rotation ($\sim 200\text{-}350 \text{ km s}^{-1}$) angular momentum loss is important for very massive stellar models ($\geq 88 M_{\odot}$) and can turn the evolution from homogeneous to transitional. The loss of angular momentum causes mixing to become inefficient. A star with inefficient mixing starts to possess a steep chemical gradient between the mixed core and a non-mixed envelope. This prevents CHE for the very massive stellar models in the upper part of the transitional region. Their spindown behaviour shapes the boundary between the blue and yellow regions: models with TE in the yellow region would be models with CHE if there were no mass and angular momentum loss. The borderline velocity between the blue and the yellow region is increasing with mass above 55 M_{\odot} .

If the rotation is fast enough, mass-loss cannot spin the star down enough to prevent the overall mixing. The fastest rotators therefore undergo CHE over their whole lifetime. They are enclosed in the blue region in Fig. 3.

Summarising, the slowest initial rotation (250 km s^{-1}) showing chemically-homogeneous evolution occurs for stars of 55-88 M_{\odot} . Stars less and more massive than this need to rotate faster than 250 km s^{-1} initially to follow a homogeneous evolutionary path, because either the Eddington–Sweet timescale is too large (in the case of the lower-mass regime) or too much angular momentum is lost in the wind (in the case of the higher-mass regime).

4. Evolutionary tracks in the HR diagram

In this section, we discuss the evolution of our low-metallicity massive stars in the HR diagram (see Fig. 5). The tracks that are plotted constitute a representative subset of our grid. Here we summarise their typical behaviour.

Slow rotators ($v_{ini}=0\text{-}200 \text{ km s}^{-1}$ in Fig. 5, more precisely those in the red region of Fig. 3) evolve from the ZAMS towards lower effective temperatures (i.e. *redwards*) and towards higher luminosities, which represents normal evolution. In contrast, fast rotating stars ($\geq 500 \text{ km s}^{-1}$ in Fig. 5, those in the blue region of Fig. 3) turn towards higher temperatures (bluewards) from the beginning, following CHE (Maeder 1987). The bifurcation between redward NE and blueward CHE has been studied by e.g. Brott et al. (2011) who showed that the lower the metallicity, the more predominant the CHE becomes.

Models shown in Fig. 5 with intermediate initial rotational velocities ($\sim 200\text{-}350 \text{ km s}^{-1}$) might evolve either normally or chemically-homogeneously, depending on their mass. In some cases, however, we can classify them neither NE nor CHE because the model shows properties of both evolutionary classes. For example, the 294 M_{\odot} model with 350 km s^{-1} evolves first chemically-homogeneously then turns to normal evolution, which is defined as transitional evolution (represented by the yellow region in Fig. 3).

The type of evolution is not only a function of the rotational velocity but also of the initial mass. In Fig. 5 one can observe the behaviour of the 350 km s^{-1} models: the lowest mass models (9-23 M_{\odot}) undergo NE, i.e. they evolve normally and redwards

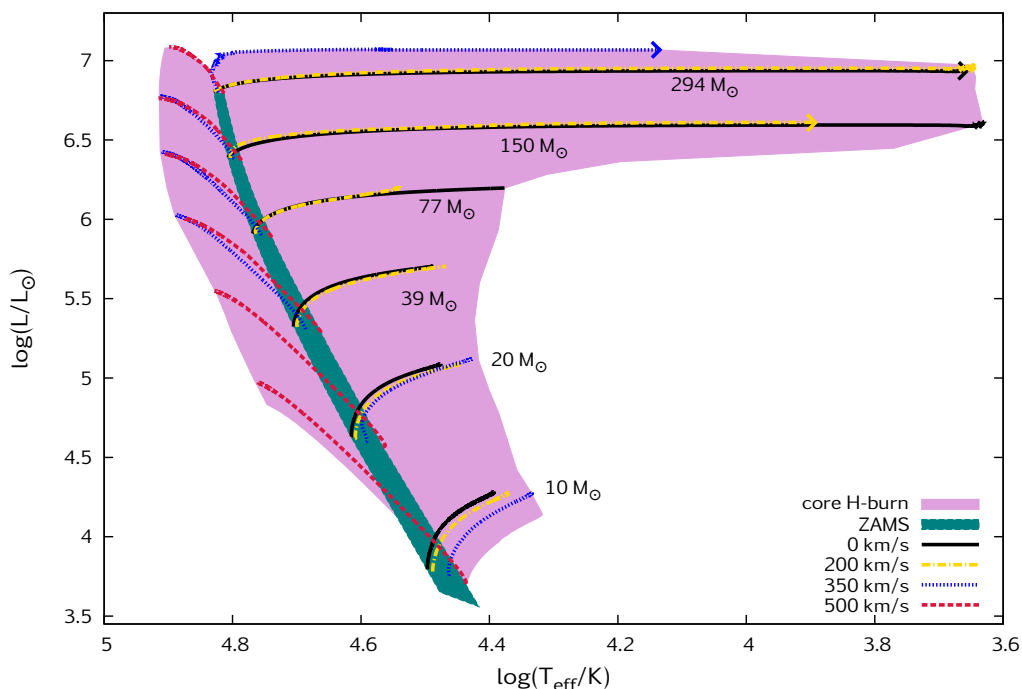


Fig. 5. Evolutionary tracks in the HR diagram during core hydrogen burning for models with initial masses between 9–300 M_{\odot} (see labels) and initial rotational velocities of 0, 200, 350 and 500 km s^{-1} , with a composition of $1/10 Z_{\text{SMC}}$. The lighter (purple) shading identifies the region in which all models of our grid undergo core hydrogen burning. The darker (green) shading identifies the zero-age main-sequence. An arrow marks the end of the tracks for models that were stopped before the terminal age main-sequence was reached. Core-hydrogen-burning objects are expected to be found on both sides of the ZAMS, inside the purple coloured region.

in the HR diagram, while higher mass models (26–257 M_{\odot}) undergo CHE, i.e. they evolve chemically-homogeneously and bluewards. The 294 M_{\odot} model with 350 km s^{-1} is a transitional case. We investigate the dependence of the evolutionary types on initial mass and rotation in Sect. 3.3.

The ZAMS positions of our models is shown by the green shaded region in Fig. 5. It is a broad region instead of a line due to the different rotation rates of the ZAMS models. Centrifugal acceleration reduces the effective gravity so while the radius of the rotating stellar model is higher, its temperature and luminosity are lower compared to a non-rotating stellar model of the same mass (cf. Fig. 3 in Köhler et al. 2015).

Purple shading in Fig. 5 represents the region which encloses all our models that burn hydrogen in their core. Due to the presence of the stars with CHE at this low metallicity, the purple main-sequence region encompasses the green ZAMS region. Our evolutionary calculations thus predict *hydrogen-burning massive stars to be found on both sides of the ZAMS*.

Some of the tracks stopped at the upper red side of the purple region due to numerical instabilities (see also the white diamonds in Fig. 4). Therefore, the upper borderline of the main-sequence region is approximate and might change (however not significantly) if all models were continued until $Y_C = 0.98$.

There is a significant difference between the redwards evolving lower- and higher-mass stellar sequences. Lower-mass ($\lesssim 80 M_{\odot}$) models stay more or less close to the ZAMS, never reaching $\log(T_{\text{eff}}/\text{K})$ values lower than ~ 4.3 . Higher-mass models, on the other hand, evolve all the way to the cool supergiant region ($T_{\text{eff}} < 12 \text{ kK}$) before core-hydrogen exhaustion. These high-mass objects are, therefore, *core-hydrogen-burning cool supergiants* during the last 5–15% of their main-sequence lifetimes.

5. Core-hydrogen-burning cool supergiants

The models of $\geq 80 M_{\odot}$ in our grid with slow or intermediate rotation rates spend the last 5–15% of their main-sequence evolution on the cool supergiant branch with $T_{\text{eff}} < 12 \text{ kK}$. We call this evolutionary phase the *core-hydrogen-burning cool supergiant phase*.

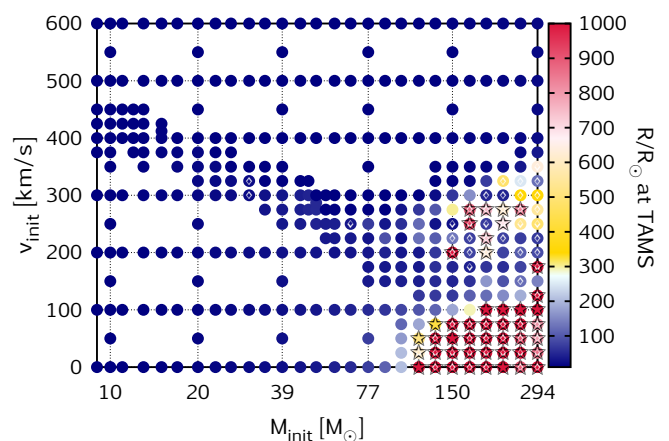


Fig. 6. Radius at the end of the main-sequence evolution as a function of initial mass and rotational velocity. The core-hydrogen-burning cool supergiants (defined as $T_{\text{eff}}^{\text{TAMS}} < 12 \text{ kK}$) are found at high mass and slow or intermediate rotation. We mark them with a star symbol. White diamonds mark the sequences that have not reached the TAMS (i.e. the calculation was stopped between $0.82 < Y_C < 0.98$).

Fig. 6 shows the radius of our stellar models at the TAMS. The fast rotating, chemically-homogeneously-evolving models

all remain compact and blue, while the massive ($M_{\text{ini}} \geq 80 M_{\odot}$) models with normal and transitional evolution expand during the main-sequence lifetime. They may reach T_{eff} values below 12 kK and radii larger than $1000 R_{\odot}$, and become core-hydrogen-burning cool supergiants near the TAMS.

The reason for the expansion of our massive unmixed models is their proximity to the Eddington limit. Köhler et al. (2015) and Sanyal et al. (2015) find that this occurs for stars above $\sim 50 M_{\odot}$ in LMC models, whose mass-loss, however, removes the hydrogen-rich envelope such that stars above $\sim 100 M_{\odot}$ do not become that cool. We note that even very massive zero-metallicity models have been shown to become red supergiants during core hydrogen burning (Marigo et al. 2003; Yoon et al. 2012).

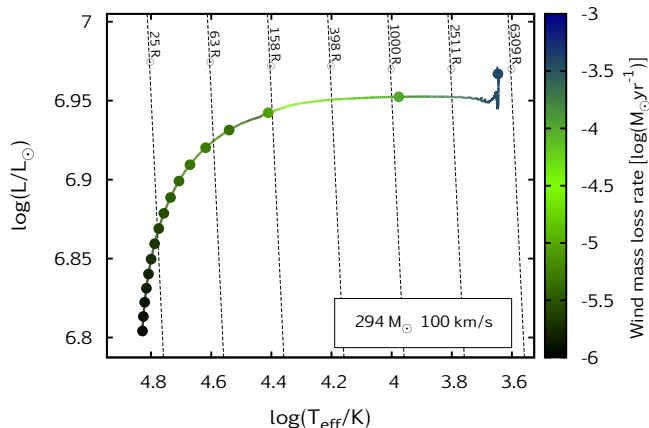


Fig. 7. Evolutionary track of our model with $M_{\text{ini}}=294 M_{\odot}$ and $v_{\text{ini}}=100 \text{ km s}^{-1}$ during core hydrogen burning in the HR diagram. Dots mark every 10^5 years of evolution. The stellar wind mass-loss rate is colour coded; black dashed lines of constant radii are labelled according to their radius value. The star becomes a core-hydrogen-burning cool supergiant during the last 15% of its main-sequence evolution.

Fig. 7 shows the evolution of our slowly rotating stellar sequence with $294 M_{\odot}$ in the HR diagram. After the first 1.5 Myr, the radius inflates from $150 R_{\odot}$ to $5100 R_{\odot}$ within 0.2 Myr. Thus, the model spends ~ 0.3 Myr (15% of the total main-sequence lifetime) as a core-hydrogen-burning cool supergiant before hydrogen exhausts in the core. During this time, the mass-loss rate is very high (up to $4 \cdot 10^{-4} M_{\odot}/\text{yr}$). The star loses mass rapidly and ends up with $244 M_{\odot}$ at the TAMS. However, it still retains a hydrogen-rich envelope of $\sim 60 M_{\odot}$ at this time.

As seen in Fig. 6, several sequences evolve similarly to the $294 M_{\odot}$ sequence discussed above, reaching surface temperatures below 12 kK. There are two distinct regions containing core-hydrogen-burning supergiants, one at high mass and slow rotation, and the other at high mass and around 275 km s^{-1} initial rotation. The slow rotators evolve normally during the first part of their main-sequence lifetimes, while those at intermediate rotation rates evolve homogeneously initially, and turn to normal evolution due to angular momentum loss (transitional evolution).

The stability of the extended envelopes of the core-hydrogen-burning cool supergiants is uncertain. Moriya & Langer (2015) suggest that their likely pulsational instability may lead to enhanced mass-loss. This may significantly shorten this evolutionary stage.

Nevertheless, should they exist, they may be extremely bright stars. As their bolometric correction is essentially

zero, the cool supergiants predicted by our model grid with $\log(L/L_{\odot})=6.3\dots 7$ would have visual magnitudes in I Zw 18, adopting a distance of 18 Mpc (Aloisi et al. 2007), in the range of 20.3 mag...18.6 mag. Brightness variations with periods of the order of months to years due to pulsations may reveal them as stars rather than star clusters in photometric multi-epoch observations.

There may also be other ways to look for core-hydrogen-burning cool supergiants in nature. According to our simulations, core-hydrogen-burning supergiants lose a significant amount of mass during the red supergiant phase. In the case of the $294 M_{\odot}$ star analysed above, for example, as much as $\sim 40 M_{\odot}$ of material is lost in the red supergiant wind. As the material lost in the wind has undergone CNO processing, the material that returns to the circumstellar gas pollutes the environment with hydrogen-burning products. The low wind velocity may allow this gas to be retained in the vicinity of the star-forming region which produced the cool supergiants, and thus pollute the gas from which further stars in the same region may form. E.g., our cool supergiants may have an impact on the understanding of abundance anomalies in globular clusters (Caretta 2010; Bastian et al. 2013, and Szécsi et al. in prep.).

6. Transparent Wind Ultraviolet Intense stars

Stars of all masses that evolve homogeneously mixed during their main-sequence lifetime occupy the left purple region in Fig. 5, i.e. blueward from the ZAMS.

These models have OB-type mass-loss initially. WR-type mass-loss is adopted for $Y_{\text{S}} > 0.7$, see the top panel in Fig. 8. Therefore, from the evolutionary point of view, these models might be considered as core-hydrogen-burning WR stars. However, from the observational point of view, WR stars are characterized by the presence of strong emission lines, which indicate optically-thick winds. We estimate the optical depth of their winds following Eq. (14) of Langer (1989) as:

$$\tau(R) = \frac{\kappa \dot{M}}{4\pi R(v_{\infty} - v_0)} \ln \frac{v_{\infty}}{v_0}, \quad (1)$$

where R designates the radius of the stellar model without taking the wind into account. This equation is derived from a β -velocity law with $\beta=1$. In that, we use the electron scattering opacity $\kappa = \sigma(1 + X)$, σ being the Thomson scattering cross-section, an expansion velocity of $v_0=20 \text{ km s}^{-1}$ at the surface of the stellar model, and a terminal wind velocity of $v_{\infty} = \sqrt{\frac{GM}{R}}$.

Fig 8 (bottom panel) shows the optical depth of the stellar winds as calculated from Eq. (1) for our homogeneously-evolving stellar models. The behaviour of the wind optical depth seen in this figure is mostly related to the mass-loss rate (cf. Sect. 8), which is increasing with mass. While these numbers are only approximate, they show that the winds of the lower-mass ($M_{\text{ini}} \lesssim 80 M_{\odot}$) models with CHE, even when applying WR-type mass-loss, remain optically thin ($\tau < 1$) throughout their main-sequence lifetime. Even the higher-mass models ($M_{\text{ini}} \geq 80 M_{\odot}$) keep optically-thin winds for most of core hydrogen burning, and the wind optical depth does not exceed $\tau \approx 3$ even up to core hydrogen exhaustion for the most luminous stars.

Our fully mixed stars are extremely hot (up to $T_{\text{eff}} \approx 80 \text{ kK}$) and bright (up to $10^7 L_{\odot}$) objects which have an optically-thin wind. Additionally, they emit intense mid- and far-UV radiation (see also Sect. 10), so we call them Transparent Wind Ultraviolet Intense stars or TWUIN stars.

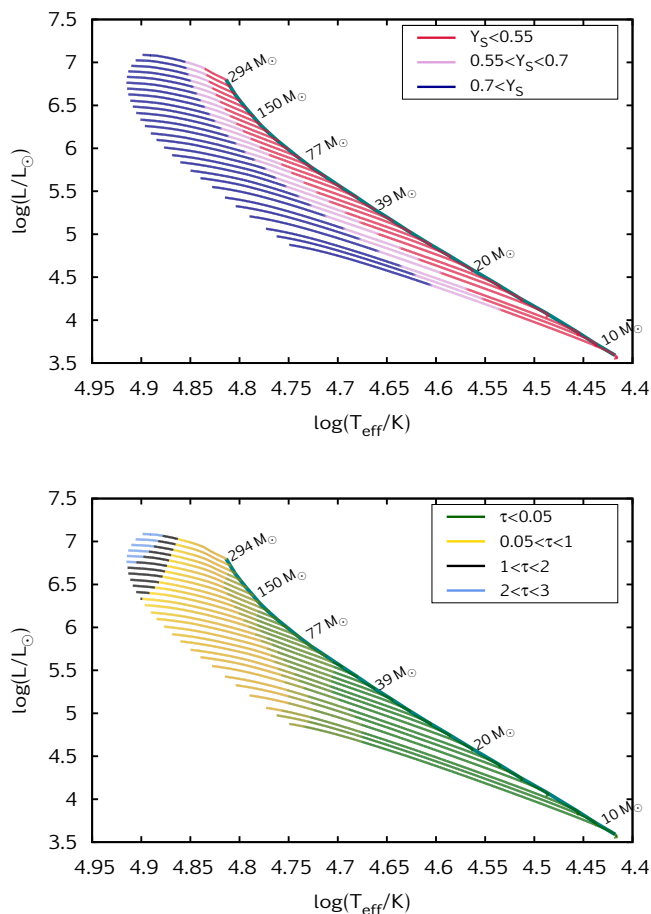


Fig. 8. *Top:* HR diagram of models with $v_{\text{ini}}=500 \text{ km s}^{-1}$ (chemically-homogeneous evolution) and masses between 9-294 M_\odot . The thick green line marks the ZAMS. The colouring marks the surface helium mass fraction as indicated by the legend. For $Y_S < 0.55$, OB-type mass-loss is applied; for Y_S between 0.55 and 0.7, an interpolation between OB- and WR-type mass-loss is applied; and for $Y_S > 0.7$, WR-type mass-loss is applied (cf. Sect. 2.3). *Bottom:* HR diagram of the same collection of models as above. The colouring marks the wind optical depth τ according to Eq. (1).

We emphasize that TWUIN stars are only expected at very low-metallicity. Their mass-loss, which depends on the metallicity, is not strong enough to spin them down to prevent homogeneous evolution (Szécsi et al. in prep.). They remain compact, i.e. the radii remain small, typically around 10-20 R_\odot . Additionally, they develop no core-envelope structure, so most of the hydrogen in the envelope is mixed into the burning regions and converted into helium. TWUIN stars therefore finish their main-sequence evolution as massive fast-rotating helium stars which make them strong candidates for long-duration gamma-ray bursts (Yoon & Langer 2005; Woosley & Heger 2006). Their rotational rate at the TAMS is discussed in Sect. 9.2.2.

7. The helium abundance at the surface and in the core

In the surface helium vs. central helium mass fraction (Y_S - Y_C) diagram, every stellar evolutionary sequence can be represented by one line, and the core helium mass fraction merely serves as a clock. During the core-hydrogen-burning stage, the slope of the line tells us about the efficiency of mixing helium from the

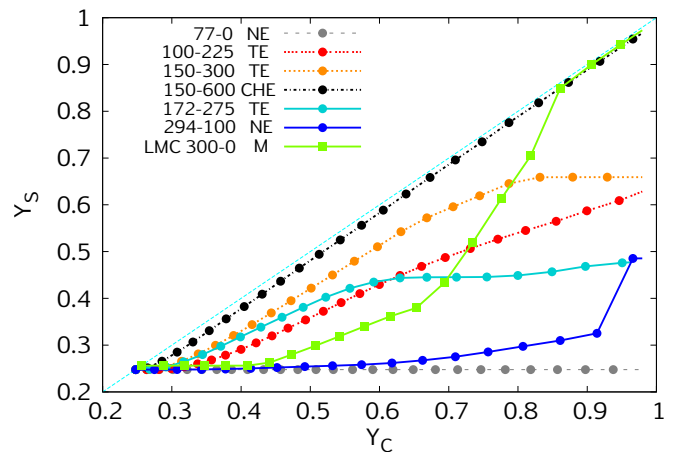


Fig. 9. Mass fraction of helium at the stellar surface (Y_S) as a function of that in the core (Y_C) for sequences of different initial masses and rotational velocities as indicated by the legend, in units of $M_\odot\text{-km s}^{-1}$. Dots mark every 10^5 years of the evolution. The diagonal line ($Y_C=Y_S$) is marked by a lightblue (dashed) line. Stars that evolve chemically-homogeneously (CHE) lie close to the diagonal, while those that undergo normal evolution (NE) trace a horizontal line; stars with transitional evolution (TE) lie between (see also Fig. 3). One non-rotating sequence (of type M) with $M_{\text{ini}}=300 M_\odot$ from the LMC grid of Köhler et al. (2015) is shown for comparison.

core through the radiative envelope to the surface by rotation-induced turbulence. Thus, the steeper the slope, the more helium reaches the surface. Tracks of normally-evolving stellar models form a horizontal line while tracks of homogeneously-evolving models lie close to the diagonal in the Y_S - Y_C diagram. Furthermore, tracks of models with transitional evolution lie between the horizontal and the diagonal lines. Consequently, it is easy to distinguish these three evolutionary behaviours in the Y_S - Y_C diagram.

Fig. 9 presents some of our stellar sequences in the Y_S - Y_C diagram. The non-rotating sequence of 77 M_\odot evolves close to the X-axis of the Y_S - Y_C diagram, which indicates that there is no mixing between the core and the surface.

Sequences of intermediate rotational velocities (such as the models of 100 M_\odot -225 km s^{-1} , 150 M_\odot -300 km s^{-1} and 172 M_\odot -275 km s^{-1}) start their life homogeneously and with a slight rise in the Y_S - Y_C diagram, but after a while they lose enough angular momentum so they turn to normal evolution and show a horizontal slope in the diagram. Therefore, we consider these sequences having transitional evolution.

Fast rotating sequences of 600 km s^{-1} undergo CHE, turning bluewards in the HR diagram and following the diagonal line in the Y_S - Y_C diagram. In these models, the ashes of nuclear burning are mixed between the core and the surface, enhancing the surface with burning products (e.g. helium) and supplying unprocessed material to the hydrogen-burning region.

Köhler et al. (2015), who analysed stellar models with LMC composition, introduced Type M evolution, which stands for an evolutionary behaviour during which mass-loss is so efficient that the homogeneous layers of the stellar interior are uncovered. Fig. 9 shows one LMC sequence which is of Type M.

None of our sequences undergo evolution classified as Type M. This is simply because the mass-loss at our low-metallicity is less effective than at LMC metallicity. Although some sequences (e.g. the one with 294 M_\odot and 100 km s^{-1} in

Fig. 9) show effects of mass-loss near the TAMS, this effect is not strong enough to make the model homogeneous (i.e. $Y_C \approx Y_S$).

The evolution leading to a core-hydrogen-burning cool supergiant star (Sect. 5) is represented by the track of $294 M_\odot$ with 100 km s^{-1} initial rotation in Fig. 9. During the last $\sim 10^5$ years of the simulated evolution, the surface helium abundance increases rapidly for two reasons. The first reason is that the supergiant mass-loss takes over, leading to a significant increase in the surface helium abundance. The second reason is that a deep convective envelope develops in the outer layers of the star, which dredges out helium from the core. This model spends the last phase of its main-sequence evolution (between $Y_C \gtrsim 0.92$ and the TAMS) as a core-hydrogen-burning red supergiant with $T_{\text{eff}} \approx 4500 \text{ K}$.

Another example of a core-hydrogen-burning supergiant is given by the track of $172 M_\odot$ with 275 km s^{-1} initial rotational velocity. This model is categorised as transitional evolution, since Y_S increases with Y_C initially (as in the case of the homogeneously-evolving models). Between $0.6 \lesssim Y_C \lesssim 0.8$, however, Y_S stays constant (typical for normal evolution). At $Y_C \sim 0.8$, a slight increase in the surface helium abundance happens again as the sequence proceeds towards lower effective temperatures and the mass-loss becomes more effective. Amongst our core-hydrogen-burning cool supergiant models, the highest surface helium mass fraction we find is 0.52.

8. Mass-loss history

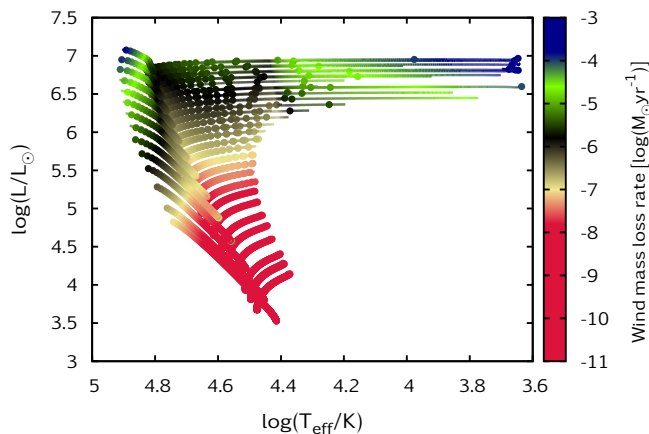


Fig. 10. HR diagram showing sequences with $v_{\text{ini}}=0$ and 500 km s^{-1} for all masses of our grid. Mass-loss rates are colour coded. Dots mark every 10^5 years of evolution.

While the mass-loss rates adopted for our models (Sect. 2.3) depend strongly on the initial metallicity (Vink et al. 2001, and Szécsi et al., in prep.), and our models lose less mass than their counterparts at, for example, LMC composition (Köhler et al. 2015), in the most extreme cases of the most massive TWUIN stars and the core-hydrogen-burning supergiants, our stellar models reach mass-loss rates as high as $4 \times 10^{-4} M_\odot \text{ yr}^{-1}$. This is demonstrated by Fig. 10, which shows the mass-loss rate of some of our models in the HR diagram.

Fig. 11 shows the M_{ini} vs. M_{TAMS} relation for our stellar sequences. Overall, none of the tracks deviate much from the diagonal line, meaning that the mass-loss is quite weak for our models. However, there are some differences in how much mass

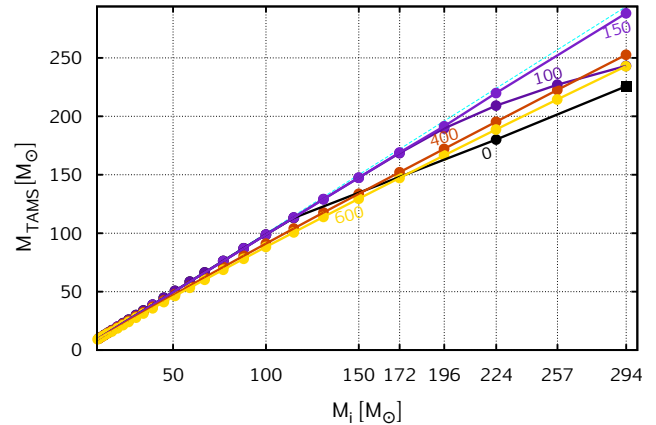


Fig. 11. Initial mass vs. final mass (at the TAMS). Every dot marks one evolutionary sequence. Sequences with the same initial rotational velocity v_{ini} are connected, labels indicate the value of the corresponding v_{ini} in km s^{-1} . Only models that evolved until the TAMS are shown, except for the non-rotating one with $M_{\text{ini}}=294 M_\odot$ (marked by a rectangle), for which the final mass is extrapolated.

the models with different evolutionary paths retain during their main-sequence lifetimes.

In the lower-mass regime ($\lesssim 100 M_\odot$), the fast rotating, chemically-homogeneously-evolving sequences of 400 and 600 km s^{-1} end up having less mass than the slow rotating, normally-evolving sequences. This is due to the WR-type mass-loss rate that applies for the sequences with CHE during the second part of their main-sequence evolution.

For the high-mass ($\gtrsim 100 M_\odot$) sequences, however, another behaviour is present: the very massive slow rotators (represented by the models of 0 - 100 km s^{-1} in Fig. 11) become core-hydrogen-burning cool supergiants. The efficiency of mass-loss increases when a star approaches the cool supergiant phase because the mass-loss prescription applied here has a radius dependence of $\dot{M} \sim R^{0.81}$. Thus, the mass-loss in this phase may be even stronger than the WR-type mass-loss, which means that stellar models that evolve to the cool supergiant phase during the main sequence may end up less massive than models with CHE of the same mass. Note that the model marked with a rectangle in Fig. 11 is stopped at $Y_C = 0.87$. For this model, we predicted the final mass based on the mass-loss rate in the last computed model and on the remaining hydrogen-burning lifetime.

Intermediate rotation rates (150 - 350 km s^{-1}) are represented by the models at 150 km s^{-1} in Fig. 11. These models eventually evolve normally but stay bluer due to enhanced surface helium abundance by rotational mixing (cf. models with TE in Fig. 9). They therefore undergo neither WR-type mass-loss nor cool supergiant mass-loss and only lose small amounts of mass due to the OB-type mass-loss that applies to them during their whole main-sequence lifetime.

9. Rotation

At higher metallicity (e.g. Solar or LMC), rotating massive stars would be spun down during the main-sequence evolution because of mass and angular momentum loss via winds (Langer 1998; Köhler et al. 2015). At the metallicity of I Zw 18, in contrast, mass-loss is less efficient and the stars can retain a more or less constant amount of angular momentum. If there are efficient

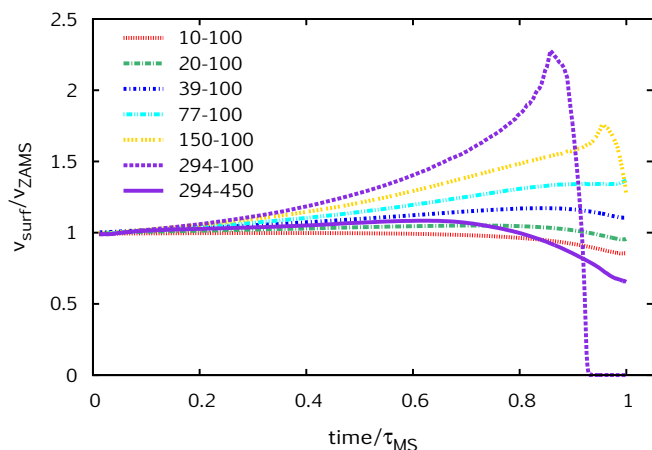


Fig. 12. Surface rotational velocity as function of time for models with different initial masses and rotational velocities as indicated by the legend (units are $[M_{\odot}]$ - $[\text{km s}^{-1}]$). The time is normalised to the main-sequence lifetime of the stars and the rotational velocity is normalised to the ZAMS value (see Sect. 3.1). The track of the $294 M_{\odot}$ - 450 km s^{-1} model which evolves chemically homogeneously is plotted with a dotted line for comparison.

mechanisms transporting angular momentum in the interior between the core and the envelope, the surface rotational velocity might increase during the main-sequence evolution even when the star evolves towards lower surface temperature and larger radius (Ekström et al. 2008; de Mink et al. 2013). In this section we show how this core-envelope coupling plays a role in shaping the rotational history of our stars.

9.1. Evolution of the surface rotational velocity

The evolution of the surface rotational velocity for some of our models is presented in Fig. 12. The surface rotation of the $10 M_{\odot}$ - 100 km s^{-1} model gradually decreases. Higher-mass models at 100 km s^{-1} from our grid, however, all increase their surface rotational velocity during the first $\sim 80\%$ of their main-sequence lifetime. The most massive models then reach a maximum and start a rapid decrease and spin down – in case of the $294 M_{\odot}$ - 100 km s^{-1} model all the way to zero. This sequence evolves into a core-hydrogen-burning cool supergiant.

To understand this behaviour we need to consider the following mechanisms. In our stellar models, angular momentum can be transported from the core to the envelope due to meridional circulations and shear turbulence, as well as by magnetic torques (Sect. 2.2). The angular momentum transport aims to make the whole star rotate with constant angular velocity. During the main-sequence phase of a normally-evolving model, the stellar core contracts, the envelope expands and the star evolves redwards in the HR diagram. Although the radius increases, angular momentum can be effectively transported from the contracting core outwards, at least during the first $\sim 80\%$ of the main-sequence lifetime. As a result, the surface rotational velocity of the star must increase during this evolutionary phase.

The star therefore spins up. According to Fig. 12, the maximum velocity depends on the initial mass, being greater for higher-mass objects. The reason of this mass dependence is that the higher the mass the more massive the stellar core. The angular momentum which is transported from this more massive core to the envelope is therefore higher. The rotation rate can increase to more than twice the initial value in the case of the

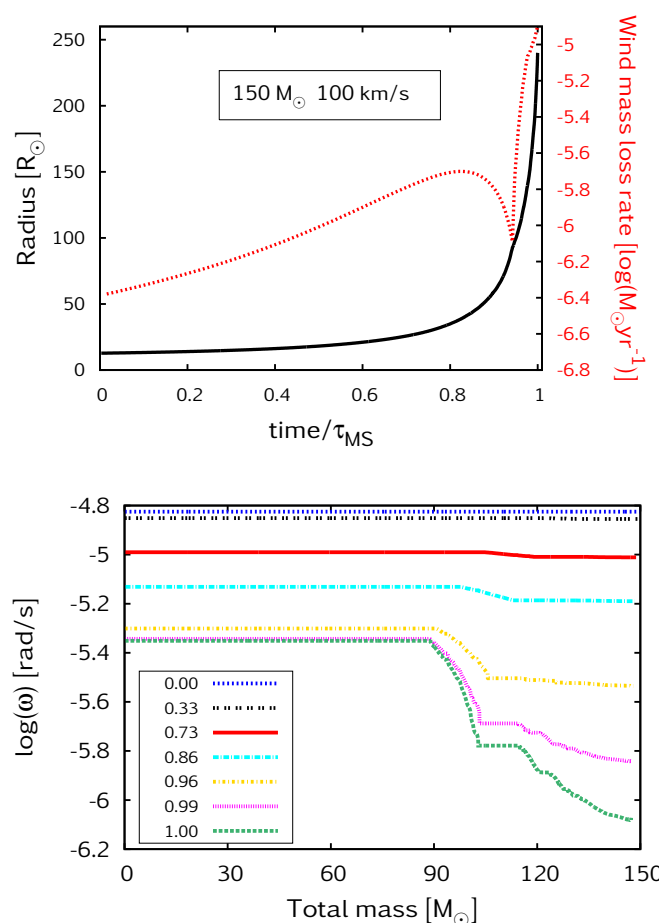


Fig. 13. *Top:* Radius and mass-loss rate as a function of the main-sequence lifetime for the stellar sequence with $M_{\text{ini}}=150 M_{\odot}$ and $v_{\text{ini}}=100 \text{ km s}^{-1}$ (yellow track in Fig. 12). *Bottom:* Angular velocity (ω) distribution inside the same sequence at the fractions of main-sequence lifetime, t/τ_{MS} , indicated by the legend, where $\tau_{\text{MS}} = t_{\text{C}}^{Y_{\text{C}}=0.98} - t_{\text{C}}^{Y_{\text{C}}=0.28}$.

$294 M_{\odot}$ model. In contrast, the $10 M_{\odot}$ model does not show any increase of surface rotation because its core is relatively small.

For the highest mass models of $150 M_{\odot}$ - 100 km s^{-1} and $294 M_{\odot}$ - 100 km s^{-1} , a sudden drop happens at $\sim 85\%$ and $\sim 95\%$ of the main-sequence lifetime, respectively. This is further illustrated by Fig. 13 which shows the evolution of the radius and the mass-loss rate, as well as the angular velocity distribution inside the $150 M_{\odot}$ model. The angular velocity is approximately constant until $t \approx 0.80 \tau_{\text{MS}}$. Then the radial expansion becomes so pronounced that the angular momentum transport through the core-envelope coupling cannot keep the star rigidly rotating and the surface layers slow down. Additionally, the mass-loss increases at $\sim 0.94 \tau_{\text{MS}}$ when the star encounters the bi-stability jump at $T_{\text{eff}} \sim 25 \text{ kK}$ (Vink et al. 2000). As a result, a significant amount of mass and angular momentum is lost contributing to the fast decrease of the surface rotational velocity.

At the TAMS, stars that have not become cool supergiants during the main-sequence still rotate rapidly (see also Sect. 9.2). The core-hydrogen-burning supergiants, represented by the $294 M_{\odot}$ - 100 km s^{-1} model in Fig. 12, have negligible surface rotation at the TAMS in our calculations.

Our results support the finding of Meynet & Maeder (2002) and Ekström et al. (2008) that normally-evolving stars may increase their surface rotation during the main-sequence evolution

if the mass-loss is low. This implies that the rotational velocity distribution of hydrogen-burning massive stars to be observed in low-metallicity environments is expected to be significantly different than that in higher-metallicity environments.

For fast rotators, the angular velocity distribution inside the star is always close to constant during the main-sequence lifetime. They are represented by the $294 M_{\odot}$ – 450 km s^{-1} model in Fig. 12. This model evolves with only a slight radius increase during the first half of the main-sequence. When the WR-type mass-loss turns on at $\sim 0.65 \tau_{\text{MS}}$, the mass-loss increases and spins the star down. However, WR-type mass-loss at this metallicity is not strong enough to remove all the angular momentum. Therefore these stars still rotate rapidly at the TAMS (see Sect. 9.2.2) and, if there is little angular momentum loss afterwards, also during their post-main-sequence phases (see Sect. 10.5).

9.2. Surface rotational velocity at the TAMS

Here we discuss the rotational rates of our models at the end of the main sequence. The rotational velocity of a model at the TAMS depends on its rotational behaviour during the main-sequence evolution, which in turn depends on the actual evolutionary path (normal, transitional or homogeneous evolution, as seen in Sect. 9.1). Also, we refer to Sect. 3.1 where we discuss the rotational velocities of our models at the ZAMS.

9.2.1. Redward evolving stars

Fig. 14 presents the surface rotational velocity of our models at the TAMS. Sequences that are marked by red star symbol or not marked with any symbol undergo normal or transitional evolution. In both cases, the models evolve redwards in the HR diagram.

Sequences in the left bottom corner of the figure with initial masses $\lesssim 26 M_{\odot}$ and initial rotational velocities $\lesssim 150 \text{ km s}^{-1}$ reduce their rotational velocity gradually, the same way as the sequence $10 M_{\odot}$ – 100 km s^{-1} in Fig. 12. The reason that their rotational velocities are still above 100 km s^{-1} at the TAMS is the spin up during the adjustment phase at the beginning of their evolution, as discussed in Sect. 3.1.

The rotational velocity at the TAMS of the higher-mass models (between 26 – $131 M_{\odot}$ in the case of the 100 km s^{-1} line) with slow initial rotation ($\lesssim 150 \text{ km s}^{-1}$) is an increasing function of the initial mass. As we have explained in the discussion of Fig. 12, this is because the higher the mass, the more angular momentum can be released by the contracting core and transported to the envelope. Stars more massive than $80 M_{\odot}$ have, in the last $\sim 20\%$ of the main-sequence lifetime, undergone envelope inflation. They have encountered the bi-stability jump and spun down in the same way as the models of $150 M_{\odot}$ – 100 km s^{-1} and $294 M_{\odot}$ – 100 km s^{-1} shown in Fig. 12. Those which rotate very slowly at the TAMS have evolved into core-hydrogen-burning cool supergiants. Accordingly, sequences with $T_{\text{eff}}^{\text{TAMS}} < 12 \text{ kK}$ are marked with large red star symbols.

Lower-mass ($\lesssim 50 M_{\odot}$) sequences with initial velocities of 200 – 300 km s^{-1} evolve normally. Their behaviour is similar to those of lower mass at 100 km s^{-1} : the surface rotational velocity at the TAMS is an increasing function of the initial mass. Higher-mass ($\gtrsim 50 M_{\odot}$) sequences with initial velocities of 200 – 300 km s^{-1} , on the other hand, have variable values of surface rotational velocity at the TAMS. They undergo transitional evolution. The following effects contribute significantly in shaping

their evolution. (1) mass-loss uncovers helium-rich layers, and the star appears bluer due to the lower opacities at the surface. Furthermore, the mass-loss, which depends on the surface composition and the effective temperature, removes angular momentum. (2) The radius increases during the main-sequence evolution, and the star appears redder. At the same time, the core contracts, and the star increases the surface rotational velocity due to the core-envelope coupling. The net effect of these competing mechanisms can be that the model at the TAMS is either fast rotating and blue, or slow rotating and red, or somewhere in between.

9.2.2. Homogeneously-evolving stars

The fastest rotators (400 – 600 km s^{-1}) are chemically-homogeneously-evolving TWUIN stars (marked in Fig. 14 with small blue stars). They undergo WR-type mass-loss at the TAMS (i.e. $Y_{\text{S}}^{\text{TAMS}} \geq 0.7$), mostly have optically thin winds (as seen in Sect. 6) and emit intense UV radiation (as seen in Sect. 10).

Low-mass ($\lesssim 20 M_{\odot}$) stars with CHE reach breakup rotational rates early during the main-sequence evolution because the breakup velocity is less for lower masses. When the models spin up to close to breakup, they manage to spin down again by losing mass through rotationally-enhanced stellar winds. As a consequence, they rotate slower at the TAMS than they would if they had not reached breakup rotation or if there was no rotationally-enhanced mass-loss included in the calculations. This is why the surface rotational velocity at the TAMS of the fast rotators increases at low mass and does not follow the decreasing trend of the more massive stars which undergo CHE. Although rotating massive stars at breakup have gained some interest in the past (Decressin et al. 2007), theoretical suggestions by Müller & Vink (2014) disfavour the concept of rotationally-enhanced stellar winds. Since the physical assumptions in these stellar models are currently under debate, we do not analyse this issue further at this point.

High mass ($>20 M_{\odot}$) sequences which undergo CHE, on the other hand, are hardly influenced by the rotational mass-loss enhancement. Their surface rotational velocity at the TAMS is decreasing as a function of the initial mass. This decreasing trend is a consequence of the stellar wind being more efficient at higher mass (but not efficient enough to turn them back to TE). Their typical behaviour is presented in Fig. 12 by the sequence $294 M_{\odot}$ – 450 km s^{-1} : their rotational velocity does not change much during the first two-thirds of their main-sequence lifetime, and then they slightly spin down due to the WR-type mass-loss. However, they still rotate at least as fast as 350 km s^{-1} at the TAMS. This fast rotation, if not reduced during the post-main-sequence evolutionary phases, might lead to the formation of a long-duration gamma-ray burst in the collapsar scenario (Sect. 10.5).

9.3. Surface nitrogen abundance and internal mixing

The surface nitrogen abundance of a star traces the internal mixing efficiency (e.g. Köhler et al. 2015). Fig. 15 shows the evolution of the surface nitrogen mass fraction for some of our stellar models relative to their surface hydrogen mass fraction. Three tracks are plotted for every mass representing the three classes of evolution (NE, TE, CHE). Due to hydrogen-burning, the N/H ratio cannot decrease during the main-sequence lifetime plotted here. The CNO equilibrium abundance of nitrogen for normal hydrogen and helium abundances corresponds roughly to

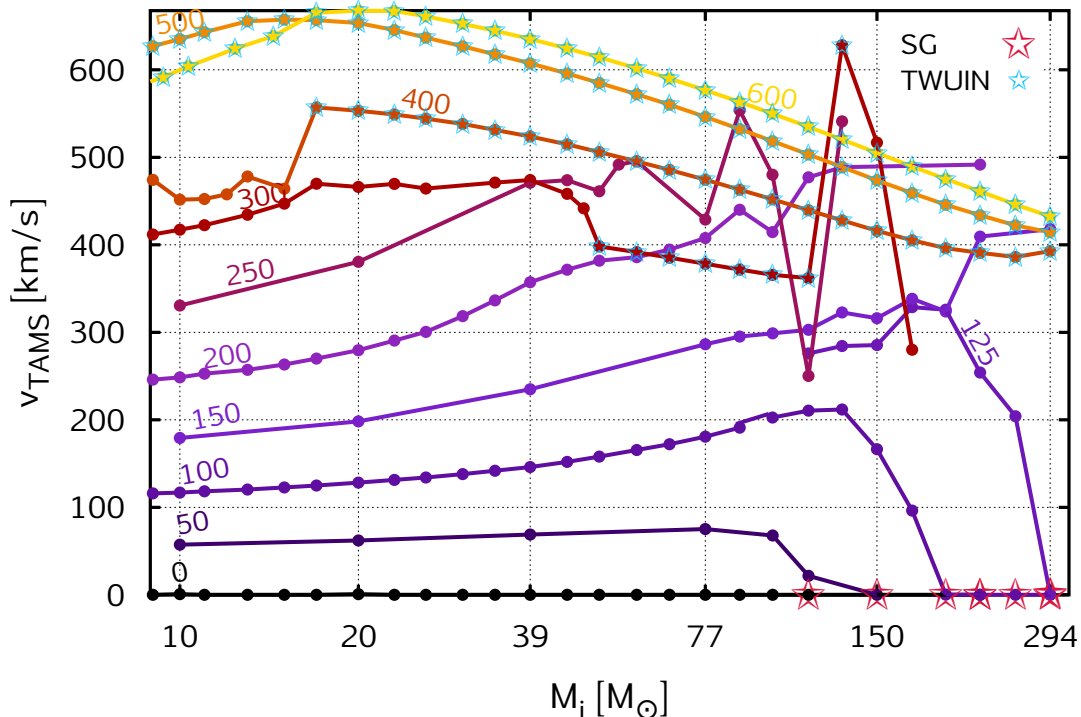


Fig. 14. Rotational velocity at the terminal age main-sequence (TAMS) as a function of initial mass. Every dot represents one evolutionary sequence. The colours refer to the initial rotational velocity; dots of model sequences with the same initial rotational velocity are connected and labelled (units in km s^{-1}). Only those sequences that have reached $Y_C=0.98$ have been plotted. (See also Fig. 4 which shows the rotational velocity at the ZAMS: here the same models are connected as in Fig. 4.) Core-hydrogen-burning cool supergiants (SG) are marked with large red stars, chemically-homogeneous TWUIN stars ($Y_S^{\text{TAMS}} > 0.7$) are marked with small blue stars.

$12 + \log(N/H) = 7$. Higher values in Fig. 15 imply a reduced hydrogen abundance.

Stars which undergo NE (represented by the tracks of 100 km s^{-1} in Fig. 15) are slow rotators. They mix some amount of nitrogen but the surface nitrogen abundance remains far from the CNO equilibrium abundance, indicating that rotational mixing is not very efficient. However, the higher the mass the larger the convective core and the more nitrogen appears at the surface.

The $294 M_{\odot} - 100 \text{ km s}^{-1}$ sequence becomes a core-hydrogen-burning red supergiant near the end of the main-sequence evolution. When the model approaches the red supergiant branch, the mass-loss becomes higher and deeper layers are uncovered. This causes a rapid increase of the N/H ratio at the stellar surface near the TAMS.

The intermediate rotators (represented by the tracks of $200 - 425 \text{ km s}^{-1}$ in Fig. 15) undergo TE (cf. Sect. 7). These models are mixed during the first part of their evolution, but then a chemical gradient develops between the core and the envelope which prevents further mixing. The fastest rotators (represented by the tracks of 450 km s^{-1} in Fig. 15) are chemically-homogeneously-evolving stars. They are, per definition, mixed throughout: every chemical change in the core is apparent at the surface as well.

Brott et al. (2011) computed the N/H ratio for stellar models with Galactic, LMC and SMC composition. The initial abundance of nitrogen in our models is much lower than that in the Brott models. However, our rotating models with NE and TE reach surface N/H ratios at the TAMS which can be higher than that in the adopted (initial) LMC and SMC compositions. Moreover, our models with CHE, even the less massive ones, have

surface N/H abundance ratios as high as 8.4. This value is higher than any value predicted by the Galactic, LMC and SMC models without CHE. The reason of this high N/H value in our models is the homogeneous mixing which transports all the hydrogen supply into the burning regions where it is destroyed. Consequently, observing surface N/H abundance ratios as high as 8.4 for a massive single star in a low-metallicity environment might imply that the star evolved chemically-homogeneously.

10. Photoionizing fluxes

Massive stars ionise their surroundings through their intense UV radiation (Schaerer et al. 1999b; Peters et al. 2010). To estimate the amount of ionizing radiation released by low-metallicity main-sequence stars, we discuss the ionizing fluxes of our stellar models based on the black body approximation (see also Table B.1).

In this section, we first present the ionizing fluxes and photon numbers calculated in the Lyman continuum (i.e. $\lambda < 912 \text{ \AA}$), in the He I continuum (i.e. $\lambda < 504 \text{ \AA}$) and in the He II continuum (i.e. $\lambda < 228 \text{ \AA}$). We then analyse the time evolution of the emission and the validity of the black body approximation. Finally, we discuss two aspects of our stellar models in terms of observational constraints: the total He II flux measured in I Zw 18 and the connection of our models to gamma-ray bursts and superluminous supernovae.

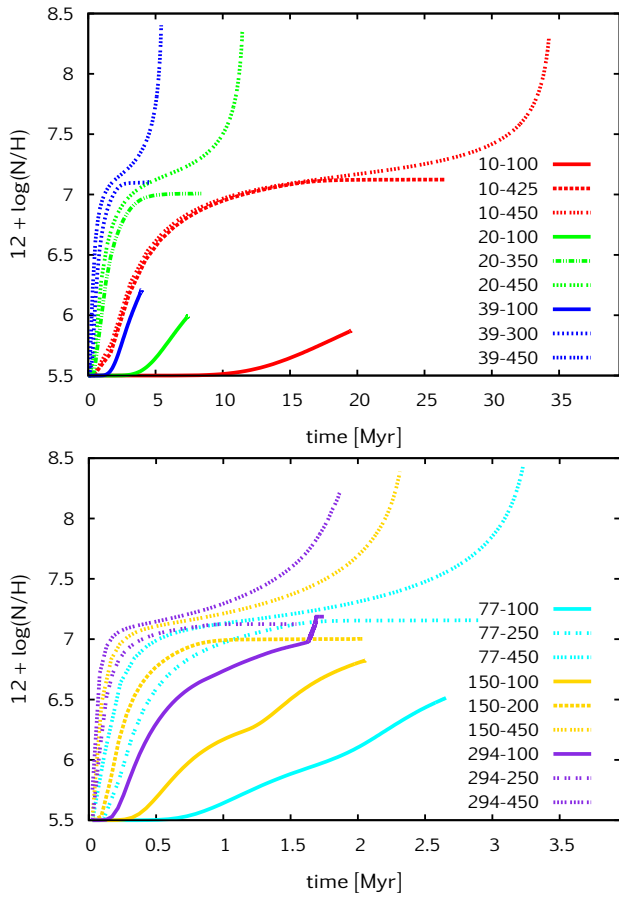


Fig. 15. Surface nitrogen abundance as a function of time for models with different initial masses and rotational velocity as indicated by the legend (units are $[M_{\odot}]$ - $[\text{km s}^{-1}]$). Models are chosen to represent all mass ranges and the three classes of evolution.

10.1. Time-integrated ionizing fluxes

The top panel in Fig. 16 shows the time-integrated energy, i.e. the total energy that is emitted by our models in the Lyman continuum during their core-hydrogen-burning lifetimes. The total emitted flux is an increasing function of the initial mass for the following reason. Although the main-sequence lifetime becomes shorter for a higher-mass model, both the luminosity and the surface temperature increase with the mass so much that the most massive model is able to radiate $\sim 10^3$ times more ionizing energy during its main-sequence lifetime than the lowest mass one.

According to Fig. 16, the emitted flux also depends on the initial rotation rate. On one hand, rotation increases the lifetime of a model (more fuel is mixed into the core due to rotational mixing), therefore increasing the time-integrated energy. Amongst the less massive, normally-evolving models, on the other hand, the lowest amount of ionizing energy is produced in the sequence with $9 M_{\odot}$ - 375 km s^{-1} (see Table 1), while the non-rotating model with the same mass produces somewhat more energy. This is because the rotating model has a larger radius than the non-rotating one due to the centrifugal acceleration, hence its luminosity and effective temperature are lower.

The fast rotators evolve chemically-homogeneously towards higher luminosities and higher surface temperatures. They generally produce ~ 5 - 10 times more ionizing energy than their normally-evolving counterparts of the same mass during the main-sequence lifetime.

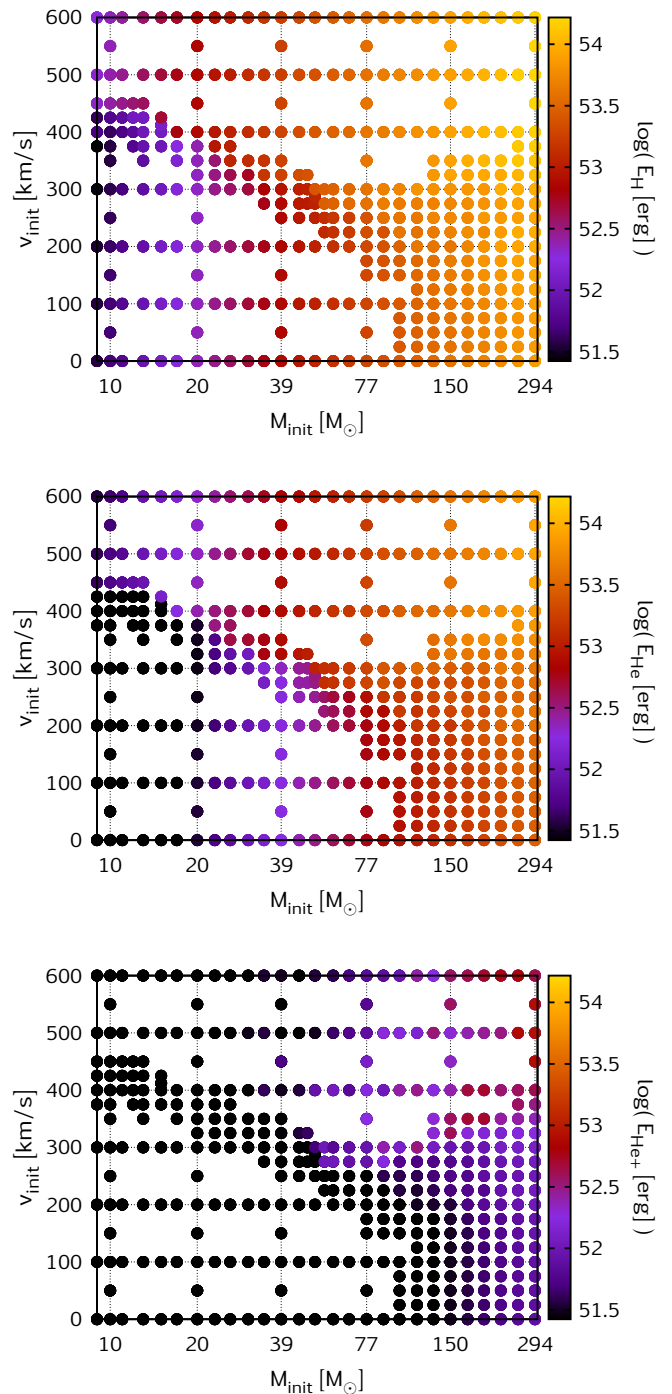


Fig. 16. *Top:* Ionizing energy emitted by our stellar sequences in the Lyman continuum during their main-sequence lifetime. Each evolutionary sequence of our grid is represented by one dot in this diagram and the total amount of energy emitted in the Lyman continuum (in ergs) is colour coded in a logarithmic scale. *Middle and bottom:* The same as the top figure but for the HeI and He II continua, respectively.

The time-integrated fluxes in the HeI and the He II continua are influenced by the mass and the rotation a similar way as those in the Lyman continuum. Consequently, the minimum and maximum time-integrated flux values correspond, respectively, to the lowest- and highest-mass models, at intermediate rotation rates. Table 1 gives the minimum and maximum values of the energy and photon numbers emitted by our models in all three continua.

Table 1. Minimum and maximum values of time-integrated energy (E) in ergs, time-integrated number (Q) of the ionizing photons and the time average value of the photon numbers per seconds for hydrogen (H), neutral helium (He) and singly ionised helium (He⁺) emitted during the main-sequence phase by our stellar evolutionary models (cf. Table B.1). Black body radiation is assumed. For comparison, the ionizing energy and photon numbers of the Pop III models of Yoon et al. (2012) are shown: these values are systematically higher than those of our corresponding models due to the higher effective temperatures of the metal-free models (see also Fig. 17).

	<i>this work</i>	E_{tot} [erg]	Q_{tot}	Q_{avr} [s ⁻¹]	<i>Pop III models</i>	$E_{\text{tot}}^{\text{PopIII}}$ [erg]	$Q_{\text{tot}}^{\text{PopIII}}$	$Q_{\text{avr}}^{\text{PopIII}}$ [s ⁻¹]
H	9 M _⊙ -375 km/s	2.65e51	1.00e62	1.21e+47	10 M _⊙ -0 v _k	1.53e52	4.95e62	6.41e+47
	100 M _⊙ -500 km/s	4.87e53	1.32e64	1.52e+50	100 M _⊙ -0.4 v _k	7.31e53	1.66e64	2.48e+50
	294 M _⊙ -500 km/s	1.49e54	3.89e64	6.75e+50	300 M _⊙ -0.4 v _k	1.96e54	4.55e64	7.19e+50
He	9 M _⊙ -375 km/s	9.22e49	2.11e60	2.55e+45	10 M _⊙ -0 v _k	3.36e51	7.10e61	9.20e+46
	100 M _⊙ -500 km/s	2.28e53	4.33e63	4.99e+49	100 M _⊙ -0.4 v _k	4.78e53	8.18e63	7.32e+49
	294 M _⊙ -500 km/s	7.58e53	1.42e64	2.46e+50	300 M _⊙ -0.4 v _k	1.24e54	2.15e64	2.92e+50
He ⁺	9 M _⊙ -375 km/s	1.81e45	1.98e55	2.39e+40	10 M _⊙ -0 v _k	1.20e49	1.27e59	1.65e+44
	100 M _⊙ -500 km/s	9.63e51	9.72e61	1.12e+48	100 M _⊙ -0.4 v _k	6.24e52	6.03e62	5.39e+48
	294 M _⊙ -500 km/s	3.93e52	3.95e62	6.85e+48	300 M _⊙ -0.4 v _k	1.41e53	1.37e63	1.86e+49

10.2. Time evolution of the emission

Fig. 17 shows the time evolution of the emission from both normal and chemically-homogeneous models with $M_{\text{ini}} = 100 M_{\odot}$. According to the plot, the emission from the model with NE decreases while that with CHE increases during their main-sequence evolution. This is expected since the model with CHE evolves towards higher luminosities and higher effective temperatures.

The average photon flux in the He II continuum is $2.00 \times 10^{47} \text{ s}^{-1}$ for the model with NE and $1.12 \times 10^{48} \text{ s}^{-1}$ for the model with CHE during their main-sequence phase. Considering somewhat lower masses, we find that the time-average He II photon flux from the chemically-homogeneous models is higher than that of the normally-evolving models by factors of 9, 12, and 15 at $77 M_{\odot}$, $51 M_{\odot}$ and $39 M_{\odot}$, respectively. The order of magnitude of these ratios implies that the contribution of the models with CHE to the total emitted He II ionizing flux of a low-metallicity galaxy may be significant.

Moreover, Fig. 17 demonstrates that towards the end of the main-sequence evolution, the ionizing fluxes of the chemically-homogeneous models can be an order of magnitude larger than those of normally-evolving models. In fact, comparing the peak ionizing He II fluxes from the chemically-homogeneous models to those of the normally-evolving models, we find ratios of 20, 27, 50, and 92 for stars of $100 M_{\odot}$, $77 M_{\odot}$, $51 M_{\odot}$ and $39 M_{\odot}$, respectively. We therefore expect that ionizing fluxes predicted by starburst models will drastically change when the TWUIN stars are taken into account.

For comparison, a corresponding metal-free model with CHE is plotted in Fig. 17. The ratio of the time-integrated fluxes of the two models with CHE for the main-sequence lifetime is $E(\gamma_{\text{He}^+})^{\text{IZW18}}/E(\gamma_{\text{He}^+})^{\text{PopIII}} = 0.15$ in the He II continuum. Table 1 compares the time-integrated ionizing energy and photon numbers in all three bands between our sequences and the Pop III sequences. The differences between the metal-poor and metal-free models derive from the latter evolving at systematically higher effective temperatures. Note, however, that the He II fluxes of the metal-free models may be overestimated by a factor of three (see below).

10.3. Validity of the approximations

At the considered metallicity, the mass-loss of massive stars is generally sufficiently weak to make the wind transparent in the continuum. As mentioned in Sect. 6, only our most massive chemically-homogeneously-evolving models are expected to de-

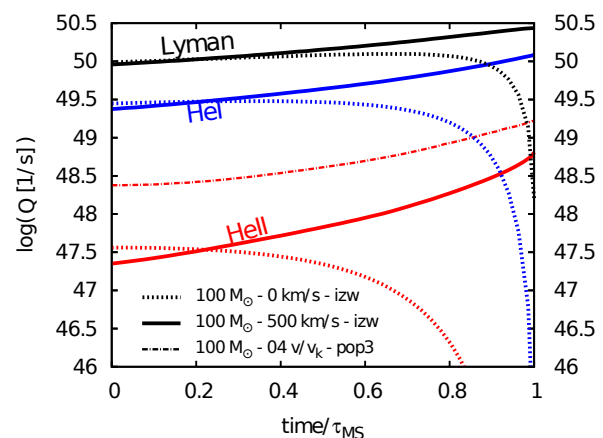


Fig. 17. Time evolution of the number of the ionizing photons for models with an initial mass of $100 M_{\odot}$. Photons emitted in the Lyman, He I and He II continua by a normally-evolving model (without rotation) and a chemically-homogeneously-evolving model (with an initial rotational velocity of 500 km s^{-1}) from our grid are plotted. For comparison, the number of photons emitted in the He II continuum by a chemically-homogeneously-evolving Pop III model from Yoon et al. (2012) with similar initial mass and initial rotational velocity (in units of the critical rotation, which refers to $v_{\text{ini}} \sim 520 \text{ km s}^{-1}$) is plotted by the dotted-dashed line. Note that the He II flux of the Pop III model may, however, be overestimated by a factor of three (see text).

velop winds with a continuum optical depth of order unity (cf., Fig. 8).

Kudritzki (2002) investigated the dependence of the ionizing photon fluxes of low-metallicity massive main-sequence stars on the mass-loss rate. He found the ionizing fluxes in general to be reduced at the highest considered metallicities due to the correspondingly stronger stellar winds. However, below a threshold metallicity, Kudritzki found that the fluxes are not affected by the winds anymore as they become too weak. While in the quoted work, the threshold metallicity is close to the one used in our models, the mass-loss rates adopted by Kudritzki are significantly larger than what is assumed in our work.

For He II ionizing photons, and only for those, Kudritzki found slightly more complex behaviour. At 50 kK and below, he found that the He II flux per cm^2 can increase for stronger winds. However, at the highest effective temperature, 60 kK, this effect was not seen anymore. In fact, the He II flux per cm^2 for the most luminous main-sequence stars at 60 kK is predicted by Kudritzki

to be approximately $10^{23.5} \text{ s}^{-1}$ in the case of both our metallicity and lower values. This value is very close to the black body prediction, as shown in Fig. 18.

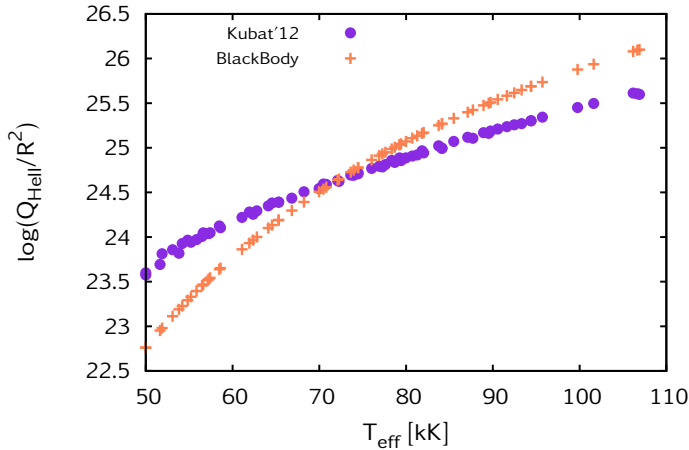


Fig. 18. Ionizing flux (normalised to one square centimetre of stellar surface) in the He II continuum provided by Kubát (2012) based on non-LTE spectra of metal-free massive stars and ionizing flux values using a black body approximation for the same collection of metal-free massive stars.

Kubát (2012) calculated the ionizing flux of metal-free massive hot stars based on simulated stellar atmospheres, for a large range of effective temperatures. In Fig. 18, we show the He II fluxes from Kubát (2012) for a large number of stellar models. As the models cover a wide mass range, Fig. 18 demonstrates that gravity effects, which cause the scatter in the plot, are very small.

When comparing Kubat’s results to the black body prediction, we note that while our metallicity is different from zero, Kudritzki (2002) finds that the metallicity dependence of the ionizing fluxes at the considered low-metallicity is generally quite weak, as discussed above. We find that in the temperature range of our most massive and hot stellar models, between $60 \text{ kK} < T_{\text{eff}} < 85 \text{ kK}$ (i.e. where they provide most of the ionizing radiation), Fig. 18 shows that the ionizing flux in the He II continuum calculated from the black body approximation matches that calculated from the stellar atmospheres to within $\lesssim 50\%$ (0.3 dex). Although this comparison is limited by the number of stellar spectra provided by Kubát (2012), as well as the difference between the composition of their metal-free models and our metal-poor models, it implies that the ionizing energy coming from our stellar evolutionary models using the black body approximation is indeed a good estimate for their He II ionizing fluxes.

We note that the Pop III models are significantly hotter than our low-metallicity models during core-hydrogen-burning. While this is the reason of their He II fluxes based on black body spectra being almost one order of magnitude larger than those of our models, Fig. 18 indicates that they may over-predict the true He II fluxes by a factor of three, whereas at the effective temperatures of our models this appears not to be the case. Thus, the step from the metallicity considered by our models to zero may increase the He II fluxes not by a factor of ten, as one might grasp from Fig. 17, but just by a factor of three.

In summary, the neglect of wind effects and the black body approximation both introduce uncertainties into the predicted ionizing fluxes. However, in the mass and metallicity regime which we consider here, the uncertainty of both effects appears to be within a factor of two. Conceivably, other uncertainties

may be larger. Indeed, the mass-loss rates we consider, in particular those for WR stars, may be more uncertain. E.g. Vink et al. (2011), found the mass-loss rate to jump to a steeper relation once the winds become optically thick. This effect, which is observationally confirmed for very luminous Of/WN and WNh stars in the LMC (Bestenlehner et al. 2014), is not implemented into our stellar models. On the other hand, Gräfener & Hamann (2008) and Muijres et al. (2012) predict the winds of the hottest helium-rich stars to become weaker or even to break down for increasing temperature. However, the investigated wind models are largely restricted to effective temperatures below 50 kK, whereas our TWUIN stars reach values of 80 kK, and higher.

Clearly, the ionizing fluxes which we provide are only approximate. Our work demonstrates the need for model atmosphere calculations for very hot stars (50...100 kK) at low (but finite) metallicity. At the same time, self-consistent mass-loss rate predictions are required, to place firmer constraints on the predicted ionizing fluxes.

10.4. He II ionizing flux of star-forming dwarf galaxies

As found in the comprehensive study by Shirazi & Brinchmann (2012), a large fraction of star-forming dwarf galaxies display strong He II emission, which is difficult to understand based on previously published evolutionary models of low-metallicity massive stars (cf. also Sect. 11). While WR stars are thought to have the potential to produce He II ionizing photons, most of the He II emitting dwarf galaxies below a certain metallicity do not show WR features in their spectra (Crowther & Hadfield 2006). We suggest that TWUIN stars (Sect. 6) could potentially resolve this discrepancy.

Kehrig et al. (2015) reported a He II ionizing photon flux, $Q(\text{He II})_{\text{obs}} \simeq 1.3 \times 10^{50} \text{ photons s}^{-1}$ measured by integral field spectroscopy for I Zw 18. They also suggested that WR stars are not responsible for most of this emission, and speculated about the presence of very massive, metal-free, chemically-homogeneously-evolving stars in this galaxy. Indeed, about 10-15 massive chemically-homogeneously-evolving Pop III stars with fluxes of $10^{49} \text{ photons s}^{-1}$ in the He II continuum could emit the amount of ionizing photons observed (Yoon et al. 2012). However, the gas in I Zw 18 is very metal-poor but not primordial, so the presence of actual Pop III stars in I Zw 18 may be debatable.

As we have shown above, our simulations of massive stars with the composition of I Zw 18 predict chemically-homogeneous evolution even for moderately fast rotating stars. Based on the empirical distribution of rotational velocities for O stars in the SMC by Mokiem et al. (2006), up to 20% of the very massive stars could undergo CHE. Possibly, at the ten-times smaller metallicity of I Zw 18, massive stars rotate even faster.

Figure 19 shows that the fraction of the stellar luminosity which is emitted as He II ionising photons above $\sim 20 M_{\odot}$ is weakly increasing with mass. This, together with the number of stars of given mass decreasing as $M^{-\alpha}$, with $\alpha \simeq 2.35$, and the mass-luminosity relation $L \sim M^{\beta}$ having an exponent of $\beta \simeq 2.5 \dots 1.5$ for stars in the mass range $20 M_{\odot} \dots 200 M_{\odot}$ (cf. Fig. 17 of Köhler et al. 2015), implies that all mass bins in the considered mass range provide similar contributions to the total He II flux of a stellar generation. Integration over a Salpeter initial mass function (IMF; Salpeter 1955; Kroupa 2001) from $0.5 M_{\odot}$ to $500 M_{\odot}$ and assuming a constant star-formation rate of $0.1 M_{\odot}$ (Lebouteiller et al. 2013) giving $300\,000 M_{\odot}$ of stars within 3 Myr results in a time-averaged He II flux of $1.6 \times 10^{50} \text{ s}^{-1}$ when 20% of the stars are assumed to undergo chemically-

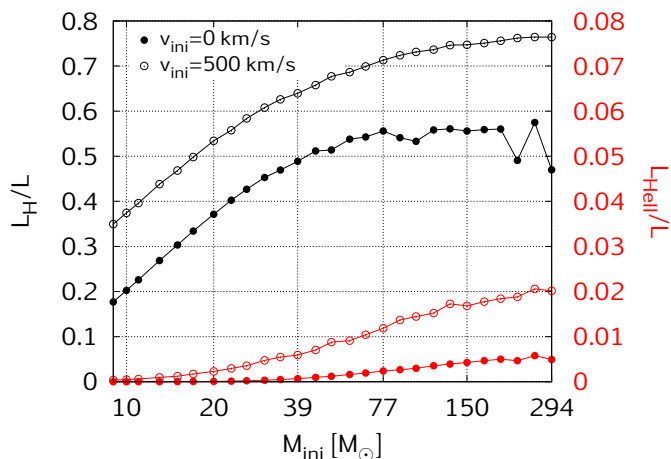


Fig. 19. Time-averaged luminosity in hydrogen and helium II ionizing photons, relative to the time-averaged total stellar luminosity of our models without rotation and with $v_{\text{ini}} = 500$ km/s, as function of the initial stellar mass.

homogeneous evolution. While this simple estimate can not replace proper population synthesis calculations, it indicates that TWUIN stars of finite metallicity may indeed explain the He II flux found for I Zw 18, especially given the fact that the maximum He II fluxes are about five times higher than the time-averaged values.

As discussed in Sect. 6, TWUIN stars have optically-thin ($\tau \lesssim 3$) winds. Therefore, they do not contribute to the broad emission signatures that characterise galaxy spectra with WR stars, but they still emit sufficient radiation to explain the observed He II ionizing photon flux in I Zw 18. This may imply that chemically-homogeneous evolution, which leads to TWUIN stars in our calculations, is a phenomenon that is indeed happening in nature.

As a consequence of their high temperature and the lack of optically-thick winds, TWUIN stars are expected to radiate at ultraviolet wavelengths. This means that their optical brightness is quite faint, with bolometric corrections estimated from assuming a black body spectrum of the order of $5 \dots 6^{\text{mag}}$ for effective temperatures in the range $70 \dots 90$ kK. On the other hand, they may contribute significantly to the observed optical spectra (rest-frame UV) of high-redshift galaxies.

10.5. The connection to GRBs, superluminous supernovae and high- z galaxies

Our rapidly-rotating models become TWUIN stars due to quasi-chemically-homogeneous evolution, which was identified as a promising road toward long-duration gamma-ray bursts (GRBs) by Yoon & Langer (2005) and Woosley & Heger (2006). Indeed, our results are consistent with the study of Yoon et al. (2006), who found a very similar threshold rotational velocity for chemically-homogeneous evolution for stars below $60 M_{\odot}$ as the present work. While we shall present the post-main-sequence evolution of our models in a forthcoming paper, from our models we can expect a similar ratio of GRBs to supernovae (SNe) of the order of $1\% \dots 3\%$ as Yoon et al. (2006). This is consistent with the GRB/SN-ratio in the local Universe being significantly smaller (Podsiadlowski et al. 2004) due to the observed preference for GRBs to occur in low-metallicity dwarf galaxies (Langer & Norman 2006; Niino 2011). As a conse-

quence, we can consider large He II-emission in low-metallicity star-forming dwarf galaxies (Sect. 10.4) as a signpost for upcoming GRBs in the same objects.

Similar to GRBs, the recently discovered hydrogen-poor superluminous supernovae (SLSNe; Quimby et al. 2013) also occur preferentially in low-metallicity dwarf galaxies (Leloudas et al. 2015). While pair-instability explosions (Kozyreva et al. 2014) and massive circumstellar interactions (Moriya et al. 2013; Mackey et al. 2014) have been proposed to explain some of these events, the magnetar model (Thompson et al. 2004; Woosley 2010) appears currently favoured (Inserra et al. 2013). Within the magnetar model, the enormous luminosities as observed in SLSNe are produced by heating due to the spin-down of a millisecond magnetar. Consequently, again similar to GRBs (Thompson et al. 2004), the progenitor stars need to produce extremely-rapidly-rotating iron cores. Within this scenario, TWUIN stars could also be considered as progenitors of SLSNe. While a quantitative connection requires the investigation of their post-main-sequence evolution, a qualitative connection of SLSNe with low-metallicity dwarf galaxies appears likely in this context.

Recently, Sobral et al. (2015) observed CR7, the most luminous Lyman- α emitter found at $z > 6$. They explained the high Lyman- α and He II emission with a combination of two populations of stars: a ‘normal’, red stellar population which dominates the mass, and a Pop III population which dominates the nebular emission. While comparing our theoretical predictions to the observational properties of CR7 falls outside of the scope of present work, we emphasize that our stellar models inherently predict two populations of stars: the normally, redwards-evolving ones with slow rotation, and the chemically-homogeneous, bluewards-evolving ones with fast rotation. This latter type, the TWUIN stars, emits intense ionizing radiation but show no WR features, similar to the supposed Pop III stars. Consequently, two chemically-distinct populations may not be required in CR7, because massive stellar evolution at low metallicity inherently produces the two types of stars observed.

11. Comparison to previous results

We discuss the similarities and differences between our stellar models and two grids of models at similar metallicities, one published by Meynet & Maeder (2002) (from now on, MM02) and Ekström et al. (2008), the other by Georgy et al. (2013) (from now on, G+13). Both grids have subsolar initial compositions. The grid from G+13 (with $Z=0.002$) consists of stellar sequences with initial masses between $9\text{--}120 M_{\odot}$ and initial rotational velocities of 0 and $0.4 v_k$ (v_k being the critical velocity at the ZAMS). The grid from MM02 (with $Z=0.00001$) consists of sequences with initial masses between $9\text{--}60 M_{\odot}$ and initial rotational velocities of 0 and 300 km s^{-1} .

11.1. HR diagram

Figure 20 shows the HR diagram of the three low-metallicity grids. The ZAMS regions of the grids move towards higher effective temperatures when the metallicity is lower. The ZAMS region of our grid extends to higher luminosities because it contains masses up to $294 M_{\odot}$.

The TAMS regions populated by the MM02 and G+13 grids are on the red side of the corresponding ZAMS regions, meaning that all the sequences evolve redwards. In the case of our grid, however, there are two separate

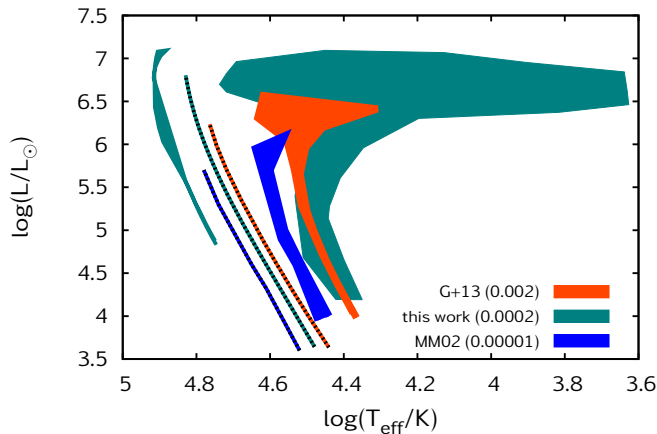


Fig. 20. HR diagram showing where the stellar sequences of three different grids begin the main-sequence evolution (ZAMS, marked with black dashed lines) and where they finish the main-sequence evolution (TAMS, shaded regions). *G+13*: Georgy et al. (2013); *MM02*: Meynet & Maeder (2002); the initial metallicity of the grids is also indicated by the legend.

TAMS areas corresponding to the normally-evolving and the chemically-homogeneously-evolving sequences. The prediction of chemically-homogeneously-evolving sequences at the TAMS is the first important difference between the previous results and our work.

Another important difference between the three grids derives from the value of the overshooting parameter utilised. The grid with $Z=0.00001$ was computed without taking overshooting into consideration (Meynet & Maeder 2002), while the grid with $Z=0.002$ included an overshooting parameter $\alpha_{\text{over}} = 0.1H_p$ (Georgy et al. 2013). Convective core overshooting gives larger cores, and has been shown to extend the main sequence to lower effective temperatures (Langer & Maeder 1995). This is why some of the sequences of our grid (with $\alpha_{\text{over}} = 0.335H_p$) finish their main-sequence evolution at lower T_{eff} than the corresponding sequences with $Z=0.002$.

The broadening of the TAMS of the normally-evolving sequences of our grid at the very high masses is related to the envelope inflation (Sect. 5, also see Fig. 5). Although the grid with $Z=0.002$ also shows a broadening around the highest masses (indeed, the non-rotating sequence of the $Z=0.002$ grid with initial mass of $120 M_{\odot}$ finishes the main-sequence evolution at $\log T_{\text{eff}} = 4.3$, while the corresponding rotating sequence finishes at $\log T_{\text{eff}} = 4.6$), this effect was linked to the efficiency of the stellar wind (Meynet & Maeder 2002). If the winds are strong and the mass lost during the main-sequence evolution is significant (but not strong enough to remove the hydrogen envelope), the mass fraction of the core increases with respect to the total mass. This increases the ratio of the core mass vs. total mass (similarly to the effect of overshooting) and the stellar models appear more red.

11.2. Mass-loss history and rotation

Fig. 21 compares the mass that is lost during the evolution of the stellar sequences in the three different grids as a function of initial mass and rotation. For the analysis of the mass-loss history of our models, we refer to Sect. 8. While the mass-loss rate prescriptions used by MM02 and G+13 are not exactly the same as ours, they nevertheless result in mass-loss rates comparable

to those of the prescriptions used here. This is apparent from Fig. 21. The mass that is lost during the evolution of stars in the mass range of $9\text{--}120 M_{\odot}$ is between 0 and $14 M_{\odot}$ for models from all three grids, depending strongly on the initial mass.

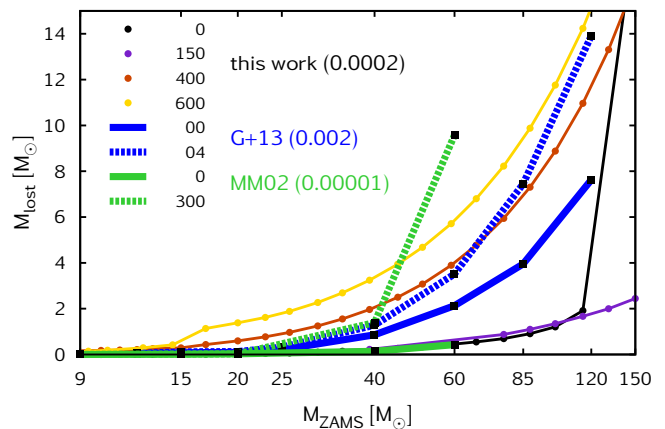


Fig. 21. Mass lost during the evolution of the stellar sequences in the three grids with different initial compositions. Sequences with four initial rotational rates of our grid, as indicated by the legend with units in km s^{-1} , are shown by connected dots. Sequences of the $Z=0.002$ grid (Georgy et al. 2013) and the $Z=0.00001$ grid (Meynet & Maeder 2002) are shown by black rectangles connected with lines as indicated by the legend with units in v_k and km s^{-1} , respectively. Note that the M_{lost} values of the $Z=0.00001$ grids correspond to the end of the helium-burning phase and are, therefore, an overestimate of the mass lost during the main sequence. The M_{lost} values of the $Z=0.002$ and I Zw 18 grids correspond to the end of the main sequence.

The non-rotating $Z=0.002$ sequences lose more mass during the main-sequence lifetime as our non-rotating sequences due to the metallicity dependence of the mass-loss rates. The non-rotating $Z=0.00001$ sequences end up having similar mass at the end of the helium-burning phase as our non-rotating sequences at the TAMS.

Our fast rotating sequences in Fig. 21 evolve chemically-homogeneously and undergo WR-type mass-loss during the last few Myr of the main-sequence evolution. Therefore, although their initial metallicity is lower, they might end up less massive at the TAMS than the rotating $Z=0.002$ sequences, that do not evolve chemically-homogeneously (Georgy et al. 2013). The rotating $Z=0.00001$ sequences of 40 and $60 M_{\odot}$ lose more mass than the rotating $Z=0.002$ sequences of the same masses; and the rotating $Z=0.00001$ sequence of $60 M_{\odot}$ loses even more mass than our chemically-homogeneously-evolving sequences of the same mass. However, this is because the M_{lost} values of the $Z=0.00001$ grid shown in Fig. 21 correspond to the end of helium burning and are, therefore, overestimating the mass lost during their main-sequence evolution.

In Sect. 9, we analysed the evolution of the rotational velocity in our models and noted that their behaviour is consistent with the findings of Meynet & Maeder (2002) and Ekström et al. (2008) for their $Z=0.00001$ models. These authors concluded that the massive ($\gtrsim 30 M_{\odot}$) stellar sequences increase their surface rotation due to the strong core-envelope coupling and the low mass-loss rates. Also, if the initial mass function at low metallicity extends up to high-mass stars, as often supposed, rotation is likely to be a major effect in the course of the evolution of massive stars, since many of them are likely to reach high velocities.

Our calculations supports these conclusions since our normally-evolving massive ($\geq 20 M_{\odot}$) sequences also increase their surface rotational velocity during the main sequence, as shown in Sect. 9. A quantitative comparison of our models with the $Z=0.00001$ models is less meaningful because of a limited overlap of the initial parameter space investigated.

12. Conclusions

We presented a grid of stellar evolutionary models in the mass range of 9-300 M_{\odot} with initial rotational velocities between 0-600 km s^{-1} , which is dense enough to be well suited for population-synthesis studies. The initial mass fraction of metals in our models is chosen to be 10% of that found in the SMC, which is probably appropriate for metal-poor blue compact dwarf galaxies such as I Zw 18. We found that our models evolve qualitatively differently compared to models of solar metallicity in several respects. We summarize the most important new results below.

- Massive main-sequence stars populate both sides of the ZAMS.** Apart from the normal (i.e. redwards) evolution of the slow rotating models, fast rotation induces chemically-homogeneous evolution in our low-metallicity massive stars. As these objects evolve bluewards from the zero-age main-sequence (cf. Sect. 4), we predict core-hydrogen-burning objects to be found on both sides of the ZAMS. This finding might be relevant to explain observations of high- z galaxies such as CR7 (Sobral et al. 2015) which apparently contains two different types of objects: a normal, red stellar population and a hot and luminous stellar population that dominates the ionizing radiation of the galaxy. As we have shown, low-metallicity massive stellar evolution inherently produces both type of objects.
- Core-hydrogen-burning cool supergiants.** We find the majority of our massive ($>80 M_{\odot}$) models evolve into cool supergiants while still burning hydrogen in the core, and spend up to 10% of their life time as such (cf. Sect. 5). This evolutionary outcome is a consequence of the low mass-loss rate and the envelope inflation close to the Eddington limit (Sanyal et al. 2015). Although short lived and rare, they may provide an important contribution to the chemical evolution of their environments due to the large amount of nuclearely-processed material that is lost in their slow stellar wind.
- Transparent Wind Ultraviolet Intense (TWUIN) stars.** Our fast rotating stars, which may comprise 10...20% of all massive stars, evolve chemically homogeneously and bluewards in the HR diagram during core hydrogen burning (cf. Sect. 6). Due to their extremely high effective temperatures, and the expectation that their winds remain optically thin, we show that these TWUIN stars may have very high ionizing fluxes (cf. Sect. 10). E.g., their maximum He II ionizing photon flux is about 20 to 100 times larger than that of their non-rotating counterparts (cf. Sect. 10.4). We find that the measured He II flux of I Zw 18 (Kehrig et al. 2015) as well as the weakness or absence of Wolf-Rayet features in I Zw 18 and other low-metallicity dwarf galaxies (Shirazi & Brinchmann 2012) is compatible with a population of TWUIN stars in these objects.
- Increasing surface rotational velocity.** Consistent with previous models of low-metallicity massive stars (cf. Sect. 11), our calculations show that the normally evolving models increase their surface rotational velocity during the main-sequence lifetime due to strong core-envelope coupling and low mass-loss rates (cf. Sect. 9). Therefore, the rotational velocity distribution of core-hydrogen-burning massive stars to be observed in low-metallicity environments might be different to that in higher-metallicity environments.
- Connection to IGRBs and superluminous SNe.** It has been argued previously that chemically-homogeneous evolution is a promising path towards long-duration gamma-ray bursts (cf., Sect. 10.5). Their preference to occur in low-metallicity dwarf galaxies, together with the spectroscopic features of dwarf galaxies mentioned above, provides increasing evidence for chemically-homogeneous evolution indeed occurring at low metallicity. As superluminous supernovae may also require low metallicity and rapid rotation (see Sect. 10.5), chemically-homogeneous evolution may also be a factor in these dramatic final explosions and in the evolutionary path that leads to them.

Observations of massive stars in nearby compact dwarf galaxies, of massive-star populations in high-redshift galaxies, or even of stellar explosions in the far Universe can provide promising avenues to expand and improve our knowledge of massive star evolution at low metallicity. Here we provided a complementary view from theoretical models considering the main-sequence evolution, while the post-main-sequence phase will be presented in a forthcoming work. It will thus require further efforts on both sides, observational and theoretical, before we are able to understand low-metallicity massive stars as well as those in our Milky Way, and thus obtain a deeper understanding of metal-poor environments in the Universe.

Acknowledgements. The authors thank Jorick Vink and the VLT FLAMES Tarantula consortium for their comments. S.-C. Y was supported by the Basic Science Research (2013R1A1A2061842) program through the National Research Foundation of Korea (NRF). We thank the referee, Dr Sally Heap, for her constructive report on our draft.

References

- Abel, T., Bryan, G., & Norman, M. 2002, *Science*, 295, 93
Aloisi, A., Savaglio, S., Heckman, T. M., et al. 2003, *ApJ*, 595, 760
Aloisi, A., Tosi, M., & Greggio, L. 1999, *ApJ*, 118, 302
Aloisi, A. et al. 2007, *ApJ*, 667, L151
Annibali, F., Cignoni, M., Tosi, M., et al. 2013, *AJ*, 146, 144
Arcavi, I., Gal-Yam, A., Kasliwal, M. M., et al. 2010, *ApJ*, 721, 777
Asplund, M. et al. 2009, *ARA&A*, 47, 481
Bastian, N. et al. 2013, *MNRAS*, 436, 2398
Beers, T. C. & Christlieb, N. 2005, *ARA&A*, 43, 531
Bestenlehner, J. M., Gräfener, G., Vink, J. S., et al. 2014, *A&A*, 570, A38
Bromm, V. & Larson, R. B. 2004, *ARA&A*, 42, 79
Brott, I., de Mink, S. E., Cantiello, M., et al. 2011, *A&A*, 530, A115
Böhm-Vitense, E. 1958, *ZAp*, 46, 108
Cantiello, M., Yoon, S.-C., Langer, N., & Livio, M. 2007, *A&A*, 465, L29
Caretta, 2010, *A&A*, 516, A55
Caretta, E. et al. 2005, *A&A*, 433, 597
Castro, N., Fossati, L., Langer, N., et al. 2014, *A&A*, 570, L13
Chabrier, G., Hennebelle, P., & Charlot, S. 2014, *ApJ*, 796, 75
Chiappini, C., Frischknecht, U., Meynet, G., et al. 2011, *Nature*, 472, 454
Chini, R., Hoffmeister, V. H., Nasserri, A., Stahl, O., & Zinnecker, H. 2012, *MNRAS*, 424, 1925
Ciardi, B., Ferrara, A., & White, S. D. M. 2003, *MNRAS*, 344, L7
Crowther, P. A. & Hadfield, L. J. 2006, *A&A*, 449, 711
Crowther, P. A., Schnurr, O., Hirschi, R., et al. 2010, *MNRAS*, 408, 731
Dabringhausen, J., Kroupa, P., & Baumgardt, H. 2009, *MNRAS*, 394, 1529
D'Antona, F. & Ventura, P. 2010, *Proceedings IAU Symposium*, No.268
de Jager, C., Nieuwenhuijzen, H., & van der Hucht, K. A. 1988, *A&AS*, 72, 259
de Mink, S. et al. 2009, *A&A*, 507, L1
de Mink, S. E., Langer, N., Izzard, R. G., Sana, H., & de Koter, A. 2013, *ApJ*, 764, 166
de Mink, S. E., Sana, H., Langer, N., Izzard, R. G., & Schneider, F. R. N. 2014, *ApJ*, 782, 7

- Decressin, T., Meynet, G., Charbonnel, C., Prantzos, N., & Ekström, S. 2007, *A&A*, 464, 1029
- Denissenkov, P. & Hartwick, F. 2014, *MNRAS*, 437
- Dufton, P. L., Langer, N., Dunstall, P. R., et al. 2013, *A&A*, 550, A109
- Ekström, S., Georgy, C., Meynet, G., Maeder, A., & Granada, A. 2011, in *IAU Symposium, Vol. 272, IAU Symposium*, ed. C. Neiner, G. Wade, G. Meynet, & G. Peters, 62–72
- Ekström, S., Meynet, G., Maeder, A., & Barblan, F. 2008, *A&A*, 478, 467
- Eldridge, J. J., Izzard, R. G., & Tout, C. A. 2008, *MNRAS*, 384, 1109
- Eldridge, J. J., Langer, N., & Tout, C. A. 2011, *MNRAS*, 414, 3501
- Eldridge, J. J. & Stanway, E. R. 2012, *MNRAS*, 419, 479
- Espinosa Lara, F. & Rieutord, M. 2013, *A&A*, 552, A35
- Frebel, A., Aoki, W., Christlieb, N., et al. 2005, *Nature*, 434, 871
- Georgy, C., Ekström, S., Eggenberger, P., et al. 2013, *A&A*, 558, A103
- Georgy, C., Ekström, S., Meynet, G., et al. 2012, *A&A*, 542, A29
- Georgy, C., Meynet, G., Walder, R., Folini, D., & Maeder, A. 2009, *A&A*, 502, 611
- Gräfenor, G. & Hamann, W.-R. 2008, *A&A*, 482, 945
- Gräfenor, G., Vink, J. S., de Koter, A., & Langer, N. 2011, *A&A*, 535, A56
- Graham, J. F. & Fruchter, A. S. 2013, *ApJ*, 774, 119
- Gratton, R. G., Bonifacio, P., Bragaglia, A., et al. 2001, *A&A*, 369, 87
- Greif, T. H., Glover, S. C. O., Bromm, V., & Klessen, R. S. 2010, *ApJ*, 716, 510
- Grevesse, N., Noels, A., & Sauval, A. J. 1996, in *Astronomical Society of the Pacific Conference Series, Vol. 99, Cosmic Abundances*, ed. S. S. Holt & G. Sonneborn, 117
- Groenewegen, M. A. T., Sloan, G. C., Soszyński, I., & Petersen, E. A. 2009, *A&A*, 506, 1277
- Hamann, W.-R., Koesterke, L., & Wesołowski, U. 1995, *A&A*, 299, 151
- Heap, S., Bouret, J.-C., & Hubeny, I. 2015, *ArXiv e-print 1504.02742*
- Heger, A. & Langer, N. 2000, *ApJ*, 544, 1016
- Heger, A., Langer, N., & Woosley, S. E. 2000, *ApJ*, 528, 368
- Heger, A. & Woosley, S. E. 2010, *ApJ*, 724, 341
- Heger, A., Woosley, S. E., & Spruit, H. C. 2005, *ApJ*, 626, 350
- Hirschi, R., Meynet, G., & Maeder, A. 2005, *A&A*, 443, 581
- Horváth, I., Hakkila, J., & Bagoly, Z. 2014, *A&A*, 561, L12
- Hosokawa, T., Yoshida, N., Omukai, K., & Yorke, H. W. 2012, *ApJ*, 760, L37
- Huang, W., Gies, D. R., & McSwain, M. V. 2010, *ApJ*, 722, 605
- Hunter, D. & Thronson, H. 1995, *ApJ*, 452, 238
- Hunter, I., Dufton, P. L., Smartt, S. J., et al. 2007, *A&A*, 466, 277
- Hunter, I., Lennon, D. J., Dufton, P. L., et al. 2008, *A&A*, 479, 541
- Iglesias, C. A. & Rogers, F. J. 1996, *ApJ*, 464, 943
- Inserra, C., Smartt, S. J., Jerkstrand, A., et al. 2013, *ApJ*, 770, 128
- Izotov, Y., Papaderos, P., Thuan, T., et al. 1999, unpublished
- Izotov, Y. & Thuan, T. 2002, *ApJ*, 567
- Izotov, Y. & Thuan, T. 2004, *ApJ*, 616, 768
- Kehrig, C., Pérez-Montero, E., Vílchez, J. M., et al. 2013, *MNRAS*, 432, 2731
- Kehrig, C., Vílchez, J. M., Pérez-Montero, E., et al. 2015, *ApJ*, 801, L28
- Keller, S. C., Bessell, M. S., Frebel, A., et al. 2014, *Nature*, 506, 463
- Köhler, K., Langer, N., de Koter, A., et al. 2015, *A&A*, 573, A71
- Kozyreva, A., Blinnikov, S., Langer, N., & Yoon, S.-C. 2014, *A&A*, 565, A70
- Kroupa, P. 2001, *MNRAS*, 322, 231
- Krtićka, J., Owocki, S. P., & Meynet, G. 2011, *A&A*, 527, A84
- Kubát, J. 2012, *ApJS*, 203, 20
- Kudritzki, R. P. 2002, *ApJ*, 577, 389
- Kudritzki, R. P., Pauldrach, A., & Puls, J. 1987, *A&A*, 173, 293
- Langer, N. 1989, *A&A*, 210, 93
- Langer, N. 1991, *A&A*, 252, 669
- Langer, N. 1997, *Luminous Blue Variables: Massive Stars in Transition*. ASP Conference Series. Ed. A. Nota, H. Lamers., 120, 83
- Langer, N. 1998, *A&A*, 329, 551
- Langer, N. 2012, *ARA&A*, 50, 107
- Langer, N., Fricke, K. J., & Sugimoto, D. 1983, *A&A*, 126, 207
- Langer, N. & Maeder, A. 1995, *A&A*, 295, 685
- Langer, N. & Norman, C. A. 2006, *ApJ*, 638, L63
- Langer, N., Norman, C. A., de Koter, A., et al. 2007, *A&A*, 475, L19
- Lebouteiller, V., Heap, S., Hubeny, I., & Kunth, D. 2013, *A&A*, 553, A16
- Lecavelier des Etangs, A., Désert, J.-M., Kunth, D., et al. 2004, *A&A*, 413, 131
- Lee, Y. S., Suda, T., Beers, T. C., & Stancliffe, R. J. 2014, *ApJ*, 788, 131
- Legrand, F., Kunth, D., Roy, J.-R., Mas-Hesse, J. M., & Walsh, J. R. 1997, *A&A*, 326, L17
- Leloudas, G., Schulze, S., Krühler, T., et al. 2015, *MNRAS*, 449, 917
- Levesque, E. M., Kewley, L. J., Berger, E., & Zahid, H. J. 2010, *AJ*, 140, 1557
- Longmore, S. N., Kruijssen, J. M. D., Bastian, N., et al. 2014, *Protostars and Planets VI*, 291
- Lunnan, R., Chornock, R., Berger, E., et al. 2013, *ApJ*, 771, 97
- MacFadyen, A. & Woosley, S. 1999, *ApJ*, 524, 262
- Mackey, J., Mohamed, S., Gvaramadze, V. V., et al. 2014, *Nature*, 512, 282
- Maeder, A. 1987, *A&A*, 178
- Maeder, A. & Meynet, G. 2000, *ARA&A*, 38, 143
- Marigo, P., Chiosi, C., & Kudritzki, R.-P. 2003, *A&A*, 399, 617
- Martins, F., Depagne, E., Russeil, D., & Mahy, L. 2013, *A&A*, 554, A23
- Mathews, G. J., Kajino, T., & Shima, T. 2005, *Phys. Rev. D*, 71
- Mauron, N. & Josselin, E. 2011, *A&A*, 526
- McEvoy, C. M., Dufton, P. L., Evans, C. J., et al. 2015, *A&A*, 575, A70
- Meynet, G. & Maeder, A. 2000, *A&A*, 361, 101
- Meynet, G. & Maeder, A. 2002, *A&A*, 390, 561
- Meynet, G. & Maeder, A. 2005, *A&A*, 429, 581
- Meynet, G. & Maeder, A. 2007, *A&A*, 464, L11
- Modjaz, M., Kewley, L., Bloom, J. S., et al. 2011, *ApJ*, 731, L4
- Mokiem, M. R., de Koter, A., Evans, C. J., et al. 2006, *A&A*, 456, 1131
- Mokiem, M. R., de Koter, A., Vink, J. S., et al. 2007, *A&A*, 473, 603
- Moriya, T. J., Blinnikov, S. I., Tominaga, N., et al. 2013, *MNRAS*, 428, 1020
- Moriya, T. J. & Langer, N. 2015, *A&A*, 573, A18
- Muijres, L. et al. 2012, *A&A*, 537
- Müller, P. & Vink, J. 2014, *A&A*, 564
- Nicholls, D. C., Dopita, M. A., Sutherland, R. S., et al. 2014, *ApJ*, 786, 155
- Nieuwenhuijzen, H. & de Jager, C. 1990, *A&A*, 231, 134
- Niino, Y. 2011, *MNRAS*, 417, 567
- Nugis, T. & Lamers, H. J. G. L. M. 2000, *A&A*, 360, 227
- Peimbert, M., Luridiana, V., & Peimbert, A. 2007, *ApJ*, 666, 636
- Penny, L. R. & Gies, D. R. 2009, *ApJ*, 700, 844
- Peters, T., Banerjee, R., Klessen, R. S., et al. 2010, *ApJ*, 711, 1017
- Podsiadlowski, P., Mazzali, P. A., Nomoto, K., Lazzati, D., & Cappellaro, E. 2004, *ApJ*, 607, L17
- Portegies Zwart, S. F., McMillan, S. L. W., & Gieles, M. 2010, *ARA&A*, 48, 431
- Puls, J., Vink, J. S., & Najaro, F. 2008, *A&A Rev.*, 16, 209
- Quimby, R. M., Kulkarni, S. R., Kasliwal, M. M., et al. 2011, *Nature*, 474, 487
- Quimby, R. M., Yuan, F., Akerlof, C., & Wheeler, J. C. 2013, *MNRAS*, 431, 912
- Ramírez-Agudelo, O. H., Simón-Díaz, S., Sana, H., et al. 2013, *A&A*, 560, A29
- Salpeter, E. 1955, *ApJ*, 121, 161
- Sana, H., de Mink, S. E., de Koter, A., et al. 2012, *Science*, 337, 444
- Sanders, N. E., Soderberg, A. M., Valenti, S., et al. 2012, *ApJ*, 756, 184
- Sanyal, D. et al. 2015, *A&A*, accepted
- Schaerer, D., Contini, T., & Kunth, D. 1999a, *A&A*, 341, 399
- Schaerer, D., Contini, T., & Pindao, M. 1999b, *A&AS*, 136, 35
- Schneider, F. R. N., Izzard, R. G., de Mink, S. E., et al. 2014, *ApJ*, 780, 117
- Searle, L. & Sargent, W. 1972, *ApJ*, 173, 25
- Shirazi, M. & Brinchmann, J. 2012, *MNRAS*, 421, 1043
- Sobral, D., Matthee, J., Darvish, B., et al. 2015, *ArXiv e-prints 1504.01734*
- Sonnenfeld, A., Treu, T., Gavazzi, R., et al. 2012, *ApJ*, 752, 163
- Spruit, H. 2002, *A&A*, 381, 923
- Spruit, H. 2006, *arXiv:astro-ph/0607164*
- Suijs, M. P. L., Langer, N., Poelarends, A.-J., et al. 2008, *A&A*, 481, L87
- Thompson, T., Chang, P., & Quataert, E. 2004, *ApJ*, 611, 380
- Tolstoy, E., Hill, V., & Tosi, M. 2009, *ARA&A*, 47, 371
- Tramper, F., Sana, H., de Koter, A., & Kaper, L. 2011, *ApJ*, 741, L8
- Treu, T., Auger, M. W., Koopmans, L. V. E., et al. 2010, *ApJ*, 709, 1195
- Vaduvescu, O., McCall, M. L., & Richer, M. G. 2007, *AJ*, 134, 604
- Vink, J., de Koter, A., & Lamers, H. 2000, *A&A*, 362, 295
- Vink, J., de Koter, A., & Lamers, H. 2001, *A&A*, 369, 574
- Vink, J. S., Brott, I., Gräfenor, G., et al. 2010, *A&A*, 512, L7
- Vink, J. S., Muijres, L. E., Anthonisse, B., et al. 2011, *A&A*, 531, A132
- Walborn, N. R., Morrell, N. I., Howarth, I. D., et al. 2004, *ApJ*, 608, 1028
- Weisz, D. R., Dolphin, A. E., Skillman, E. D., et al. 2014, *ApJ*, 789, 147
- Woosley, S. & Heger, A. 2006, *ApJ*, 637, 914
- Woosley, S. E. 2010, *ApJ*, 719, L204
- Yong, D., Grundahl, F., Lambert, D. L., Nissen, P. E., & Shetrone, M. D. 2003, *A&A*, 402, 985
- Yoon, S.-C. 2015, *PASA*, 32, 15
- Yoon, S.-C., Dierks, A., & Langer, N. 2012, *A&A*, 542, A113
- Yoon, S.-C. & Langer, N. 2005, *A&A*, 443, 643
- Yoon, S.-C., Langer, N., & Norman, C. 2006, *A&A*, 460, 199
- Yoshida, N., Oh, S. P., Kitayama, T., & Hernquist, L. 2007, *ApJ*, 663, 687
- Yusof, N., Hirschi, R., Meynet, G., et al. 2013, *MNRAS*, 433, 1114
- Zhao, Y., Gao, Y., & Gu, Q. 2013, *ApJ*, 764, 44

Appendix A: Key quantities of our model sequences (Online material)

Table A.1. Important characteristics of our models. M^i : initial mass. v_{rot}^i : initial rotational velocity. $v_{\text{rot}}^{Y_C=0.28}$: rotational velocity at the zero-age main-sequence (defined as $Y_C=0.28$). τ_{MS} : Main-sequence lifetime. M^f : mass at the end of the calculation. v_{rot}^f : rotational velocity at the end of the calculation. Y_C^f : central mass fraction of helium at the end of the calculation. Y_S^f : surface mass fraction of helium at the end of the calculation; bold face indicates if the last model is chemically-homogeneous (with $Y_S^f \geq 0.7$), i.e. a TWAIN star. $A(C)_S^f = \log[C/H]_S^f + 12$: surface abundance of carbon (^{12}C) at the end of the calculation. $A(N)_S^f = \log[N/H]_S^f + 12$: surface abundance of nitrogen (^{14}N) at the end of the calculation. $\log L^f/L_\odot$: luminosity at the end of the calculation. T_{eff}^f : effective temperature at the end of the calculation. R^f : radius at the end of the calculation; bold face indicates if the last model is a cool supergiant (with $T_{\text{eff}}^f < 12$ kK). Type: evolutionary class as defined in Sect. 3.2.

M^i [M_\odot]	v_{rot}^i [km s^{-1}]	$v_{\text{rot}}^{Y_C=0.28}$ [km s^{-1}]	τ_{MS} [Myr]	M^f [M_\odot]	v_{rot}^f [km s^{-1}]	Y_C^f	Y_S^f	$A(C)_S^f$	$A(N)_S^f$	$\log L^f/L_\odot$	T_{eff}^f [K]	R^f [R_\odot]	Type
9	0	0	23.1	9.0	0	0.98	0.25	6.37	5.50	4.14	23828	6.9	NE
9	100	136	23.3	9.0	116	0.98	0.25	6.30	5.87	4.15	23532	7.1	NE
9	200	276	23.8	9.0	246	0.98	0.25	5.83	6.46	4.14	22567	7.7	NE
9	300	435	24.8	9.0	412	0.98	0.25	5.28	6.70	4.14	20948	8.9	NE
9	375	572	26.3	8.9	440	0.98	0.26	5.03	6.85	4.14	20778	9.1	NE
9	400	618	32.7	8.8	474	0.98	0.40	5.17	7.13	4.30	24777	7.7	TE
9	425	663	31.4	8.8	459	0.98	0.35	5.13	7.10	4.24	23067	8.2	TE
9	450	709	41.4	8.9	615	0.98	0.95	6.68	8.29	4.89	56521	2.9	CHE
9	500	741	43.0	8.7	627	0.98	0.96	6.68	8.30	4.88	56142	2.9	CHE
9	600	656	46.3	8.3	581	0.98	0.95	6.63	8.27	4.83	55739	2.8	CHE
10	0	0	19.5	10.0	0	0.98	0.25	6.37	5.50	4.29	24729	7.6	NE
10	50	67	19.5	10.0	57	0.98	0.25	6.37	5.50	4.28	24699	7.6	NE
10	100	135	19.6	10.0	117	0.98	0.25	6.29	5.87	4.28	24478	7.7	NE
10	150	205	19.7	10.0	179	0.98	0.25	6.08	6.27	4.28	24100	7.9	NE
10	200	276	19.9	10.0	249	0.98	0.25	5.82	6.47	4.28	23465	8.4	NE
10	250	351	20.2	10.0	331	0.98	0.25	5.53	6.59	4.28	22530	9.0	NE
10	300	432	20.8	10.0	417	0.98	0.26	5.26	6.72	4.28	21782	9.7	NE
10	350	523	21.5	9.9	446	0.98	0.26	5.09	6.81	4.28	21562	9.9	NE
10	375	569	22.1	9.9	446	0.98	0.27	5.04	6.88	4.29	21679	9.9	NE
10	400	615	23.6	9.8	452	0.98	0.29	5.07	7.00	4.31	22412	9.5	TE
10	425	660	26.5	9.7	468	0.98	0.36	5.16	7.12	4.39	24442	8.8	TE
10	450	705	34.3	9.8	616	0.98	0.96	6.70	8.30	4.99	58222	3.1	CHE
10	500	758	35.3	9.7	635	0.98	0.96	6.72	8.31	4.98	57837	3.1	CHE
10	550	756	36.4	9.5	634	0.98	0.96	6.71	8.31	4.96	57545	3.0	CHE
10	600	668	37.8	9.2	592	0.98	0.95	6.67	8.28	4.93	57477	3.0	CHE
11	0	0	16.6	11.0	0	0.98	0.25	6.37	5.50	4.40	25630	8.0	NE
11	100	135	16.9	11.0	118	0.98	0.25	6.29	5.89	4.41	25237	8.4	NE
11	200	275	17.2	11.0	253	0.98	0.25	5.80	6.48	4.41	24141	9.2	NE
11	300	430	17.8	11.0	422	0.98	0.25	5.26	6.70	4.40	22441	10.5	NE
11	400	612	19.8	10.8	452	0.98	0.28	5.06	6.97	4.42	22769	10.4	NE
11	425	657	22.4	10.7	471	0.98	0.36	5.17	7.12	4.50	25058	9.5	TE
11	450	702	28.9	10.8	618	0.98	0.96	6.73	8.31	5.08	59735	3.2	CHE
11	500	782	29.7	10.7	643	0.98	0.96	6.74	8.33	5.06	59304	3.2	CHE
11	600	683	31.9	10.2	604	0.98	0.96	6.70	8.30	5.02	58920	3.1	CHE
12	375	564	16.4	11.9	452	0.98	0.26	5.04	6.87	4.51	22919	11.5	NE
12	400	609	17.5	11.8	458	0.98	0.29	5.08	7.00	4.54	23654	11.1	TE
12	425	655	20.4	11.7	492	0.98	0.41	5.24	7.17	4.67	27710	9.4	TE
12	450	700	24.9	11.7	619	0.98	0.96	6.75	8.32	5.15	61058	3.4	CHE
13	0	0	12.9	13.0	0	0.98	0.25	6.37	5.50	4.60	27032	9.2	NE
13	100	135	13.0	13.0	120	0.98	0.25	6.28	5.91	4.61	26677	9.4	NE
13	200	275	13.2	13.0	257	0.98	0.25	5.77	6.49	4.61	25521	10.3	NE
13	300	427	13.8	13.0	434	0.98	0.26	5.24	6.74	4.61	23595	12.0	NE
13	350	515	14.4	12.9	458	0.98	0.27	5.09	6.86	4.61	23562	12.2	NE
13	375	561	15.5	12.8	467	0.98	0.30	5.11	7.02	4.65	24715	11.5	TE
13	400	607	16.7	12.7	478	0.98	0.35	5.17	7.11	4.70	26226	10.9	TE
13	425	652	17.2	12.7	481	0.98	0.37	5.19	7.13	4.71	26664	10.7	TE
13	450	697	21.8	12.7	620	0.98	0.96	6.76	8.32	5.22	62218	3.5	CHE
13	500	785	22.5	12.6	656	0.98	0.96	6.77	8.34	5.21	61624	3.5	CHE
13	600	707	23.7	12.1	624	0.98	0.96	6.75	8.32	5.18	61446	3.4	CHE

Table A.1. Continued.

M^i [M_{\odot}]	v_{rot}^i [km s^{-1}]	$v_{\text{rot}}^{Y_c=0.28}$ [km s^{-1}]	τ_{MS} [Myr]	M^f [M_{\odot}]	v_{rot}^f [km s^{-1}]	Y_C^f	Y_S^f	$A(C)_S^f$	$A(N)_S^f$	$\log L^f/L_{\odot}$	T_{eff}^f [K]	R^f [R_{\odot}]	Type
15	0	0	10.6	15.0	0	0.98	0.25	6.37	5.50	4.77	28131	10.3	NE
15	100	135	10.6	15.0	123	0.98	0.25	6.27	5.95	4.78	27743	10.6	NE
15	200	274	10.8	15.0	263	0.98	0.25	5.75	6.51	4.77	26481	11.6	NE
15	300	425	11.2	15.0	447	0.98	0.25	5.22	6.73	4.77	24345	13.7	NE
15	375	557	11.8	14.8	459	0.98	0.26	5.04	6.87	4.78	24286	13.8	NE
15	400	602	12.4	14.7	464	0.98	0.29	5.09	7.00	4.80	25038	13.4	TE
15	412	624	13.0	14.7	472	0.98	0.32	5.14	7.07	4.83	26020	12.8	TE
15	425	647	17.1	14.6	593	0.98	0.96	6.77	8.32	5.34	64650	3.7	CHE
15	500	780	17.9	14.5	657	0.98	0.96	6.80	8.35	5.33	63645	3.8	CHE
15	600	731	18.7	14.0	639	0.98	0.96	6.79	8.34	5.30	63389	3.7	CHE
17	0	0	9.0	17.0	0	0.98	0.25	6.37	5.50	4.92	28983	11.4	NE
17	100	135	9.0	17.0	125	0.98	0.25	6.26	5.96	4.92	28565	11.8	NE
17	200	274	9.2	17.0	270	0.98	0.25	5.72	6.52	4.92	27180	13.0	NE
17	300	423	9.9	17.0	470	0.98	0.28	5.22	6.91	4.94	25683	15.0	NE
17	350	506	9.9	16.8	464	0.98	0.27	5.10	6.90	4.92	25154	15.3	NE
17	375	552	10.9	16.7	483	0.98	0.34	5.17	7.09	4.99	27400	13.8	TE
17	400	597	14.0	16.6	557	0.98	0.96	6.77	8.32	5.44	67156	3.9	CHE
17	500	776	14.8	16.4	657	0.98	0.96	6.82	8.36	5.43	65277	4.0	CHE
17	600	823	15.5	15.9	665	0.98	0.96	6.82	8.36	5.40	64787	4.0	CHE
20	0	0	7.4	20.0	0	0.98	0.25	6.37	5.50	5.09	29910	13.1	NE
20	50	67	7.4	20.0	62	0.98	0.25	6.37	5.51	5.09	29781	13.2	NE
20	100	135	7.4	20.0	128	0.98	0.25	6.24	5.99	5.09	29449	13.5	NE
20	150	203	7.5	20.0	198	0.98	0.25	5.98	6.33	5.09	28868	14.1	NE
20	200	273	7.5	20.0	280	0.98	0.25	5.69	6.54	5.09	27855	15.1	NE
20	250	345	7.7	20.0	381	0.98	0.25	5.42	6.70	5.09	26510	16.7	NE
20	300	420	8.0	19.9	466	0.98	0.27	5.22	6.87	5.10	25908	17.7	NE
20	325	459	8.1	19.8	467	0.98	0.28	5.17	6.93	5.11	26115	17.6	NE
20	350	501	8.4	19.7	472	0.98	0.30	5.15	7.01	5.12	26696	17.1	TE
20	375	545	8.7	19.6	477	0.98	0.32	5.16	7.06	5.14	27381	16.5	TE
20	400	592	11.2	19.4	553	0.98	0.96	6.80	8.33	5.57	69373	4.2	CHE
20	450	682	11.5	19.3	612	0.98	0.96	6.83	8.35	5.56	68199	4.3	CHE
20	500	771	11.7	19.1	653	0.98	0.96	6.84	8.37	5.55	67287	4.4	CHE
20	550	856	12.0	18.9	669	0.98	0.96	6.85	8.37	5.54	66930	4.4	CHE
20	600	868	12.3	18.6	668	0.98	0.96	6.84	8.37	5.53	66754	4.3	CHE
23	0	0	6.3	23.0	0	0.98	0.25	6.37	5.50	5.23	30469	14.9	NE
23	100	135	6.4	22.9	131	0.98	0.25	6.23	6.04	5.23	29959	15.4	NE
23	200	272	6.5	22.9	291	0.98	0.25	5.68	6.55	5.23	28133	17.4	NE
23	300	417	7.0	22.9	470	0.98	0.29	5.24	6.94	5.26	26796	19.8	NE
23	325	456	7.2	22.7	475	0.98	0.31	5.21	7.02	5.27	27436	19.2	TE
23	350	497	7.4	22.6	483	0.98	0.33	5.20	7.08	5.29	28400	18.3	TE
23	375	540	9.3	22.3	518	0.98	0.96	6.80	8.32	5.67	71639	4.5	CHE
23	400	585	9.4	22.2	549	0.98	0.96	6.82	8.34	5.67	71145	4.5	CHE
23	500	766	9.8	21.9	645	0.98	0.96	6.86	8.38	5.65	69139	4.7	CHE
23	600	886	10.2	21.4	667	0.98	0.96	6.86	8.38	5.63	68378	4.7	CHE
26	0	0	5.6	25.9	0	0.98	0.25	6.37	5.50	5.35	30787	16.7	NE
26	100	134	5.6	25.9	134	0.98	0.25	6.21	6.07	5.35	30282	17.2	NE
26	200	272	5.7	25.9	300	0.98	0.25	5.68	6.59	5.35	28339	19.7	NE
26	300	415	6.0	25.8	464	0.98	0.27	5.27	6.92	5.36	26501	22.8	NE
26	325	453	6.4	25.6	479	0.98	0.33	5.24	7.07	5.40	28350	20.9	TE
26	350	494	8.0	25.1	482	0.98	0.96	6.79	8.31	5.76	73474	4.7	CHE
26	375	535	8.0	25.1	514	0.98	0.96	6.82	8.34	5.76	73065	4.7	CHE
26	400	579	8.1	25.0	544	0.98	0.96	6.84	8.35	5.75	72608	4.8	CHE
26	500	761	8.4	24.7	637	0.98	0.96	6.88	8.39	5.74	70762	4.9	CHE
26	600	919	8.8	24.1	661	0.98	0.96	6.88	8.39	5.72	69941	5.0	CHE
30	0	0	4.9	29.9	0	0.98	0.25	6.37	5.50	5.48	31044	19.0	NE
30	100	134	4.9	29.9	138	0.98	0.25	6.20	6.14	5.48	30440	19.8	NE
30	200	271	5.0	29.9	318	0.98	0.25	5.71	6.63	5.48	28586	22.5	NE
30	300	413	5.1	29.8	0	0.92	0.28	5.35	6.95	5.47	29555	20.7	NE
30	325	451	5.5	29.5	0	0.95	0.33	5.29	7.08	5.52	29726	21.7	TE
30	350	490	6.8	28.9	478	0.98	0.96	6.82	8.33	5.86	74982	5.0	CHE

Table A.1. Continued.

M^i [M_{\odot}]	v_{rot}^i [km s^{-1}]	$v_{\text{rot}}^{Y_c=0.28}$ [km s^{-1}]	τ_{MS} [Myr]	M^f [M_{\odot}]	v_{rot}^f [km s^{-1}]	Y_C^f	Y_S^f	$A(C)_S^f$	$A(N)_S^f$	$\log L^f/L_{\odot}$	T_{eff}^f [K]	R^f [R_{\odot}]	Type
30	400	573	6.9	28.8	538	0.98	0.96	6.86	8.36	5.85	74157	5.1	CHE
30	500	756	7.2	28.4	627	0.98	0.96	6.89	8.40	5.84	72480	5.3	CHE
30	600	925	7.5	27.7	653	0.98	0.96	6.90	8.40	5.82	71725	5.3	CHE
34	0	0	4.4	33.9	0	0.98	0.25	6.37	5.50	5.59	30782	22.1	NE
34	100	134	4.4	33.8	142	0.98	0.25	6.21	6.18	5.59	30388	22.6	NE
34	200	270	4.5	33.8	337	0.98	0.26	5.75	6.65	5.59	28697	25.3	NE
34	275	375	4.7	33.7	454	0.98	0.27	5.49	6.90	5.60	26026	31.1	NE
34	300	412	5.0	33.4	471	0.98	0.33	5.39	7.06	5.64	28021	28.0	TE
34	325	449	6.0	32.7	443	0.98	0.96	6.81	8.31	5.94	76456	5.3	CHE
34	350	487	6.0	32.6	474	0.98	0.96	6.83	8.33	5.94	76148	5.4	CHE
34	400	569	6.1	32.4	531	0.98	0.96	6.88	8.38	5.93	75482	5.4	CHE
34	500	752	6.3	32.0	618	0.98	0.97	6.91	8.41	5.92	73890	5.6	CHE
34	600	923	6.5	31.3	645	0.98	0.97	6.92	8.41	5.90	73152	5.6	CHE
39	0	0	4.0	38.8	0	0.98	0.25	6.37	5.50	5.70	30706	25.2	NE
39	50	67	4.0	38.8	69	0.98	0.25	6.36	5.57	5.70	30522	25.5	NE
39	100	134	4.0	38.8	146	0.98	0.25	6.20	6.21	5.70	30328	25.8	NE
39	150	202	4.0	38.8	235	0.98	0.26	6.00	6.51	5.70	30505	25.5	NE
39	200	270	4.0	38.8	357	0.98	0.27	5.85	6.69	5.70	29362	27.5	NE
39	250	339	4.2	38.7	471	0.98	0.28	5.69	6.88	5.71	27145	32.5	NE
39	275	374	4.3	38.5	456	0.98	0.29	5.60	6.96	5.72	26238	35.2	NE
39	300	410	4.5	38.2	474	0.98	0.35	5.45	7.10	5.76	28461	31.3	TE
39	325	447	5.3	37.3	438	0.98	0.96	6.83	8.33	6.03	77693	5.7	CHE
39	350	485	5.3	37.2	467	0.98	0.96	6.86	8.36	6.03	77449	5.7	CHE
39	400	565	5.3	37.0	524	0.98	0.96	6.90	8.39	6.02	76733	5.8	CHE
39	450	654	5.4	36.8	572	0.98	0.97	6.92	8.41	6.02	75957	5.9	CHE
39	500	747	5.5	36.5	607	0.98	0.97	6.93	8.42	6.01	75294	5.9	CHE
39	550	835	5.6	36.2	628	0.98	0.97	6.93	8.42	6.00	74833	6.0	CHE
39	600	920	5.7	35.8	635	0.98	0.97	6.93	8.42	5.99	74585	6.0	CHE
45	0	0	3.6	44.7	0	0.98	0.25	6.37	5.50	5.82	30184	29.7	NE
45	100	134	3.6	44.7	152	0.98	0.25	6.22	6.23	5.82	30073	29.9	NE
45	200	269	3.7	44.7	372	0.98	0.28	5.95	6.76	5.82	30949	28.2	NE
45	250	338	3.8	44.5	474	0.98	0.29	5.79	6.93	5.83	27436	36.5	NE
45	275	373	3.9	44.2	454	0.98	0.31	5.67	7.02	5.85	26030	41.3	TE
45	300	408	4.0	43.9	458	0.98	0.34	5.55	7.09	5.87	26817	39.9	TE
45	325	445	4.6	42.8	432	0.98	0.96	6.85	8.34	6.12	78810	6.2	CHE
45	400	562	4.7	42.5	515	0.98	0.96	6.91	8.40	6.11	77936	6.2	CHE
45	500	742	4.8	41.9	596	0.98	0.97	6.94	8.43	6.10	76635	6.4	CHE
45	600	917	5.0	41.1	625	0.98	0.97	6.95	8.43	6.08	75951	6.4	CHE
48	275	372	3.6	47.1	440	0.98	0.28	5.79	6.94	5.88	24500	48.5	NE
48	300	408	3.8	46.8	442	0.98	0.32	5.61	7.06	5.91	25507	46.1	TE
48	325	444	4.4	45.6	429	0.98	0.96	6.86	8.35	6.16	79267	6.4	CHE
51	0	0	3.3	50.7	0	0.98	0.25	6.37	5.50	5.91	29530	34.5	NE
51	100	134	3.3	50.6	158	0.98	0.25	6.24	6.27	5.91	29664	34.3	NE
51	200	269	3.4	50.6	382	0.98	0.30	6.02	6.79	5.91	31894	29.6	NE
51	250	337	3.5	50.3	461	0.98	0.28	5.90	6.90	5.92	25906	45.4	NE
51	275	372	3.5	50.0	436	0.98	0.29	5.78	6.98	5.93	24334	52.1	NE
51	287	389	3.6	49.8	438	0.98	0.31	5.69	7.04	5.94	24579	51.9	TE
51	300	408	4.2	48.4	398	0.98	0.96	6.83	8.32	6.20	79816	6.6	CHE
51	400	558	4.3	47.9	506	0.98	0.97	6.93	8.40	6.19	78889	6.6	CHE
51	500	737	4.4	47.3	585	0.98	0.97	6.96	8.43	6.17	77682	6.8	CHE
51	600	916	4.5	46.3	614	0.98	0.97	6.96	8.44	6.16	77047	6.8	CHE
55	225	302	3.3	54.4	483	0.98	0.31	5.96	6.90	5.97	30200	35.3	NE
55	250	336	3.4	54.1	492	0.98	0.33	5.77	7.04	5.99	28647	40.2	TE
55	275	372	3.9	52.3	368	0.98	0.95	6.79	8.28	6.24	80266	6.9	CHE
55	300	407	3.9	52.1	395	0.98	0.96	6.84	8.33	6.24	80278	6.8	CHE
59	0	0	3.0	58.6	0	0.98	0.25	6.37	5.50	6.02	28123	43.0	NE
59	100	134	3.1	58.5	165	0.98	0.26	6.26	6.44	6.02	29493	39.1	NE
59	200	268	3.1	58.4	386	0.98	0.32	6.03	6.88	6.01	34396	28.7	NE
59	225	302	3.2	58.3	496	0.98	0.33	5.90	6.99	6.03	31047	35.7	TE
59	250	336	3.3	57.9	496	0.98	0.37	5.70	7.10	6.06	29585	40.8	TE

Table A.1. Continued.

M^i [M_{\odot}]	v_{rot}^i [km s^{-1}]	$v_{\text{rot}}^{Y_c=0.28}$ [km s^{-1}]	τ_{MS} [Myr]	M^f [M_{\odot}]	v_{rot}^f [km s^{-1}]	Y_c^f	Y_s^f	$A(C)_s^f$	$A(N)_s^f$	$\log L^f/L_{\odot}$	T_{eff}^f [K]	R^f [R_{\odot}]	Type
59	275	371	3.7	55.9	365	0.98	0.95	6.80	8.29	6.28	80647	7.1	CHE
59	300	406	3.8	55.7	392	0.98	0.96	6.85	8.33	6.28	80668	7.1	CHE
59	400	556	3.8	55.1	495	0.98	0.97	6.94	8.41	6.27	79851	7.2	CHE
59	500	729	3.9	54.3	572	0.98	0.97	6.97	8.44	6.26	78767	7.3	CHE
59	600	913	4.0	53.3	602	0.98	0.97	6.98	8.44	6.25	78197	7.3	CHE
67	0	0	2.8	66.4	0	0.98	0.25	6.37	5.50	6.10	26399	54.0	NE
67	100	133	2.9	66.4	172	0.98	0.26	6.26	6.50	6.10	28856	45.2	NE
67	200	268	2.9	66.2	395	0.98	0.33	6.02	6.93	6.10	35100	30.5	NE
67	225	301	2.9	66.1	485	0.98	0.34	5.92	7.00	6.11	32679	35.5	TE
67	250	336	2.8	66.1	0	0.88	0.34	5.76	7.06	6.10	33637	33.3	TE
67	275	371	3.4	63.2	360	0.98	0.95	6.81	8.29	6.36	81210	7.6	CHE
67	300	406	3.4	63.0	385	0.98	0.96	6.86	8.34	6.35	81300	7.6	CHE
67	400	554	3.5	62.2	486	0.98	0.97	6.94	8.41	6.34	80571	7.6	CHE
67	500	724	3.6	61.4	560	0.98	0.97	6.97	8.44	6.33	79582	7.7	CHE
67	600	912	3.7	60.2	590	0.98	0.97	6.98	8.45	6.32	79064	7.7	CHE
77	0	0	2.6	76.3	0	0.98	0.25	6.37	5.50	6.20	23781	74.1	NE
77	50	66	2.6	76.3	75	0.98	0.25	6.36	5.66	6.20	23988	72.8	NE
77	100	133	2.7	76.2	181	0.98	0.27	6.26	6.51	6.20	27828	54.0	NE
77	150	200	2.7	76.1	286	0.98	0.31	6.15	6.79	6.19	34005	36.1	NE
77	175	234	2.7	76.1	340	0.98	0.33	6.07	6.90	6.20	35802	32.6	NE
77	200	267	2.7	76.0	408	0.98	0.35	5.98	6.98	6.20	35007	34.3	TE
77	225	301	2.8	75.8	477	0.98	0.42	5.71	7.15	6.23	37425	31.1	TE
77	250	336	2.9	74.7	429	0.98	0.41	5.63	7.16	6.26	25397	70.2	TE
77	275	370	3.1	72.4	356	0.98	0.95	6.79	8.27	6.44	81554	8.3	CHE
77	300	406	3.2	72.0	378	0.98	0.96	6.86	8.33	6.43	81818	8.2	CHE
77	350	477	3.2	71.5	428	0.98	0.96	6.92	8.38	6.43	81630	8.2	CHE
77	400	553	3.2	71.0	474	0.98	0.97	6.95	8.41	6.42	81243	8.2	CHE
77	450	632	3.2	70.6	515	0.98	0.97	6.97	8.43	6.42	80796	8.3	CHE
77	500	718	3.3	70.1	546	0.98	0.97	6.98	8.44	6.41	80375	8.3	CHE
77	550	817	3.3	69.4	567	0.98	0.97	6.98	8.44	6.41	80052	8.3	CHE
77	600	911	3.3	68.8	577	0.98	0.97	6.99	8.45	6.40	79881	8.3	CHE
88	0	0	2.5	87.1	0	0.98	0.25	6.37	5.50	6.28	20440	110.7	NE
88	100	133	2.5	87.0	191	0.98	0.28	6.24	6.61	6.28	26865	64.0	NE
88	150	200	2.5	86.9	295	0.98	0.32	6.11	6.86	6.28	34514	38.7	NE
88	175	233	2.5	86.8	347	0.98	0.35	5.99	6.98	6.28	37094	33.7	TE
88	200	267	2.6	86.7	440	0.98	0.35	5.93	7.01	6.29	32741	43.4	TE
88	225	301	2.6	86.0	317	0.98	0.32	5.83	7.03	6.31	22543	93.3	TE
88	250	335	2.9	83.9	554	0.98	0.66	5.79	7.41	6.46	41748	32.5	TE
88	275	370	2.9	83.0	379	0.98	0.91	6.49	8.01	6.50	78227	9.7	CHE
88	300	405	2.9	81.8	372	0.98	0.96	6.85	8.32	6.51	82149	8.9	CHE
88	400	551	3.0	80.7	463	0.98	0.97	6.95	8.41	6.50	81754	8.8	CHE
88	500	714	3.0	79.5	532	0.98	0.97	6.98	8.44	6.49	81009	8.9	CHE
88	600	909	3.1	78.1	563	0.98	0.97	6.99	8.45	6.47	80547	8.9	CHE
100	0	0	2.4	98.8	0	0.98	0.25	6.37	5.50	6.36	15675	206.4	NE
100	25	33	2.4	98.7	23	0.98	0.25	6.37	5.50	6.36	15738	204.8	NE
100	50	66	2.4	98.7	68	0.98	0.25	6.35	5.93	6.36	17348	168.6	NE
100	75	100	2.4	98.8	127	0.98	0.26	6.29	6.42	6.36	20965	115.3	NE
100	100	133	2.4	98.8	203	0.98	0.28	6.22	6.66	6.36	24948	81.3	NE
100	150	200	2.4	98.6	299	0.98	0.34	6.08	6.91	6.36	35245	40.7	NE
100	175	233	2.4	98.6	356	0.98	0.36	6.00	6.98	6.36	36241	38.6	TE
100	200	267	2.5	98.4	415	0.98	0.42	5.76	7.14	6.39	39536	33.3	TE
100	225	301	2.6	98.0	516	0.98	0.63	5.78	7.37	6.47	49765	23.2	TE
100	250	335	2.7	94.8	480	0.98	0.57	5.70	7.31	6.51	32043	58.2	TE
100	275	370	2.7	94.9	594	0.98	0.70	5.85	7.47	6.53	44852	30.6	TE
100	300	404	2.7	92.5	366	0.98	0.96	6.84	8.31	6.57	82282	9.5	CHE
100	400	550	2.8	91.1	452	0.98	0.96	6.94	8.40	6.56	82117	9.5	CHE
100	500	710	2.8	89.8	519	0.98	0.97	6.98	8.43	6.55	81495	9.5	CHE
100	600	908	2.9	88.2	550	0.98	0.97	6.99	8.44	6.54	81072	9.5	CHE
115	0	0	2.2	113.1	0	0.98	0.25	6.37	5.50	6.45	5895	1608.2	NE
115	25	33	2.2	113.2	3	0.97	0.25	6.37	5.50	6.45	9558	610.9	NE

Table A.1. Continued.

M^i [M_{\odot}]	v_{rot}^i [km s^{-1}]	$v_{\text{rot}}^{Y_c=0.28}$ [km s^{-1}]	τ_{MS} [Myr]	M^f [M_{\odot}]	v_{rot}^f [km s^{-1}]	Y_C^f	Y_S^f	$A(C)_S^f$	$A(N)_S^f$	$\log L^f/L_{\odot}$	T_{eff}^f [K]	R^f [R_{\odot}]	Type
115	50	66	2.2	113.2	22	0.98	0.25	6.34	6.08	6.45	10433	513.9	NE
115	75	100	2.2	113.4	116	0.98	0.27	6.26	6.53	6.45	17553	181.3	NE
115	100	133	2.3	113.5	210	0.98	0.29	6.19	6.72	6.45	23877	97.9	NE
115	125	166	2.3	113.4	276	0.98	0.32	6.12	6.85	6.45	28875	66.8	NE
115	150	199	2.3	113.3	303	0.98	0.36	6.02	6.98	6.45	37264	40.1	TE
115	175	233	2.3	113.2	349	0.98	0.39	5.91	7.06	6.45	40269	34.6	TE
115	200	266	2.4	112.7	477	0.98	0.53	5.74	7.25	6.52	41447	35.2	TE
115	225	300	2.4	111.1	273	0.98	0.43	5.69	7.17	6.51	21811	125.9	TE
115	250	335	2.5	108.6	250	0.98	0.50	5.66	7.24	6.56	23061	119.7	TE
115	275	369	2.5	107.8	478	0.98	0.60	5.71	7.34	6.59	31296	66.9	TE
115	300	404	2.6	105.9	362	0.98	0.95	6.79	8.26	6.65	82013	10.5	CHE
115	400	548	2.6	104.0	440	0.98	0.96	6.94	8.39	6.64	82386	10.2	CHE
115	500	707	2.6	102.5	503	0.98	0.97	6.98	8.43	6.63	81889	10.3	CHE
115	600	903	2.7	100.7	535	0.98	0.97	6.99	8.44	6.62	81524	10.2	CHE
131	0	0	2.1	128.8	0	0.96	0.25	6.37	5.50	6.52	7083	1208.6	NE
131	25	33	2.1	128.6	0	0.96	0.25	6.37	5.51	6.52	6182	1587.7	NE
131	50	66	2.1	128.5	1	0.97	0.25	6.33	6.20	6.52	6234	1564.5	NE
131	75	99	2.1	128.7	46	0.98	0.27	6.24	6.59	6.52	11921	429.6	NE
131	100	133	2.2	129.1	212	0.98	0.30	6.17	6.77	6.52	23140	113.8	NE
131	125	166	2.2	129.1	284	0.98	0.33	6.09	6.89	6.52	29710	69.0	NE
131	150	199	2.2	129.0	323	0.98	0.36	6.00	6.99	6.52	34014	52.7	TE
131	175	233	2.2	128.9	405	0.98	0.37	5.89	7.06	6.53	32015	60.0	TE
131	200	266	2.2	128.4	489	0.98	0.43	5.74	7.15	6.55	31023	65.6	TE
131	225	300	2.3	126.9	393	0.98	0.46	5.69	7.20	6.58	24797	105.8	TE
131	250	334	2.3	127.9	541	0.98	0.60	5.74	7.34	6.60	48315	28.6	TE
131	275	369	2.3	123.4	410	0.98	0.56	5.68	7.30	6.64	26327	100.1	TE
131	300	403	2.4	123.4	628	0.98	0.81	6.10	7.67	6.69	57418	22.4	TE
131	325	439	2.4	119.1	372	0.98	0.96	6.84	8.30	6.71	82286	11.2	CHE
131	350	474	2.4	118.5	391	0.98	0.96	6.88	8.33	6.71	82474	11.1	CHE
131	400	547	2.4	117.7	428	0.98	0.96	6.93	8.38	6.70	82488	11.0	CHE
131	500	704	2.5	115.9	489	0.98	0.97	6.97	8.42	6.70	82125	11.0	CHE
131	600	894	2.5	113.9	520	0.98	0.97	6.99	8.43	6.68	81830	11.0	CHE
150	0	0	2.0	147.3	0	0.94	0.25	6.37	5.50	6.59	6786	1432.3	NE
150	25	33	2.0	147.3	0	0.94	0.25	6.37	5.51	6.59	6885	1391.6	NE
150	50	66	2.1	141.7	0	0.98	0.34	6.08	6.92	6.60	4284	3645.8	NE
150	75	99	2.0	146.8	1	0.96	0.27	6.23	6.62	6.60	6549	1548.5	NE
150	100	133	2.1	147.5	166	0.98	0.31	6.13	6.82	6.60	19157	181.6	NE
150	125	166	2.1	147.7	285	0.98	0.35	6.05	6.94	6.60	31383	67.6	TE
150	150	199	2.1	147.5	316	0.98	0.38	5.97	7.02	6.60	37642	47.0	TE
150	175	233	2.1	147.4	375	0.98	0.39	5.87	7.09	6.61	37177	48.5	TE
150	200	266	2.0	144.8	1	0.94	0.30	5.87	7.00	6.61	7568	1177.8	TE
150	225	300	2.1	144.8	347	0.94	0.43	5.70	7.17	6.64	22812	134.6	TE
150	250	334	2.1	147.2	501	0.92	0.56	5.71	7.30	6.65	50869	27.3	TE
150	275	369	2.2	140.6	22	0.98	0.52	5.65	7.26	6.69	15678	301.7	TE
150	300	403	2.2	139.6	517	0.98	0.66	5.80	7.41	6.73	34221	65.8	TE
150	325	438	2.3	135.7	368	0.98	0.95	6.78	8.25	6.78	81609	12.3	CHE
150	350	473	2.3	134.8	382	0.98	0.96	6.85	8.30	6.78	82187	12.1	CHE
150	400	546	2.3	133.7	416	0.98	0.96	6.91	8.36	6.77	82427	12.0	CHE
150	450	622	2.3	132.7	448	0.98	0.96	6.94	8.39	6.77	82354	11.9	CHE
150	500	701	2.3	131.7	474	0.98	0.97	6.96	8.41	6.76	82236	11.9	CHE
150	550	788	2.3	130.7	493	0.98	0.97	6.97	8.42	6.76	82090	11.9	CHE
150	600	886	2.4	129.5	505	0.98	0.97	6.98	8.43	6.75	82020	11.8	NE
172	0	0	1.9	168.9	0	0.92	0.25	6.37	5.50	6.66	7274	1354.1	NE
172	25	33	1.8	168.9	1	0.92	0.25	6.37	5.53	6.66	7445	1293.1	NE
172	50	66	1.9	168.6	1	0.93	0.26	6.30	6.37	6.67	7205	1384.3	NE
172	75	99	1.9	168.3	1	0.95	0.28	6.19	6.70	6.67	7307	1354.3	NE
172	100	133	2.0	168.5	96	0.98	0.31	6.10	6.87	6.68	15768	292.8	NE
172	125	166	2.0	169.3	329	0.98	0.35	6.01	6.98	6.68	25894	108.6	TE
172	150	199	2.0	169.0	338	0.98	0.38	5.93	7.04	6.68	34616	60.8	TE
172	175	232	2.0	168.9	358	0.93	0.41	5.84	7.11	6.68	41374	42.7	TE

Table A.1. Continued.

M^i [M_{\odot}]	v_{rot}^i [km s^{-1}]	$v_{\text{rot}}^{Y_c=0.28}$ [km s^{-1}]	τ_{MS} [Myr]	M^f [M_{\odot}]	v_{rot}^f [km s^{-1}]	Y_C^f	Y_S^f	$A(C)_S^f$	$A(N)_S^f$	$\log L^f/L_{\odot}$	T_{eff}^f [K]	R^f [R_{\odot}]	Type
172	200	266	1.8	169.6	958	0.82	0.45	5.74	7.18	6.71	31187	78.0	TE
172	225	300	2.0	168.3	834	0.93	0.53	5.72	7.26	6.74	32098	75.9	TE
172	250	334	2.0	162.7	1	0.96	0.43	5.66	7.17	6.73	9123	930.4	TE
172	275	368	2.1	161.1	1	0.96	0.48	5.63	7.22	6.75	9490	875.8	TE
172	300	403	2.1	160.2	280	0.98	0.58	5.70	7.32	6.77	22706	157.4	TE
172	325	438	2.2	158.8	473	0.98	0.87	6.32	7.85	6.83	70324	17.6	CHE
172	350	473	2.2	153.6	376	0.98	0.95	6.80	8.26	6.84	81424	13.3	CHE
172	400	545	2.2	152.2	405	0.98	0.96	6.89	8.34	6.84	82098	13.0	CHE
172	500	699	2.2	149.8	459	0.98	0.96	6.95	8.39	6.83	82152	12.9	CHE
172	600	880	2.2	147.3	490	0.98	0.97	6.98	8.42	6.82	82057	12.8	CHE
196	0	0	1.8	192.5	0	0.90	0.25	6.37	5.50	6.73	8145	1167.5	NE
196	25	33	1.7	192.2	0	0.90	0.25	6.37	5.59	6.73	7073	1549.0	NE
196	50	66	1.8	192.0	1	0.91	0.26	6.28	6.44	6.73	7209	1495.5	NE
196	75	99	1.8	191.5	1	0.93	0.28	6.18	6.72	6.74	7031	1580.2	NE
196	100	132	1.9	189.7	0	0.98	0.32	6.07	6.90	6.75	5028	3120.1	NE
196	125	166	1.9	192.7	326	0.98	0.36	6.00	6.99	6.75	25402	122.5	TE
196	150	199	2.0	191.5	324	0.98	0.42	5.90	7.10	6.78	22208	165.4	TE
196	175	232	2.0	191.7	492	0.98	0.46	5.80	7.17	6.78	35567	64.9	TE
196	200	266	2.0	187.3	10	0.94	0.50	5.75	7.22	6.81	11591	632.4	TE
196	225	300	1.8	187.5	7	0.91	0.35	5.73	7.09	6.76	10474	732.6	TE
196	250	334	1.9	192.4	1065	0.88	0.55	5.71	7.28	6.81	34641	70.4	TE
196	275	368	1.9	183.9	2	0.95	0.47	5.63	7.22	6.80	10579	753.0	TE
196	300	402	1.8	190.3	704	0.87	0.56	5.68	7.30	6.80	42242	46.9	TE
196	325	437	2.1	177.2	541	0.98	0.72	5.92	7.51	6.88	35732	71.9	TE
196	350	472	2.1	174.1	376	0.98	0.94	6.72	8.19	6.91	80027	14.8	CHE
196	400	544	2.1	172.1	396	0.98	0.96	6.85	8.30	6.90	81487	14.2	CHE
196	500	697	2.1	169.3	446	0.98	0.96	6.94	8.38	6.90	81875	14.0	CHE
196	600	875	2.1	166.5	475	0.98	0.97	6.97	8.41	6.89	81911	13.8	CHE
224	0	0	1.9	180.1	0	0.98	0.52	5.65	7.26	6.83	4969	3507.0	NE
224	25	33	1.7	219.6	0	0.88	0.25	6.36	5.69	6.80	7514	1484.9	NE
224	50	66	1.7	219.3	1	0.89	0.26	6.26	6.52	6.80	7304	1575.5	NE
224	75	99	1.7	218.8	1	0.91	0.28	6.14	6.78	6.81	7523	1493.3	NE
224	100	132	1.9	209.1	0	0.98	0.40	5.95	7.07	6.82	4408	4414.5	TE
224	125	165	1.9	219.7	254	0.98	0.36	5.94	7.03	6.82	23573	154.6	TE
224	150	199	1.9	219.9	409	0.98	0.40	5.86	7.09	6.82	29977	96.0	TE
224	175	232	1.9	219.6	388	0.98	0.43	5.80	7.14	6.83	38613	58.0	TE
224	200	266	1.9	218.1	492	0.98	0.54	5.78	7.26	6.87	33828	79.7	TE
224	225	299	1.7	220.8	1008	0.82	0.48	5.70	7.21	6.85	33941	77.4	TE
224	250	333	1.8	212.7	9	0.92	0.42	5.65	7.16	6.85	11326	689.5	TE
224	275	367	1.8	210.7	4	0.93	0.45	5.62	7.20	6.86	11978	625.8	TE
224	300	402	1.9	215.0	689	0.94	0.69	5.87	7.46	6.92	45510	46.4	TE
224	325	437	1.9	201.5	14	0.97	0.64	5.78	7.39	6.92	14095	484.2	TE
224	350	472	2.0	204.1	474	0.98	0.88	6.36	7.87	6.96	70120	20.6	CHE
224	400	543	2.0	195.3	391	0.98	0.95	6.79	8.25	6.97	80310	15.7	CHE
224	500	695	2.0	191.9	434	0.98	0.96	6.92	8.36	6.96	81305	15.2	CHE
224	600	869	2.0	188.7	461	0.98	0.96	6.97	8.40	6.95	81583	15.0	CHE
257	0	0	1.6	252.4	0	0.86	0.25	6.37	5.50	6.87	10046	899.2	NE
257	25	33	1.6	252.0	0	0.86	0.25	6.36	5.78	6.87	8211	1346.8	NE
257	50	66	1.6	251.8	5	0.87	0.26	6.24	6.57	6.87	10011	908.2	NE
257	75	99	1.6	250.9	1	0.89	0.28	6.11	6.82	6.88	8063	1408.4	NE
257	100	132	1.8	227.1	0	0.98	0.49	5.87	7.19	6.90	4394	4870.2	TE
257	125	165	1.8	251.5	204	0.98	0.37	5.86	7.07	6.90	22265	188.8	TE
257	150	199	1.8	252.2	427	0.97	0.41	5.80	7.12	6.90	27530	124.2	TE
257	175	232	1.8	251.7	422	0.98	0.44	5.76	7.16	6.90	34517	79.4	TE
257	200	266	1.6	253.0	1018	0.85	0.46	5.73	7.19	6.93	30229	106.0	TE
257	225	299	1.9	249.4	557	0.98	0.57	5.77	7.30	6.95	36897	73.0	TE
257	250	333	1.7	243.6	73	0.89	0.39	5.65	7.14	6.91	13346	533.1	TE
257	275	367	1.7	245.5	13	0.92	0.44	5.61	7.19	6.93	10810	829.3	TE
257	300	401	1.8	235.3	214	0.92	0.58	5.72	7.32	6.97	17213	342.4	TE
257	325	436	1.9	228.7	114	0.96	0.65	5.81	7.41	6.99	20464	249.4	TE

Table A.1. Continued.

M^i [M_{\odot}]	v_{rot}^i [km s^{-1}]	$v_{\text{rot}}^{Y_c=0.28}$ [km s^{-1}]	τ_{MS} [Myr]	M^f [M_{\odot}]	v_{rot}^f [km s^{-1}]	Y_C^f	Y_S^f	$A(C)_S^f$	$A(N)_S^f$	$\log L^f/L_{\odot}$	T_{eff}^f [K]	R^f [R_{\odot}]	Type
257	350	471	1.9	228.4	361	0.98	0.82	6.16	7.70	7.03	56975	33.5	TE
257	375	506	1.9	223.7	380	0.98	0.94	6.70	8.17	7.03	77915	18.1	CHE
257	400	542	1.9	222.5	386	0.98	0.94	6.72	8.18	7.03	78896	17.5	CHE
257	500	693	1.9	218.1	422	0.98	0.96	6.90	8.34	7.02	80477	16.8	CHE
257	600	865	2.0	214.4	446	0.98	0.96	6.96	8.39	7.02	81084	16.4	CHE
294	0	0	1.8	265.9	0	0.87	0.30	5.88	6.99	6.94	4649	4580.0	NE
294	25	33	1.5	288.6	1	0.84	0.25	6.35	5.83	6.94	10689	858.2	NE
294	50	66	1.5	288.2	11	0.85	0.26	6.22	6.61	6.94	11160	789.2	NE
294	75	99	1.5	287.3	15	0.87	0.29	6.09	6.84	6.94	11058	809.0	NE
294	100	132	1.7	243.1	0	0.98	0.49	5.85	7.19	6.97	4461	5133.2	TE
294	125	165	1.7	283.6	0	0.97	0.37	5.87	7.07	6.96	7377	1857.7	TE
294	150	199	1.7	288.2	418	0.98	0.42	5.79	7.14	6.97	26540	145.1	TE
294	175	232	1.7	283.2	2	0.95	0.39	5.76	7.12	6.97	9303	1176.4	TE
294	200	266	1.6	289.4	799	0.85	0.46	5.73	7.19	6.98	34223	88.4	TE
294	225	299	1.6	289.1	755	0.86	0.50	5.71	7.23	6.99	39058	68.6	TE
294	250	333	1.5	278.4	171	0.85	0.37	5.65	7.12	6.97	14452	486.6	TE
294	275	367	1.6	276.2	75	0.89	0.44	5.61	7.19	6.98	13730	549.5	TE
294	300	401	1.6	273.5	312	0.86	0.46	5.60	7.21	6.99	17371	345.4	TE
294	325	435	1.7	267.7	577	0.91	0.64	5.80	7.39	7.04	29568	126.9	TE
294	350	470	1.8	263.0	73	0.95	0.74	5.97	7.54	7.07	13412	634.2	TE
294	375	505	1.9	264.9	617	0.98	0.86	6.27	7.79	7.09	58147	34.7	TE
294	400	541	1.9	252.7	393	0.98	0.94	6.68	8.14	7.09	76220	20.2	CHE
294	450	614	1.9	250.0	400	0.98	0.95	6.76	8.21	7.09	78517	19.0	CHE
294	500	691	1.9	247.4	414	0.98	0.96	6.86	8.30	7.09	79189	18.6	CHE
294	550	773	1.9	244.9	421	0.98	0.96	6.95	8.38	7.08	80290	18.0	CHE
294	600	861	1.9	242.8	432	0.98	0.96	6.96	8.39	7.08	80368	17.9	CHE

Appendix B: Photoionizing flux (Online material)

Table B.1. Time averaged ionizing fluxes (L), and time averaged (Q) and peak photon emission rates (Q^{max}) of the ionizing photons for hydrogen (H), neutral helium (He) and singly ionised helium (He^+) during the main-sequence evolution for each stellar sequence. We emphasize that the given quantities rely on the black body approximation, and refer to Sect. 10.3 for a discussion of its validity.

M^i [M_{\odot}]	v_{rot}^i [km s^{-1}]	$L(\gamma_H)$ [erg/s]	$Q(\gamma_H)$ [s^{-1}]	$Q^{\text{max}}(\gamma_H)$ [s^{-1}]	$L(\gamma_{He})$ [erg/s]	$Q(\gamma_{He})$ [s^{-1}]	$Q^{\text{max}}(\gamma_{He})$ [s^{-1}]	$L(\gamma_{He^+})$ [erg/s]	$Q(\gamma_{He^+})$ [s^{-1}]	$Q^{\text{max}}(\gamma_{He^+})$ [s^{-1}]
9	0	4.94E+36	1.83E+47	2.22E+47	2.60E+35	5.89E+45	6.84E+45	1.53E+31	1.66E+41	2.28E+41
9	100	4.84E+36	1.80E+47	2.19E+47	2.50E+35	5.67E+45	6.61E+45	1.40E+31	1.52E+41	2.10E+41
9	200	4.40E+36	1.65E+47	1.97E+47	2.09E+35	4.77E+45	5.58E+45	9.53E+30	1.04E+41	1.49E+41
9	300	3.67E+36	1.37E+47	1.61E+47	1.46E+35	3.35E+45	3.99E+45	4.33E+30	4.73E+40	7.59E+40
9	375	3.20E+36	1.21E+47	1.43E+47	1.11E+35	2.55E+45	3.08E+45	2.19E+30	2.39E+40	3.75E+40
9	400	4.95E+36	1.84E+47	3.33E+47	2.38E+35	5.40E+45	1.00E+46	1.00E+31	1.09E+41	3.02E+41
9	425	4.09E+36	1.53E+47	2.34E+47	1.73E+35	3.95E+45	5.81E+45	5.21E+30	5.69E+40	1.17E+41
9	450	1.59E+37	5.30E+47	5.61E+48	2.99E+36	6.29E+46	1.39E+48	1.73E+34	1.81E+44	1.12E+46
9	500	1.50E+37	4.98E+47	5.45E+48	2.78E+36	5.85E+46	1.34E+48	1.57E+34	1.65E+44	1.07E+46
9	600	1.27E+37	4.25E+47	4.79E+48	2.29E+36	4.83E+46	1.14E+48	1.19E+34	1.25E+44	8.27E+45
10	0	7.82E+36	2.85E+47	3.54E+47	4.94E+35	1.11E+46	1.30E+46	4.86E+31	5.28E+41	7.07E+41
10	50	7.74E+36	2.83E+47	3.49E+47	4.86E+35	1.09E+46	1.27E+46	4.73E+31	5.14E+41	6.96E+41
10	100	7.61E+36	2.79E+47	3.43E+47	4.69E+35	1.06E+46	1.23E+46	4.38E+31	4.76E+41	6.49E+41
10	150	7.36E+36	2.70E+47	3.30E+47	4.41E+35	9.96E+45	1.16E+46	3.81E+31	4.15E+41	5.74E+41
10	200	7.00E+36	2.57E+47	3.12E+47	4.01E+35	9.06E+45	1.06E+46	3.10E+31	3.37E+41	4.77E+41
10	250	6.47E+36	2.39E+47	2.85E+47	3.46E+35	7.86E+45	9.30E+45	2.30E+31	2.49E+41	3.68E+41
10	300	5.92E+36	2.20E+47	2.60E+47	2.91E+35	6.59E+45	7.84E+45	1.53E+31	1.67E+41	2.59E+41
10	350	5.39E+36	2.01E+47	2.38E+47	2.41E+35	5.47E+45	6.58E+45	9.66E+30	1.05E+41	1.63E+41
10	375	5.29E+36	1.98E+47	2.35E+47	2.30E+35	5.24E+45	6.31E+45	8.41E+30	9.19E+40	1.42E+41
10	400	5.66E+36	2.11E+47	2.73E+47	2.59E+35	5.87E+45	7.37E+45	1.02E+31	1.11E+41	1.81E+41
10	425	6.92E+36	2.56E+47	4.07E+47	3.74E+35	8.45E+45	1.28E+46	2.25E+31	2.44E+41	5.25E+41
10	450	2.31E+37	7.61E+47	7.09E+48	4.66E+36	9.73E+46	1.85E+48	3.19E+34	3.33E+44	1.76E+46
10	500	2.18E+37	7.21E+47	6.89E+48	4.34E+36	9.07E+46	1.78E+48	2.88E+34	3.01E+44	1.66E+46
10	550	2.02E+37	6.69E+47	6.39E+48	3.90E+36	8.18E+46	1.59E+48	2.36E+34	2.46E+44	1.32E+46

Table B.1. Continued.

M^i [M_\odot]	v_{rot}^i [km s^{-1}]	$L(\gamma_H)$ [erg/s]	$Q(\gamma_H)$ [s^{-1}]	$Q^{\text{max}}(\gamma_H)$ [s^{-1}]	$L(\gamma_{He})$ [erg/s]	$Q(\gamma_{He})$ [s^{-1}]	$Q^{\text{max}}(\gamma_{He})$ [s^{-1}]	$L(\gamma_{He^+})$ [erg/s]	$Q(\gamma_{He^+})$ [s^{-1}]	$Q^{\text{max}}(\gamma_{He^+})$ [s^{-1}]
10	600	1.87E+37	6.21E+47	6.10E+48	3.63E+36	7.61E+46	1.53E+48	2.22E+34	2.33E+44	1.29E+46
11	0	1.15E+37	4.17E+47	5.17E+47	8.44E+35	1.89E+46	2.19E+46	1.27E+32	1.38E+42	1.86E+42
11	100	1.14E+37	4.12E+47	5.13E+47	8.15E+35	1.83E+46	2.15E+46	1.17E+32	1.27E+42	1.72E+42
11	200	1.05E+37	3.82E+47	4.70E+47	7.02E+35	1.58E+46	1.87E+46	8.52E+31	9.24E+41	1.29E+42
11	300	8.89E+36	3.27E+47	3.88E+47	5.15E+35	1.16E+46	1.38E+46	4.36E+31	4.74E+41	7.35E+41
11	400	8.18E+36	3.03E+47	3.82E+47	4.27E+35	9.68E+45	1.18E+46	2.54E+31	2.78E+41	4.36E+41
11	425	1.02E+37	3.75E+47	5.84E+47	6.43E+35	1.45E+46	2.11E+46	5.96E+31	6.48E+41	1.34E+42
11	450	3.18E+37	1.04E+48	8.51E+48	6.75E+36	1.41E+47	2.28E+48	5.09E+34	5.31E+44	2.36E+46
11	500	3.01E+37	9.87E+47	8.30E+48	6.30E+36	1.31E+47	2.20E+48	4.58E+34	4.79E+44	2.21E+46
11	600	2.60E+37	8.56E+47	7.46E+48	5.33E+36	1.12E+47	1.94E+48	3.70E+34	3.86E+44	1.84E+46
12	375	1.15E+37	4.23E+47	5.05E+47	6.84E+35	1.54E+46	1.85E+46	6.25E+31	6.80E+41	1.05E+42
12	400	1.22E+37	4.47E+47	5.74E+47	7.56E+35	1.71E+46	2.12E+46	7.36E+31	8.00E+41	1.28E+42
12	425	1.72E+37	6.16E+47	1.11E+48	1.42E+36	3.17E+46	5.43E+46	2.96E+32	3.20E+42	8.19E+42
12	450	4.23E+37	1.37E+48	1.01E+49	9.48E+36	1.97E+47	2.81E+48	7.99E+34	8.31E+44	3.23E+46
13	0	2.21E+37	7.86E+47	9.86E+47	2.06E+36	4.57E+46	5.33E+46	6.25E+32	6.75E+42	9.00E+42
13	100	2.18E+37	7.75E+47	9.71E+47	2.00E+36	4.44E+46	5.17E+46	5.79E+32	6.25E+42	8.40E+42
13	200	2.03E+37	7.29E+47	8.97E+47	1.75E+36	3.91E+46	4.56E+46	4.37E+32	4.73E+42	6.55E+42
13	300	1.77E+37	6.40E+47	7.67E+47	1.34E+36	2.99E+46	3.61E+46	2.49E+32	2.69E+42	4.12E+42
13	350	1.67E+37	6.04E+47	7.31E+47	1.18E+36	2.64E+46	3.20E+46	1.80E+32	1.95E+42	2.97E+42
13	375	1.83E+37	6.60E+47	8.55E+47	1.38E+36	3.10E+46	3.98E+46	2.36E+32	2.56E+42	4.22E+42
13	400	2.04E+37	7.35E+47	1.09E+48	1.69E+36	3.78E+46	5.41E+46	3.55E+32	3.84E+42	7.59E+42
13	425	2.07E+37	7.42E+47	1.16E+48	1.72E+36	3.83E+46	5.65E+46	3.65E+32	3.94E+42	8.19E+42
13	450	5.47E+37	1.75E+48	1.18E+49	1.28E+37	2.65E+47	3.37E+48	1.18E+35	1.23E+45	4.20E+46
13	500	5.29E+37	1.71E+48	1.20E+49	1.24E+37	2.56E+47	3.49E+48	1.17E+35	1.22E+45	4.61E+46
13	600	4.73E+37	1.53E+48	1.11E+49	1.09E+37	2.27E+47	3.18E+48	1.00E+35	1.04E+45	4.04E+46
15	0	3.73E+37	1.31E+48	1.65E+48	4.19E+36	9.21E+46	1.08E+47	2.16E+33	2.32E+43	3.12E+43
15	100	3.70E+37	1.30E+48	1.63E+48	4.05E+36	8.91E+46	1.05E+47	2.01E+33	2.16E+43	2.93E+43
15	200	3.47E+37	1.22E+48	1.51E+48	3.61E+36	7.96E+46	9.38E+46	1.56E+33	1.68E+43	2.35E+43
15	300	3.06E+37	1.09E+48	1.31E+48	2.83E+36	6.29E+46	7.59E+46	9.49E+32	1.03E+43	1.56E+43
15	375	2.76E+37	9.95E+47	1.19E+48	2.31E+36	5.14E+46	6.19E+46	5.65E+32	6.11E+42	9.52E+42
15	400	2.92E+37	1.04E+48	1.33E+48	2.52E+36	5.63E+46	6.94E+46	6.55E+32	7.07E+42	1.13E+43
15	412	3.14E+37	1.12E+48	1.53E+48	2.90E+36	6.46E+46	8.39E+46	8.63E+32	9.31E+42	1.61E+43
15	425	8.87E+37	2.79E+48	1.61E+49	2.29E+37	4.71E+47	4.94E+48	2.70E+35	2.79E+45	7.82E+46
15	500	8.17E+37	2.60E+48	1.54E+49	2.03E+37	4.19E+47	4.57E+48	2.14E+35	2.21E+45	6.50E+46
15	600	7.42E+37	2.36E+48	1.45E+49	1.83E+37	3.77E+47	4.30E+48	1.90E+35	1.99E+45	6.08E+46
17	0	5.80E+37	2.01E+48	2.52E+48	7.46E+36	1.63E+47	1.91E+47	5.91E+33	6.33E+43	8.56E+43
17	100	5.73E+37	1.98E+48	2.49E+48	7.29E+36	1.59E+47	1.86E+47	5.56E+33	5.98E+43	8.07E+43
17	200	5.41E+37	1.88E+48	2.33E+48	6.52E+36	1.43E+47	1.69E+47	4.41E+33	4.75E+43	6.65E+43
17	300	5.18E+37	1.81E+48	2.27E+48	5.98E+36	1.32E+47	1.65E+47	3.70E+33	3.96E+43	6.02E+43
17	350	4.59E+37	1.62E+48	1.97E+48	4.78E+36	1.06E+47	1.28E+47	2.23E+33	2.40E+43	3.75E+43
17	375	5.41E+37	1.89E+48	2.57E+48	6.35E+36	1.39E+47	1.88E+47	3.83E+33	4.12E+43	7.35E+43
17	400	1.33E+38	4.13E+48	2.10E+49	3.81E+37	7.72E+47	7.00E+48	5.70E+35	5.86E+45	1.42E+47
17	500	1.21E+38	3.78E+48	2.01E+49	3.27E+37	6.69E+47	6.40E+48	4.19E+35	4.34E+45	1.13E+47
17	600	1.08E+38	3.40E+48	1.82E+49	2.80E+37	5.75E+47	5.57E+48	3.21E+35	3.32E+45	8.56E+46
20	0	9.84E+37	3.35E+48	4.20E+48	1.50E+37	3.24E+47	3.80E+47	1.95E+34	2.08E+44	2.83E+44
20	50	9.84E+37	3.34E+48	4.19E+48	1.49E+37	3.23E+47	3.79E+47	1.93E+34	2.06E+44	2.80E+44
20	100	9.72E+37	3.31E+48	4.14E+48	1.46E+37	3.17E+47	3.71E+47	1.84E+34	1.97E+44	2.68E+44
20	150	9.54E+37	3.25E+48	4.04E+48	1.40E+37	3.04E+47	3.58E+47	1.68E+34	1.80E+44	2.50E+44
20	200	9.21E+37	3.16E+48	3.90E+48	1.32E+37	2.87E+47	3.40E+47	1.50E+34	1.61E+44	2.27E+44
20	250	8.86E+37	3.04E+48	3.75E+48	1.23E+37	2.68E+47	3.23E+47	1.31E+34	1.40E+44	2.03E+44
20	300	8.62E+37	2.97E+48	3.64E+48	1.17E+37	2.54E+47	3.14E+47	1.17E+34	1.26E+44	1.89E+44
20	325	8.49E+37	2.93E+48	3.63E+48	1.13E+37	2.46E+47	3.08E+47	1.08E+34	1.16E+44	1.82E+44
20	350	8.63E+37	2.97E+48	3.75E+48	1.15E+37	2.52E+47	3.15E+47	1.10E+34	1.18E+44	1.90E+44
20	375	8.86E+37	3.05E+48	3.95E+48	1.20E+37	2.61E+47	3.36E+47	1.14E+34	1.22E+44	2.04E+44
20	400	2.10E+38	6.39E+48	2.78E+49	6.48E+37	1.31E+48	9.72E+48	1.15E+36	1.17E+46	2.28E+47
20	450	1.96E+38	6.03E+48	2.61E+49	5.75E+37	1.17E+48	8.60E+48	8.51E+35	8.76E+45	1.67E+47
20	500	1.91E+38	5.91E+48	2.65E+49	5.55E+37	1.13E+48	8.76E+48	8.15E+35	8.40E+45	1.73E+47
20	550	1.81E+38	5.61E+48	2.55E+49	5.14E+37	1.05E+48	8.23E+48	7.07E+35	7.28E+45	1.51E+47
20	600	1.76E+38	5.44E+48	2.56E+49	5.03E+37	1.02E+48	8.48E+48	7.33E+35	7.53E+45	1.69E+47
23	0	1.51E+38	5.05E+48	6.32E+48	2.60E+37	5.60E+47	6.57E+47	4.98E+34	5.30E+44	7.26E+44

Table B.1. Continued.

M^i [M_{\odot}]	v_{rot}^i [km s^{-1}]	$L(\gamma_H)$ [erg/s]	$Q(\gamma_H)$ [s^{-1}]	$Q^{\text{max}}(\gamma_H)$ [s^{-1}]	$L(\gamma_{He})$ [erg/s]	$Q(\gamma_{He})$ [s^{-1}]	$Q^{\text{max}}(\gamma_{He})$ [s^{-1}]	$L(\gamma_{He^+})$ [erg/s]	$Q(\gamma_{He^+})$ [s^{-1}]	$Q^{\text{max}}(\gamma_{He^+})$ [s^{-1}]
23	100	1.49E+38	5.00E+48	6.23E+48	2.54E+37	5.44E+47	6.42E+47	4.72E+34	5.03E+44	6.93E+44
23	200	1.42E+38	4.78E+48	5.90E+48	2.31E+37	4.97E+47	5.94E+47	3.90E+34	4.16E+44	5.97E+44
23	300	1.38E+38	4.66E+48	5.87E+48	2.22E+37	4.80E+47	6.06E+47	3.60E+34	3.84E+44	5.85E+44
23	325	1.41E+38	4.76E+48	6.06E+48	2.27E+37	4.89E+47	6.32E+47	3.78E+34	4.03E+44	6.52E+44
23	350	1.46E+38	4.91E+48	6.47E+48	2.40E+37	5.17E+47	6.86E+47	4.14E+34	4.40E+44	7.75E+44
23	375	3.07E+38	9.18E+48	3.48E+49	1.02E+38	2.04E+48	1.26E+49	2.06E+36	2.10E+46	3.26E+47
23	400	3.05E+38	9.15E+48	3.55E+49	1.01E+38	2.02E+48	1.30E+49	2.06E+36	2.11E+46	3.50E+47
23	500	2.79E+38	8.48E+48	3.39E+49	8.67E+37	1.75E+48	1.18E+49	1.47E+36	1.52E+46	2.70E+47
23	600	2.56E+38	7.85E+48	3.21E+49	7.72E+37	1.56E+48	1.09E+49	1.22E+36	1.26E+46	2.32E+47
26	0	2.15E+38	7.08E+48	8.81E+48	4.08E+37	8.68E+47	1.02E+48	1.06E+35	1.12E+45	1.55E+45
26	100	2.11E+38	7.03E+48	8.67E+48	3.95E+37	8.44E+47	9.99E+47	9.91E+34	1.05E+45	1.48E+45
26	200	2.02E+38	6.75E+48	8.25E+48	3.65E+37	7.82E+47	9.32E+47	8.44E+34	9.00E+44	1.29E+45
26	300	1.91E+38	6.41E+48	7.85E+48	3.31E+37	7.09E+47	8.92E+47	7.15E+34	7.57E+44	1.17E+45
26	325	2.10E+38	7.00E+48	9.07E+48	3.92E+37	8.34E+47	1.11E+48	9.83E+34	1.04E+45	1.76E+45
26	350	4.34E+38	1.27E+49	4.44E+49	1.55E+38	3.07E+48	1.71E+49	3.81E+36	3.88E+46	5.51E+47
26	375	4.15E+38	1.22E+49	4.18E+49	1.44E+38	2.86E+48	1.53E+49	3.13E+36	3.19E+46	4.17E+47
26	400	4.16E+38	1.23E+49	4.30E+49	1.44E+38	2.86E+48	1.61E+49	3.23E+36	3.30E+46	4.66E+47
26	500	3.81E+38	1.14E+49	4.11E+49	1.24E+38	2.49E+48	1.47E+49	2.33E+36	2.39E+46	3.67E+47
26	600	3.56E+38	1.08E+49	4.02E+49	1.13E+38	2.28E+48	1.43E+49	2.07E+36	2.13E+46	3.59E+47
30	0	3.15E+38	1.03E+49	1.26E+49	6.64E+37	1.40E+48	1.65E+48	2.35E+35	2.49E+45	3.49E+45
30	100	3.12E+38	1.02E+49	1.25E+49	6.49E+37	1.38E+48	1.62E+48	2.25E+35	2.38E+45	3.36E+45
30	200	2.98E+38	9.80E+48	1.19E+49	5.99E+37	1.27E+48	1.52E+48	1.93E+35	2.04E+45	3.00E+45
30	300	2.90E+38	9.51E+48	1.17E+49	5.81E+37	1.23E+48	1.52E+48	1.83E+35	1.94E+45	2.92E+45
30	325	3.13E+38	1.02E+49	1.31E+49	6.57E+37	1.38E+48	1.83E+48	2.33E+35	2.47E+45	4.14E+45
30	350	5.88E+38	1.71E+49	5.24E+49	2.17E+38	4.28E+48	1.98E+49	5.36E+36	5.46E+46	5.96E+47
30	400	5.73E+38	1.68E+49	5.22E+49	2.08E+38	4.12E+48	1.96E+49	4.95E+36	5.04E+46	5.71E+47
30	500	5.48E+38	1.62E+49	5.29E+49	1.91E+38	3.79E+48	2.01E+49	4.27E+36	4.36E+46	6.06E+47
30	600	5.04E+38	1.50E+49	4.98E+49	1.68E+38	3.36E+48	1.82E+49	3.33E+36	3.41E+46	4.87E+47
34	0	4.33E+38	1.40E+49	1.70E+49	9.73E+37	2.05E+48	2.44E+48	4.42E+35	4.66E+45	6.72E+45
34	100	4.28E+38	1.38E+49	1.68E+49	9.63E+37	2.02E+48	2.40E+48	4.28E+35	4.52E+45	6.52E+45
34	200	4.13E+38	1.34E+49	1.61E+49	9.04E+37	1.89E+48	2.26E+48	3.76E+35	3.97E+45	5.84E+45
34	275	3.94E+38	1.28E+49	1.58E+49	8.40E+37	1.77E+48	2.24E+48	3.44E+35	3.64E+45	5.64E+45
34	300	4.35E+38	1.40E+49	1.79E+49	9.97E+37	2.09E+48	2.75E+48	4.75E+35	5.01E+45	8.13E+45
34	325	8.13E+38	2.33E+49	6.72E+49	3.21E+38	6.27E+48	2.74E+49	9.67E+36	9.83E+46	1.04E+48
34	350	8.03E+38	2.30E+49	6.65E+49	3.14E+38	6.13E+48	2.68E+49	9.25E+36	9.41E+46	9.84E+47
34	400	7.78E+38	2.25E+49	6.53E+49	2.99E+38	5.85E+48	2.58E+49	8.30E+36	8.46E+46	8.94E+47
34	500	7.28E+38	2.13E+49	6.34E+49	2.64E+38	5.21E+48	2.44E+49	6.37E+36	6.47E+46	7.70E+47
34	600	6.81E+38	2.01E+49	6.16E+49	2.40E+38	4.76E+48	2.36E+49	5.45E+36	5.60E+46	7.35E+47
39	0	5.99E+38	1.91E+49	2.30E+49	1.45E+38	3.03E+48	3.61E+48	8.39E+35	8.87E+45	1.30E+46
39	50	5.98E+38	1.91E+49	2.29E+49	1.45E+38	3.02E+48	3.60E+48	8.30E+35	8.78E+45	1.29E+46
39	100	5.93E+38	1.90E+49	2.27E+49	1.43E+38	2.98E+48	3.56E+48	8.12E+35	8.52E+45	1.26E+46
39	150	5.87E+38	1.88E+49	2.24E+49	1.40E+38	2.92E+48	3.48E+48	7.71E+35	8.11E+45	1.21E+46
39	200	5.75E+38	1.85E+49	2.20E+49	1.35E+38	2.83E+48	3.40E+48	7.26E+35	7.64E+45	1.15E+46
39	250	5.64E+38	1.80E+49	2.20E+49	1.33E+38	2.77E+48	3.43E+48	7.20E+35	7.58E+45	1.15E+46
39	275	5.66E+38	1.81E+49	2.23E+49	1.35E+38	2.81E+48	3.55E+48	7.49E+35	7.91E+45	1.22E+46
39	300	6.24E+38	1.98E+49	2.57E+49	1.57E+38	3.27E+48	4.44E+48	1.03E+36	1.08E+46	1.85E+46
39	325	1.07E+39	3.02E+49	7.91E+49	4.32E+38	8.43E+48	3.17E+49	1.33E+37	1.34E+47	1.14E+48
39	350	1.05E+39	3.00E+49	7.84E+49	4.25E+38	8.27E+48	3.12E+49	1.28E+37	1.30E+47	1.10E+48
39	400	1.04E+39	2.98E+49	7.91E+49	4.17E+38	8.12E+48	3.17E+49	1.25E+37	1.27E+47	1.14E+48
39	450	1.03E+39	2.94E+49	7.97E+49	4.04E+38	7.90E+48	3.23E+49	1.18E+37	1.20E+47	1.20E+48
39	500	9.64E+38	2.80E+49	7.50E+49	3.61E+38	7.12E+48	2.85E+49	8.93E+36	9.11E+46	8.76E+47
39	550	9.42E+38	2.75E+49	7.53E+49	3.49E+38	6.91E+48	2.90E+49	8.56E+36	8.68E+46	9.23E+47
39	600	9.19E+38	2.68E+49	7.45E+49	3.35E+38	6.61E+48	2.88E+49	8.12E+36	8.23E+46	9.23E+47
45	0	8.28E+38	2.61E+49	3.10E+49	2.16E+38	4.47E+48	5.30E+48	1.57E+36	1.64E+46	2.44E+46
45	100	8.22E+38	2.59E+49	3.07E+49	2.13E+38	4.41E+48	5.23E+48	1.52E+36	1.59E+46	2.38E+46
45	200	8.01E+38	2.53E+49	2.99E+49	2.02E+38	4.19E+48	5.07E+48	1.36E+36	1.43E+46	2.22E+46
45	250	7.84E+38	2.48E+49	3.03E+49	1.99E+38	4.12E+48	5.22E+48	1.40E+36	1.47E+46	2.30E+46
45	275	8.10E+38	2.55E+49	3.19E+49	2.12E+38	4.38E+48	5.68E+48	1.60E+36	1.67E+46	2.67E+46
45	300	8.50E+38	2.66E+49	3.37E+49	2.27E+38	4.68E+48	6.24E+48	1.83E+36	1.92E+46	3.22E+46
45	325	1.42E+39	4.00E+49	9.65E+49	5.98E+38	1.16E+49	3.91E+49	1.98E+37	2.01E+47	1.47E+48

Table B.1. Continued.

M^i [M_\odot]	v_{rot}^i [km s^{-1}]	$L(\gamma_H)$ [erg/s]	$Q(\gamma_H)$ [s^{-1}]	$Q^{\text{max}}(\gamma_H)$ [s^{-1}]	$L(\gamma_{He})$ [erg/s]	$Q(\gamma_{He})$ [s^{-1}]	$Q^{\text{max}}(\gamma_{He})$ [s^{-1}]	$L(\gamma_{He^+})$ [erg/s]	$Q(\gamma_{He^+})$ [s^{-1}]	$Q^{\text{max}}(\gamma_{He^+})$ [s^{-1}]
45	400	1.40E+39	3.94E+49	9.62E+49	5.80E+38	1.13E+49	3.90E+49	1.87E+37	1.90E+47	1.46E+48
45	500	1.30E+39	3.74E+49	9.23E+49	5.10E+38	9.97E+48	3.60E+49	1.40E+37	1.42E+47	1.19E+48
45	600	1.22E+39	3.53E+49	8.84E+49	4.56E+38	8.99E+48	3.37E+49	1.11E+37	1.14E+47	1.03E+48
48	275	8.78E+38	2.77E+49	3.40E+49	2.27E+38	4.69E+48	6.06E+48	1.73E+36	1.81E+46	2.93E+46
48	300	9.36E+38	2.94E+49	3.67E+49	2.54E+38	5.22E+48	6.89E+48	2.14E+36	2.25E+46	3.71E+46
48	325	1.63E+39	4.54E+49	1.07E+50	6.97E+38	1.34E+49	4.39E+49	2.43E+37	2.46E+47	1.73E+48
51	0	1.07E+39	3.34E+49	3.96E+49	2.91E+38	5.99E+48	7.24E+48	2.50E+36	2.62E+46	4.04E+46
51	100	1.07E+39	3.33E+49	3.94E+49	2.88E+38	5.93E+48	7.16E+48	2.43E+36	2.55E+46	3.95E+46
51	200	1.05E+39	3.30E+49	3.84E+49	2.80E+38	5.78E+48	6.96E+48	2.27E+36	2.37E+46	3.71E+46
51	250	1.01E+39	3.16E+49	3.83E+49	2.67E+38	5.51E+48	7.02E+48	2.22E+36	2.32E+46	3.71E+46
51	275	1.01E+39	3.17E+49	3.93E+49	2.72E+38	5.61E+48	7.34E+48	2.35E+36	2.45E+46	4.00E+46
51	287	1.06E+39	3.30E+49	4.08E+49	2.93E+38	6.01E+48	7.81E+48	2.65E+36	2.77E+46	4.48E+46
51	300	1.84E+39	5.10E+49	1.16E+50	8.00E+38	1.54E+49	4.83E+49	2.89E+37	2.92E+47	1.95E+48
51	400	1.81E+39	5.02E+49	1.16E+50	7.72E+38	1.49E+49	4.81E+49	2.73E+37	2.77E+47	1.96E+48
51	500	1.71E+39	4.84E+49	1.13E+50	7.03E+38	1.36E+49	4.66E+49	2.23E+37	2.26E+47	1.82E+48
51	600	1.60E+39	4.57E+49	1.08E+50	6.26E+38	1.23E+49	4.32E+49	1.76E+37	1.78E+47	1.54E+48
55	225	1.21E+39	3.77E+49	4.44E+49	3.31E+38	6.80E+48	8.40E+48	2.99E+36	3.12E+46	4.97E+46
55	250	1.25E+39	3.88E+49	4.74E+49	3.58E+38	7.33E+48	9.34E+48	3.60E+36	3.75E+46	5.91E+46
55	275	2.16E+39	5.94E+49	1.32E+50	9.57E+38	1.83E+49	5.65E+49	3.68E+37	3.72E+47	2.50E+48
55	300	2.14E+39	5.90E+49	1.31E+50	9.49E+38	1.82E+49	5.53E+49	3.65E+37	3.69E+47	2.39E+48
59	0	1.44E+39	4.44E+49	5.20E+49	4.15E+38	8.50E+48	1.02E+49	4.29E+36	4.47E+46	6.99E+46
59	100	1.43E+39	4.45E+49	5.18E+49	4.13E+38	8.45E+48	1.01E+49	4.19E+36	4.36E+46	6.86E+46
59	200	1.43E+39	4.42E+49	5.08E+49	3.98E+38	8.17E+48	9.92E+48	3.85E+36	4.01E+46	6.51E+46
59	225	1.42E+39	4.41E+49	5.19E+49	4.06E+38	8.31E+48	1.03E+49	4.16E+36	4.33E+46	6.86E+46
59	250	1.53E+39	4.69E+49	5.83E+49	4.72E+38	9.57E+48	1.23E+49	5.65E+36	5.87E+46	9.31E+46
59	275	2.43E+39	6.69E+49	1.44E+50	1.09E+39	2.09E+49	6.10E+49	4.24E+37	4.28E+47	2.64E+48
59	300	2.42E+39	6.66E+49	1.42E+50	1.09E+39	2.08E+49	6.00E+49	4.24E+37	4.28E+47	2.56E+48
59	400	2.39E+39	6.58E+49	1.42E+50	1.07E+39	2.04E+49	6.06E+49	4.13E+37	4.17E+47	2.68E+48
59	500	2.20E+39	6.19E+49	1.33E+50	9.23E+38	1.80E+49	5.30E+49	2.93E+37	2.97E+47	1.89E+48
59	600	2.09E+39	5.95E+49	1.30E+50	8.39E+38	1.64E+49	5.19E+49	2.46E+37	2.50E+47	1.84E+48
67	0	1.82E+39	5.59E+49	6.51E+49	5.49E+38	1.12E+49	1.35E+49	6.52E+36	6.78E+46	1.09E+47
67	100	1.84E+39	5.62E+49	6.50E+49	5.49E+38	1.12E+49	1.35E+49	6.41E+36	6.66E+46	1.07E+47
67	200	1.82E+39	5.63E+49	6.40E+49	5.34E+38	1.09E+49	1.33E+49	5.98E+36	6.21E+46	1.02E+47
67	225	1.80E+39	5.57E+49	6.47E+49	5.36E+38	1.09E+49	1.36E+49	6.26E+36	6.51E+46	1.05E+47
67	250	1.97E+39	5.93E+49	7.16E+49	6.42E+38	1.29E+49	1.59E+49	8.73E+36	9.05E+46	1.35E+47
67	275	3.04E+39	8.30E+49	1.69E+50	1.39E+39	2.65E+49	7.19E+49	5.63E+37	5.68E+47	3.13E+48
67	300	3.03E+39	8.26E+49	1.68E+50	1.40E+39	2.65E+49	7.11E+49	5.70E+37	5.76E+47	3.08E+48
67	400	2.93E+39	8.03E+49	1.62E+50	1.32E+39	2.53E+49	6.68E+49	5.05E+37	5.10E+47	2.66E+48
67	500	2.80E+39	7.80E+49	1.59E+50	1.22E+39	2.34E+49	6.47E+49	4.18E+37	4.24E+47	2.47E+48
67	600	2.67E+39	7.51E+49	1.56E+50	1.11E+39	2.16E+49	6.37E+49	3.53E+37	3.59E+47	2.44E+48
77	0	2.35E+39	7.14E+49	8.25E+49	7.39E+38	1.49E+49	1.81E+49	1.00E+37	1.04E+47	1.70E+47
77	50	2.29E+39	6.96E+49	8.24E+49	7.09E+38	1.44E+49	1.81E+49	9.61E+36	9.97E+46	1.69E+47
77	100	2.32E+39	7.07E+49	8.23E+49	7.12E+38	1.45E+49	1.80E+49	9.45E+36	9.81E+46	1.67E+47
77	150	2.37E+39	7.23E+49	8.19E+49	7.22E+38	1.47E+49	1.79E+49	9.28E+36	9.61E+46	1.64E+47
77	175	2.37E+39	7.26E+49	8.18E+49	7.24E+38	1.47E+49	1.79E+49	9.28E+36	9.62E+46	1.63E+47
77	200	2.36E+39	7.21E+49	8.19E+49	7.20E+38	1.47E+49	1.81E+49	9.41E+36	9.75E+46	1.64E+47
77	225	2.59E+39	7.78E+49	9.24E+49	8.51E+38	1.71E+49	2.16E+49	1.30E+37	1.34E+47	2.13E+47
77	250	2.67E+39	7.93E+49	1.02E+50	9.25E+38	1.85E+49	2.52E+49	1.62E+37	1.68E+47	2.87E+47
77	275	3.82E+39	1.04E+50	1.99E+50	1.77E+39	3.37E+49	8.32E+49	7.25E+37	7.32E+47	3.44E+48
77	300	3.82E+39	1.03E+50	1.98E+50	1.79E+39	3.39E+49	8.34E+49	7.54E+37	7.61E+47	3.54E+48
77	350	3.91E+39	1.05E+50	2.04E+50	1.86E+39	3.51E+49	9.06E+49	8.47E+37	8.52E+47	4.55E+48
77	400	3.83E+39	1.04E+50	2.00E+50	1.80E+39	3.40E+49	8.70E+49	7.77E+37	7.84E+47	4.08E+48
77	450	3.72E+39	1.02E+50	1.96E+50	1.71E+39	3.25E+49	8.28E+49	6.87E+37	6.94E+47	3.57E+48
77	500	3.61E+39	9.91E+49	1.91E+50	1.61E+39	3.09E+49	7.94E+49	6.00E+37	6.08E+47	3.21E+48
77	550	3.59E+39	9.92E+49	1.95E+50	1.59E+39	3.05E+49	8.46E+49	6.10E+37	6.15E+47	3.94E+48
77	600	3.42E+39	9.55E+49	1.87E+50	1.46E+39	2.83E+49	7.74E+49	4.97E+37	5.04E+47	3.09E+48
88	0	2.87E+39	8.70E+49	1.03E+50	9.28E+38	1.87E+49	2.37E+49	1.42E+37	1.47E+47	2.54E+47
88	100	2.95E+39	8.91E+49	1.02E+50	9.40E+38	1.90E+49	2.35E+49	1.40E+37	1.45E+47	2.50E+47
88	150	3.01E+39	9.11E+49	1.02E+50	9.55E+38	1.93E+49	2.34E+49	1.39E+37	1.43E+47	2.46E+47
88	175	3.04E+39	9.21E+49	1.03E+50	9.75E+38	1.96E+49	2.37E+49	1.43E+37	1.48E+47	2.47E+47

Table B.1. Continued.

M^i [M_{\odot}]	v_{rot}^i [km s^{-1}]	$L(\gamma_H)$ [erg/s]	$Q(\gamma_H)$ [s^{-1}]	$Q^{\text{max}}(\gamma_H)$ [s^{-1}]	$L(\gamma_{He})$ [erg/s]	$Q(\gamma_{He})$ [s^{-1}]	$Q^{\text{max}}(\gamma_{He})$ [s^{-1}]	$L(\gamma_{He^+})$ [erg/s]	$Q(\gamma_{He^+})$ [s^{-1}]	$Q^{\text{max}}(\gamma_{He^+})$ [s^{-1}]
88	200	2.95E+39	8.94E+49	1.03E+50	9.23E+38	1.86E+49	2.39E+49	1.37E+37	1.42E+47	2.48E+47
88	225	2.91E+39	8.75E+49	1.07E+50	9.63E+38	1.93E+49	2.54E+49	1.58E+37	1.63E+47	2.70E+47
88	250	4.31E+39	1.23E+50	1.87E+50	1.73E+39	3.40E+49	5.34E+49	4.34E+37	4.45E+47	8.65E+47
88	275	4.79E+39	1.29E+50	2.36E+50	2.26E+39	4.28E+49	9.71E+49	9.40E+37	9.49E+47	3.82E+48
88	300	4.84E+39	1.29E+50	2.39E+50	2.32E+39	4.38E+49	1.03E+50	1.06E+38	1.07E+48	4.77E+48
88	400	4.70E+39	1.27E+50	2.31E+50	2.21E+39	4.20E+49	9.78E+49	9.61E+37	9.69E+47	4.21E+48
88	500	4.58E+39	1.25E+50	2.30E+50	2.11E+39	4.03E+49	9.87E+49	8.67E+37	8.74E+47	4.42E+48
88	600	4.23E+39	1.17E+50	2.18E+50	1.84E+39	3.54E+49	8.87E+49	6.29E+37	6.38E+47	3.37E+48
100	0	3.48E+39	1.05E+50	1.25E+50	1.16E+39	2.32E+49	3.01E+49	1.94E+37	2.01E+47	3.64E+47
100	25	3.47E+39	1.04E+50	1.25E+50	1.15E+39	2.31E+49	3.01E+49	1.94E+37	2.00E+47	3.64E+47
100	50	3.48E+39	1.04E+50	1.25E+50	1.15E+39	2.31E+49	3.01E+49	1.93E+37	2.00E+47	3.63E+47
100	75	3.52E+39	1.06E+50	1.25E+50	1.16E+39	2.32E+49	3.00E+49	1.92E+37	1.99E+47	3.61E+47
100	100	3.58E+39	1.08E+50	1.25E+50	1.17E+39	2.36E+49	3.00E+49	1.93E+37	1.98E+47	3.58E+47
100	150	3.74E+39	1.12E+50	1.25E+50	1.22E+39	2.45E+49	2.99E+49	1.94E+37	2.01E+47	3.53E+47
100	175	3.73E+39	1.13E+50	1.25E+50	1.22E+39	2.45E+49	3.01E+49	1.95E+37	2.01E+47	3.51E+47
100	200	4.01E+39	1.19E+50	1.35E+50	1.37E+39	2.72E+49	3.38E+49	2.41E+37	2.49E+47	4.00E+47
100	225	4.95E+39	1.42E+50	1.93E+50	1.97E+39	3.86E+49	4.98E+49	4.41E+37	4.54E+47	6.44E+47
100	250	4.88E+39	1.40E+50	1.97E+50	1.90E+39	3.75E+49	5.57E+49	4.69E+37	4.81E+47	8.48E+47
100	275	5.41E+39	1.51E+50	2.29E+50	2.31E+39	4.49E+49	6.98E+49	6.85E+37	7.00E+47	1.36E+48
100	300	5.85E+39	1.56E+50	2.75E+50	2.83E+39	5.33E+49	1.17E+50	1.29E+38	1.31E+48	5.09E+48
100	400	5.90E+39	1.57E+50	2.78E+50	2.87E+39	5.40E+49	1.23E+50	1.37E+38	1.39E+48	6.15E+48
100	500	5.61E+39	1.52E+50	2.68E+50	2.63E+39	4.99E+49	1.14E+50	1.11E+38	1.12E+48	5.03E+48
100	600	5.26E+39	1.45E+50	2.58E+50	2.33E+39	4.48E+49	1.07E+50	8.53E+37	8.63E+47	4.27E+48
115	0	4.45E+39	1.33E+50	1.55E+50	1.52E+39	3.05E+49	3.88E+49	2.82E+37	2.91E+47	5.25E+47
115	25	4.45E+39	1.33E+50	1.55E+50	1.53E+39	3.04E+49	3.88E+49	2.82E+37	2.89E+47	5.25E+47
115	50	4.46E+39	1.33E+50	1.54E+50	1.53E+39	3.04E+49	3.88E+49	2.80E+37	2.89E+47	5.23E+47
115	75	4.32E+39	1.29E+50	1.54E+50	1.46E+39	2.92E+49	3.87E+49	2.66E+37	2.75E+47	5.21E+47
115	100	4.43E+39	1.33E+50	1.55E+50	1.49E+39	2.96E+49	3.86E+49	2.66E+37	2.75E+47	5.18E+47
115	125	4.55E+39	1.36E+50	1.54E+50	1.51E+39	3.03E+49	3.86E+49	2.67E+37	2.76E+47	5.14E+47
115	150	4.75E+39	1.41E+50	1.57E+50	1.58E+39	3.18E+49	3.89E+49	2.77E+37	2.86E+47	5.11E+47
115	175	4.83E+39	1.44E+50	1.58E+50	1.63E+39	3.27E+49	3.98E+49	2.90E+37	2.99E+47	5.15E+47
115	200	5.51E+39	1.60E+50	1.95E+50	2.04E+39	4.06E+49	4.76E+49	4.18E+37	4.31E+47	6.16E+47
115	225	5.24E+39	1.52E+50	1.91E+50	1.98E+39	3.91E+49	5.24E+49	4.57E+37	4.71E+47	7.18E+47
115	250	5.55E+39	1.61E+50	2.16E+50	2.12E+39	4.17E+49	6.01E+49	5.23E+37	5.36E+47	8.91E+47
115	275	6.16E+39	1.75E+50	2.39E+50	2.50E+39	4.87E+49	7.01E+49	6.83E+37	6.98E+47	1.20E+48
115	300	7.46E+39	1.97E+50	3.39E+50	3.68E+39	6.92E+49	1.51E+50	1.84E+38	1.85E+48	7.72E+48
115	400	7.29E+39	1.93E+50	3.28E+50	3.59E+39	6.75E+49	1.44E+50	1.77E+38	1.78E+48	7.05E+48
115	500	6.93E+39	1.87E+50	3.15E+50	3.29E+39	6.25E+49	1.33E+50	1.43E+38	1.45E+48	5.74E+48
115	600	6.74E+39	1.83E+50	3.15E+50	3.09E+39	5.91E+49	1.38E+50	1.30E+38	1.31E+48	6.57E+48
131	0	5.41E+39	1.59E+50	1.87E+50	1.89E+39	3.77E+49	4.87E+49	3.78E+37	3.89E+47	7.21E+47
131	25	5.39E+39	1.59E+50	1.87E+50	1.89E+39	3.75E+49	4.87E+49	3.75E+37	3.87E+47	7.24E+47
131	50	5.41E+39	1.61E+50	1.87E+50	1.89E+39	3.75E+49	4.86E+49	3.75E+37	3.86E+47	7.22E+47
131	75	5.24E+39	1.55E+50	1.87E+50	1.82E+39	3.61E+49	4.85E+49	3.56E+37	3.67E+47	7.18E+47
131	100	5.39E+39	1.60E+50	1.87E+50	1.84E+39	3.67E+49	4.84E+49	3.56E+37	3.67E+47	7.12E+47
131	125	5.56E+39	1.66E+50	1.88E+50	1.88E+39	3.75E+49	4.85E+49	3.59E+37	3.69E+47	7.08E+47
131	150	5.67E+39	1.69E+50	1.88E+50	1.91E+39	3.82E+49	4.87E+49	3.62E+37	3.74E+47	7.03E+47
131	175	5.60E+39	1.68E+50	1.89E+50	1.90E+39	3.79E+49	4.97E+49	3.74E+37	3.84E+47	7.06E+47
131	200	6.04E+39	1.77E+50	2.07E+50	2.20E+39	4.35E+49	5.59E+49	4.91E+37	5.05E+47	7.80E+47
131	225	6.32E+39	1.83E+50	2.28E+50	2.40E+39	4.72E+49	6.28E+49	5.80E+37	5.96E+47	8.82E+47
131	250	7.10E+39	2.03E+50	2.49E+50	2.78E+39	5.48E+49	6.71E+49	6.65E+37	6.83E+47	1.01E+48
131	275	6.90E+39	1.98E+50	2.61E+50	2.70E+39	5.29E+49	7.52E+49	7.26E+37	7.44E+47	1.26E+48
131	300	8.57E+39	2.30E+50	3.63E+50	4.05E+39	7.71E+49	1.28E+50	1.60E+38	1.63E+48	3.51E+48
131	325	8.84E+39	2.33E+50	3.82E+50	4.39E+39	8.24E+49	1.63E+50	2.18E+38	2.20E+48	7.29E+48
131	350	8.80E+39	2.33E+50	3.80E+50	4.39E+39	8.23E+49	1.63E+50	2.18E+38	2.19E+48	7.29E+48
131	400	8.69E+39	2.30E+50	3.75E+50	4.30E+39	8.08E+49	1.60E+50	2.08E+38	2.09E+48	7.04E+48
131	500	8.62E+39	2.30E+50	3.76E+50	4.20E+39	7.92E+49	1.66E+50	2.00E+38	2.01E+48	8.13E+48
131	600	8.11E+39	2.20E+50	3.63E+50	3.76E+39	7.17E+49	1.55E+50	1.56E+38	1.57E+48	6.82E+48
150	0	6.51E+39	1.92E+50	2.27E+50	2.33E+39	4.63E+49	6.10E+49	5.00E+37	5.14E+47	9.87E+47
150	25	6.49E+39	1.92E+50	2.26E+50	2.33E+39	4.61E+49	6.10E+49	4.97E+37	5.10E+47	9.90E+47
150	50	6.24E+39	1.84E+50	2.26E+50	2.23E+39	4.42E+49	6.09E+49	4.74E+37	4.87E+47	9.84E+47

Table B.1. Continued.

M^i [M_\odot]	v_{rot}^i [km s^{-1}]	$L(\gamma_H)$ [erg/s]	$Q(\gamma_H)$ [s^{-1}]	$Q^{\text{max}}(\gamma_H)$ [s^{-1}]	$L(\gamma_{He})$ [erg/s]	$Q(\gamma_{He})$ [s^{-1}]	$Q^{\text{max}}(\gamma_{He})$ [s^{-1}]	$L(\gamma_{He^+})$ [erg/s]	$Q(\gamma_{He^+})$ [s^{-1}]	$Q^{\text{max}}(\gamma_{He^+})$ [s^{-1}]
150	75	6.60E+39	1.95E+50	2.27E+50	2.34E+39	4.63E+49	6.08E+49	4.93E+37	5.08E+47	9.83E+47
150	100	6.55E+39	1.93E+50	2.27E+50	2.28E+39	4.54E+49	6.08E+49	4.72E+37	4.86E+47	9.71E+47
150	125	6.90E+39	2.04E+50	2.28E+50	2.37E+39	4.73E+49	6.08E+49	4.82E+37	4.96E+47	9.66E+47
150	150	7.09E+39	2.11E+50	2.29E+50	2.47E+39	4.90E+49	6.12E+49	4.95E+37	5.07E+47	9.61E+47
150	175	7.06E+39	2.10E+50	2.31E+50	2.46E+39	4.87E+49	6.25E+49	5.12E+37	5.24E+47	9.61E+47
150	200	6.79E+39	1.98E+50	2.37E+50	2.50E+39	4.94E+49	6.52E+49	5.79E+37	5.95E+47	9.93E+47
150	225	7.76E+39	2.24E+50	2.73E+50	3.01E+39	5.92E+49	7.50E+49	7.61E+37	7.80E+47	1.11E+48
150	250	8.57E+39	2.44E+50	3.03E+50	3.45E+39	6.75E+49	7.82E+49	8.54E+37	8.74E+47	1.23E+48
150	275	8.03E+39	2.30E+50	2.94E+50	3.16E+39	6.17E+49	8.53E+49	8.67E+37	8.86E+47	1.45E+48
150	300	9.51E+39	2.63E+50	3.56E+50	4.15E+39	8.03E+49	1.11E+50	1.35E+38	1.38E+48	2.19E+48
150	325	1.08E+40	2.85E+50	4.53E+50	5.44E+39	1.02E+50	1.95E+50	2.79E+38	2.80E+48	8.94E+48
150	350	1.08E+40	2.83E+50	4.49E+50	5.44E+39	1.02E+50	1.94E+50	2.81E+38	2.83E+48	8.90E+48
150	400	1.07E+40	2.81E+50	4.43E+50	5.35E+39	1.00E+50	1.91E+50	2.71E+38	2.72E+48	8.71E+48
150	450	1.05E+40	2.76E+50	4.37E+50	5.19E+39	9.75E+49	1.86E+50	2.52E+38	2.54E+48	8.24E+48
150	500	1.03E+40	2.73E+50	4.31E+50	5.00E+39	9.43E+49	1.82E+50	2.31E+38	2.32E+48	7.75E+48
150	550	1.03E+40	2.76E+50	4.37E+50	5.01E+39	9.45E+49	1.93E+50	2.38E+38	2.39E+48	9.65E+48
150	600	1.00E+40	2.70E+50	4.30E+50	4.76E+39	9.02E+49	1.88E+50	2.12E+38	2.13E+48	8.97E+48
172	0	7.91E+39	2.31E+50	2.74E+50	2.89E+39	5.70E+49	7.60E+49	6.59E+37	6.76E+47	1.33E+48
172	25	7.86E+39	2.31E+50	2.74E+50	2.86E+39	5.68E+49	7.60E+49	6.54E+37	6.70E+47	1.33E+48
172	50	7.91E+39	2.32E+50	2.74E+50	2.88E+39	5.69E+49	7.59E+49	6.52E+37	6.68E+47	1.33E+48
172	75	8.09E+39	2.38E+50	2.74E+50	2.92E+39	5.76E+49	7.58E+49	6.51E+37	6.70E+47	1.32E+48
172	100	7.99E+39	2.35E+50	2.74E+50	2.84E+39	5.62E+49	7.58E+49	6.26E+37	6.42E+47	1.31E+48
172	125	8.28E+39	2.46E+50	2.75E+50	2.92E+39	5.79E+49	7.59E+49	6.35E+37	6.51E+47	1.30E+48
172	150	8.50E+39	2.52E+50	2.75E+50	2.96E+39	5.89E+49	7.63E+49	6.38E+37	6.55E+47	1.29E+48
172	175	8.88E+39	2.61E+50	2.80E+50	3.17E+39	6.31E+49	7.80E+49	6.92E+37	7.10E+47	1.29E+48
172	200	9.72E+39	2.76E+50	3.19E+50	3.92E+39	7.69E+49	8.44E+49	9.74E+37	9.97E+47	1.34E+48
172	225	9.88E+39	2.84E+50	3.22E+50	3.85E+39	7.57E+49	8.94E+49	9.64E+37	9.87E+47	1.40E+48
172	250	9.13E+39	2.63E+50	3.22E+50	3.55E+39	6.93E+49	9.34E+49	9.54E+37	9.75E+47	1.50E+48
172	275	9.10E+39	2.62E+50	3.35E+50	3.58E+39	6.98E+49	9.85E+49	1.00E+38	1.03E+48	1.69E+48
172	300	1.06E+40	2.99E+50	3.81E+50	4.46E+39	8.63E+49	1.12E+50	1.36E+38	1.39E+48	2.11E+48
172	325	1.28E+40	3.40E+50	5.19E+50	6.32E+39	1.19E+50	1.97E+50	2.87E+38	2.90E+48	6.12E+48
172	350	1.31E+40	3.43E+50	5.28E+50	6.69E+39	1.25E+50	2.28E+50	3.55E+38	3.57E+48	1.05E+49
172	400	1.30E+40	3.39E+50	5.21E+50	6.58E+39	1.23E+50	2.25E+50	3.44E+38	3.45E+48	1.04E+49
172	500	1.25E+40	3.32E+50	5.07E+50	6.17E+39	1.16E+50	2.16E+50	2.96E+38	2.99E+48	9.40E+48
172	600	1.23E+40	3.29E+50	5.06E+50	5.94E+39	1.12E+50	2.25E+50	2.78E+38	2.80E+48	1.13E+49
196	0	9.45E+39	2.75E+50	3.26E+50	3.50E+39	6.90E+49	9.31E+49	8.44E+37	8.64E+47	1.74E+48
196	25	9.43E+39	2.75E+50	3.26E+50	3.50E+39	6.88E+49	9.30E+49	8.39E+37	8.59E+47	1.74E+48
196	50	9.50E+39	2.77E+50	3.26E+50	3.50E+39	6.90E+49	9.30E+49	8.36E+37	8.57E+47	1.73E+48
196	75	9.65E+39	2.83E+50	3.26E+50	3.54E+39	6.97E+49	9.29E+49	8.37E+37	8.57E+47	1.73E+48
196	100	9.47E+39	2.78E+50	3.27E+50	3.44E+39	6.77E+49	9.28E+49	8.02E+37	8.22E+47	1.71E+48
196	125	1.01E+40	2.97E+50	3.30E+50	3.61E+39	7.15E+49	9.30E+49	8.26E+37	8.46E+47	1.70E+48
196	150	1.04E+40	3.04E+50	3.39E+50	3.76E+39	7.46E+49	9.37E+49	8.45E+37	8.66E+47	1.69E+48
196	175	1.10E+40	3.20E+50	3.46E+50	4.02E+39	7.95E+49	9.63E+49	9.08E+37	9.33E+47	1.69E+48
196	200	1.08E+40	3.12E+50	3.83E+50	4.22E+39	8.27E+49	1.01E+50	1.08E+38	1.11E+48	1.71E+48
196	225	9.88E+39	2.85E+50	3.56E+50	3.85E+39	7.52E+49	1.04E+50	1.04E+38	1.06E+48	1.76E+48
196	250	1.22E+40	3.47E+50	4.12E+50	4.99E+39	9.78E+49	1.11E+50	1.32E+38	1.35E+48	1.86E+48
196	275	1.08E+40	3.07E+50	3.92E+50	4.31E+39	8.37E+49	1.16E+50	1.25E+38	1.27E+48	2.03E+48
196	300	1.28E+40	3.55E+50	4.34E+50	5.62E+39	1.09E+50	1.27E+50	1.77E+38	1.80E+48	2.36E+48
196	325	1.42E+40	3.87E+50	5.27E+50	6.40E+39	1.23E+50	1.78E+50	2.37E+38	2.42E+48	4.10E+48
196	350	1.56E+40	4.07E+50	6.11E+50	7.96E+39	1.49E+50	2.59E+50	4.20E+38	4.21E+48	1.12E+49
196	400	1.55E+40	4.04E+50	6.04E+50	7.90E+39	1.48E+50	2.59E+50	4.18E+38	4.22E+48	1.16E+49
196	500	1.50E+40	3.95E+50	5.89E+50	7.47E+39	1.40E+50	2.50E+50	3.65E+38	3.69E+48	1.08E+49
196	600	1.48E+40	3.94E+50	5.88E+50	7.23E+39	1.36E+50	2.61E+50	3.48E+38	3.50E+48	1.32E+49
224	0	1.01E+40	2.94E+50	3.89E+50	3.81E+39	7.48E+49	1.14E+50	9.60E+37	9.83E+47	2.25E+48
224	25	1.13E+40	3.29E+50	3.89E+50	4.27E+39	8.38E+49	1.14E+50	1.07E+38	1.10E+48	2.25E+48
224	50	1.14E+40	3.33E+50	3.89E+50	4.28E+39	8.41E+49	1.14E+50	1.07E+38	1.10E+48	2.24E+48
224	75	1.16E+40	3.40E+50	3.89E+50	4.32E+39	8.50E+49	1.14E+50	1.07E+38	1.10E+48	2.24E+48
224	100	1.08E+40	3.16E+50	3.91E+50	3.98E+39	7.86E+49	1.14E+50	9.80E+37	1.00E+48	2.21E+48
224	125	1.15E+40	3.37E+50	3.94E+50	4.15E+39	8.18E+49	1.14E+50	1.01E+38	1.03E+48	2.20E+48
224	150	1.20E+40	3.54E+50	3.96E+50	4.32E+39	8.54E+49	1.15E+50	1.04E+38	1.07E+48	2.18E+48

Table B.1. Continued.

M^i [M_{\odot}]	v_{rot}^i [km s^{-1}]	$L(\gamma_H)$ [erg/s]	$Q(\gamma_H)$ [s^{-1}]	$Q^{\text{max}}(\gamma_H)$ [s^{-1}]	$L(\gamma_{He})$ [erg/s]	$Q(\gamma_{He})$ [s^{-1}]	$Q^{\text{max}}(\gamma_{He})$ [s^{-1}]	$L(\gamma_{He^+})$ [erg/s]	$Q(\gamma_{He^+})$ [s^{-1}]	$Q^{\text{max}}(\gamma_{He^+})$ [s^{-1}]
224	175	1.26E+40	3.71E+50	4.01E+50	4.57E+39	9.03E+49	1.16E+50	1.09E+38	1.12E+48	2.18E+48
224	200	1.32E+40	3.84E+50	4.50E+50	4.99E+39	9.79E+49	1.21E+50	1.27E+38	1.30E+48	2.19E+48
224	225	1.44E+40	4.05E+50	4.63E+50	5.99E+39	1.17E+50	1.25E+50	1.64E+38	1.67E+48	2.22E+48
224	250	1.30E+40	3.70E+50	4.46E+50	5.23E+39	1.02E+50	1.30E+50	1.51E+38	1.55E+48	2.30E+48
224	275	1.36E+40	3.85E+50	4.63E+50	5.54E+39	1.07E+50	1.37E+50	1.66E+38	1.70E+48	2.43E+48
224	300	1.59E+40	4.44E+50	5.60E+50	6.78E+39	1.32E+50	1.51E+50	2.05E+38	2.10E+48	2.78E+48
224	325	1.52E+40	4.20E+50	5.60E+50	6.71E+39	1.29E+50	1.79E+50	2.34E+38	2.39E+48	3.53E+48
224	350	1.81E+40	4.78E+50	6.93E+50	8.96E+39	1.68E+50	2.55E+50	4.12E+38	4.17E+48	7.64E+48
224	400	1.85E+40	4.80E+50	6.98E+50	9.41E+39	1.76E+50	2.94E+50	4.98E+38	5.01E+48	1.24E+49
224	500	1.79E+40	4.71E+50	6.83E+50	8.95E+39	1.68E+50	2.86E+50	4.43E+38	4.46E+48	1.20E+49
224	600	1.77E+40	4.70E+50	6.82E+50	8.69E+39	1.63E+50	2.98E+50	4.19E+38	4.21E+48	1.43E+49
257	0	1.37E+40	3.97E+50	4.64E+50	5.24E+39	1.03E+50	1.39E+50	1.38E+38	1.41E+48	2.89E+48
257	25	1.38E+40	3.99E+50	4.64E+50	5.24E+39	1.03E+50	1.39E+50	1.38E+38	1.41E+48	2.89E+48
257	50	1.39E+40	4.03E+50	4.64E+50	5.26E+39	1.03E+50	1.39E+50	1.37E+38	1.41E+48	2.88E+48
257	75	1.33E+40	3.87E+50	4.65E+50	5.00E+39	9.83E+49	1.39E+50	1.30E+38	1.32E+48	2.87E+48
257	100	1.31E+40	3.82E+50	4.67E+50	4.88E+39	9.58E+49	1.39E+50	1.25E+38	1.28E+48	2.85E+48
257	125	1.41E+40	4.12E+50	4.73E+50	5.18E+39	1.02E+50	1.40E+50	1.32E+38	1.35E+48	2.83E+48
257	150	1.45E+40	4.23E+50	4.76E+50	5.32E+39	1.04E+50	1.42E+50	1.36E+38	1.39E+48	2.81E+48
257	175	1.50E+40	4.38E+50	4.82E+50	5.53E+39	1.09E+50	1.44E+50	1.43E+38	1.46E+48	2.80E+48
257	200	1.67E+40	4.76E+50	5.22E+50	6.79E+39	1.33E+50	1.47E+50	1.79E+38	1.83E+48	2.79E+48
257	225	1.66E+40	4.76E+50	5.45E+50	6.44E+39	1.26E+50	1.50E+50	1.72E+38	1.75E+48	2.81E+48
257	250	1.51E+40	4.31E+50	5.20E+50	6.11E+39	1.19E+50	1.55E+50	1.83E+38	1.87E+48	2.88E+48
257	275	1.53E+40	4.32E+50	5.42E+50	6.24E+39	1.21E+50	1.63E+50	1.91E+38	1.95E+48	3.00E+48
257	300	1.76E+40	4.94E+50	6.07E+50	7.44E+39	1.44E+50	1.75E+50	2.37E+38	2.42E+48	3.29E+48
257	325	1.84E+40	5.08E+50	6.61E+50	8.14E+39	1.56E+50	2.05E+50	2.85E+38	2.90E+48	3.88E+48
257	350	2.20E+40	5.95E+50	7.67E+50	1.03E+40	1.97E+50	2.53E+50	4.20E+38	4.27E+48	5.78E+48
257	375	2.19E+40	5.73E+50	8.14E+50	1.12E+40	2.10E+50	3.35E+50	5.90E+38	5.95E+48	1.32E+49
257	400	2.19E+40	5.71E+50	8.09E+50	1.12E+40	2.10E+50	3.35E+50	5.93E+38	5.97E+48	1.35E+49
257	500	2.19E+40	5.73E+50	8.09E+50	1.12E+40	2.09E+50	3.49E+50	5.89E+38	5.91E+48	1.61E+49
257	600	2.11E+40	5.58E+50	7.91E+50	1.04E+40	1.95E+50	3.39E+50	4.97E+38	5.01E+48	1.52E+49
294	0	1.38E+40	3.96E+50	5.50E+50	5.30E+39	1.03E+50	1.69E+50	1.45E+38	1.48E+48	3.65E+48
294	25	1.66E+40	4.81E+50	5.50E+50	6.39E+39	1.25E+50	1.69E+50	1.74E+38	1.78E+48	3.65E+48
294	50	1.68E+40	4.86E+50	5.50E+50	6.44E+39	1.26E+50	1.68E+50	1.75E+38	1.78E+48	3.64E+48
294	75	1.61E+40	4.68E+50	5.52E+50	6.13E+39	1.20E+50	1.68E+50	1.65E+38	1.68E+48	3.62E+48
294	100	1.49E+40	4.32E+50	5.54E+50	5.61E+39	1.10E+50	1.69E+50	1.49E+38	1.52E+48	3.60E+48
294	125	1.56E+40	4.54E+50	5.58E+50	5.83E+39	1.14E+50	1.69E+50	1.54E+38	1.58E+48	3.58E+48
294	150	1.69E+40	4.94E+50	5.68E+50	6.21E+39	1.22E+50	1.71E+50	1.65E+38	1.69E+48	3.55E+48
294	175	1.66E+40	4.81E+50	5.74E+50	6.34E+39	1.24E+50	1.73E+50	1.78E+38	1.82E+48	3.53E+48
294	200	2.00E+40	5.64E+50	6.13E+50	8.23E+39	1.61E+50	1.76E+50	2.26E+38	2.32E+48	3.52E+48
294	225	2.04E+40	5.73E+50	6.43E+50	8.56E+39	1.66E+50	1.79E+50	2.42E+38	2.48E+48	3.52E+48
294	250	1.77E+40	5.02E+50	6.04E+50	7.19E+39	1.39E+50	1.84E+50	2.21E+38	2.25E+48	3.57E+48
294	275	1.91E+40	5.40E+50	6.30E+50	7.82E+39	1.52E+50	1.90E+50	2.46E+38	2.50E+48	3.69E+48
294	300	1.97E+40	5.53E+50	6.47E+50	8.26E+39	1.60E+50	2.03E+50	2.73E+38	2.77E+48	3.90E+48
294	325	2.17E+40	6.04E+50	7.70E+50	9.61E+39	1.84E+50	2.32E+50	3.35E+38	3.42E+48	4.44E+48
294	350	2.40E+40	6.47E+50	8.45E+50	1.12E+40	2.14E+50	2.61E+50	4.24E+38	4.31E+48	5.39E+48
294	375	2.54E+40	6.77E+50	9.31E+50	1.25E+40	2.37E+50	3.17E+50	5.48E+38	5.55E+48	8.49E+48
294	400	2.64E+40	6.87E+50	9.49E+50	1.36E+40	2.54E+50	3.92E+50	7.34E+38	7.37E+48	1.56E+49
294	450	2.61E+40	6.80E+50	9.37E+50	1.34E+40	2.50E+50	3.94E+50	7.20E+38	7.22E+48	1.67E+49
294	500	2.58E+40	6.75E+50	9.34E+50	1.31E+40	2.46E+50	3.92E+50	6.82E+38	6.85E+48	1.64E+49
294	550	2.54E+40	6.69E+50	9.25E+50	1.28E+40	2.40E+50	3.91E+50	6.38E+38	6.41E+48	1.67E+49
294	600	2.49E+40	6.61E+50	9.15E+50	1.23E+40	2.31E+50	3.84E+50	5.81E+38	5.86E+48	1.61E+49

Appendix C: Isochrones (Online material)

Fig. C.1 shows isochrones of our stellar evolutionary calculations for several ages and rotational rates.

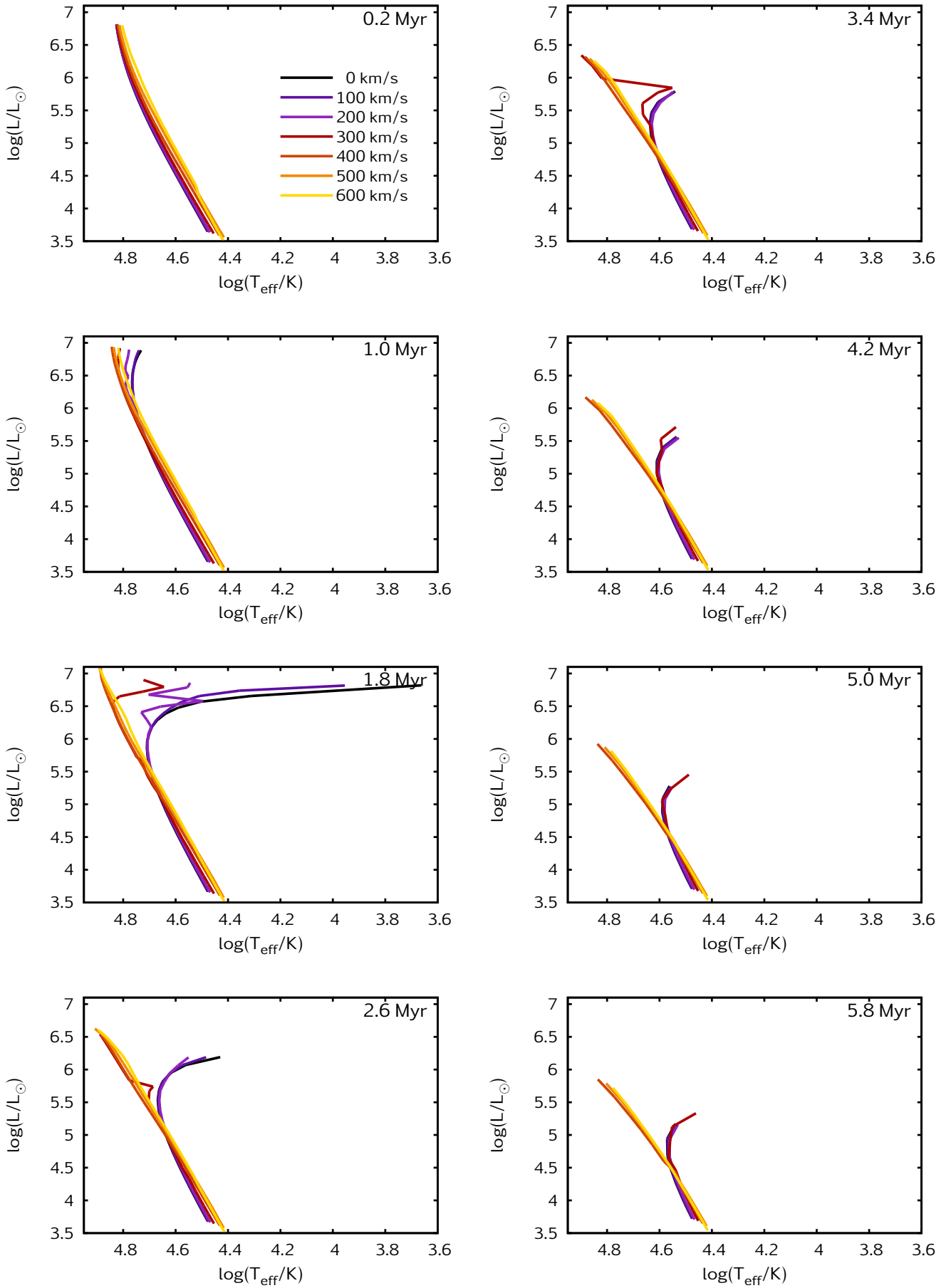


Fig. C.1. Isochrones of different ages of rotating stellar evolutionary models are shown in the HR diagram. The initial surface rotational velocity is chosen in steps of 100 km s^{-1} from non-rotating to 600 km s^{-1}